Contract FP6-IST 508009

ACE
Antenna Centre of Excellence

Instrument: Network of Excellence

Thematic Priority: IST - Information Society Technologies
Mobile and wireless systems beyond 3G

Deliverable ACE-A2.1D2
Report on Activity in
Passive Millimetre and Sub-Millimetre Wave Antennas

Due date of deliverable: 31st December 2005
Actual submission date: 31st Deember 2005

Start date of project: 1/1/2004 Duration: 24 months

Organisation name of lead contractor for this deliverable: **"La Sapienza" University of Rome**
Revision [1]

Project co-funded by the European Commission within the Sixth Framework Programme (2002-2006)		
Dissemination Level		
PU	Public	
PP	Restricted to other programme participants (including the Commission Services)	
RE	Restricted to a group specified by the consortium (including the Commission Services)	X
CO	Confidential, only for members of the consortium (including the Commission Services)	

Document Number: FP6-IST-508009-2.1D2

Workpackage: 2.1-2

Estimated Person Months:

Dissemination level (PU,PP,RE,CO): RE

Nature (R, P, D, O): R

Version: 1

Total Number of Pages: 115

File name: ACE-A2.1D2

Editors: "La Sapienza" University of Rome, Rome, Italy

Participants:

"La Sapienza" University of Rome, Italy (*Work Package Leader*)
Alcatel, France
BAE Systems, UK
Ècole Polytechnique Federale de Lausanne, Switzerland
Helsinki University of Technology, Finland
Instituto Superior Técnico, Portugal
Technische Universität Darmstadt, Germany
University of Birmingham, UK
Université de Marne la Vallée, France
University of Rennes, IETR, France

Abstract

A review of the work performed in the framework of WorkPackage 2.1-2 is presented. The activities performed by the WP participants have been carried out by sharing experience and expertise and by exchanging researchers, after an initial assessment of each partner's background and of the current state of the art on the WP topic. The activities have mainly been focused on:

- High-efficiency and multiple-beam antennas
- Metamaterial-based antennas
- Measurement of low-profile array antennas at 150 GHz

The project on high-efficiency and multiple-beam antennas has been coordinated by IETR and has been carried out by Alcatel Alenia Space, BAE, IETR, and IST; in particular, design and simulation of lens antennas has been carried out jointly by BAE, IETR and IST. Metamaterial antennas have been investigated by SAPIENZA and BU. Measurement techniques for antennas at 150 GHz have been considered by HUT.

Keyword List

High-efficiency antennas, multiple-beam antennas, lens antennas, metamaterial antennas, antenna measurements.

Document Evolution

Revision	Date	Reason of change
Rev. 1.0 Draft A		Draft Edition
Rev. 1.0		First Edition

CONTENTS

1. Introduction

A review of the work performed in the framework of WorkPackage 2.1-2 is presented.

The activities performed by the WP participants have been carried out by sharing experience and expertise and by exchanging researchers, after an initial assessment of each partner's background and of the current state of the art on the WP topic. The activities have mainly been focused on:

- High-efficiency and multiple-beam antennas
- Metamaterial-based antennas
- Measurement of low-profile array antennas at 150 GHz

The project on high-efficiency and multiple-beam antennas has been coordinated by IETR and has been carried out by Alcatel Alenia Space, BAE, IETR, and IST (see Section 2.1); in particular, design and simulation of lens antennas has been carried out jointly by BAE, IETR and IST.

Metamaterial antennas has been investigated by SAPIENZA and BU (see Section 2.2).

Measurement techniques for antennas at 150 GHz have been considered by HUT (see Section 2.3).

![a||e logo]

2.1 High-efficiency and multiple-beam antennas

2.1.1 IETR

2.1.1.1. Introduction, background and objectives

We briefly report in this deliverable the activity performed by IETR within WP2.1-2 during the last 24 months.

This deliverable is organized as follows.

Section 2.1.1.2 summarizes briefly the technical activity performed. This includes:
- a. Participation to progress meeting,
- b. Main structuring activities,
- c. Student exchanges,
- d. List of joint papers,
- e. Contribution to other work packages,

The main documents describing in detail the collaborative activities between IETR and other partners are given in secs. 2.1.2 and 2.1.3.

Conclusions and future work are detailed in Section 2.1.1.3.

2.1.1.2. Technical activity performed

Participation to progress meeting

Location, Date	Participants
Noordwijk, 01-30-2004	O. Lafond
Gothenburg, 06-10-2004	M. Himdi, O. Lafond
Nice, 11-11-2004	S. Chainon, O. Lafond, M. Himdi, R. Sauleau
Noordwijk, 05-30-2005	R. Sauleau
Noordwijk, 12-02-2005	O. Lafond, M. Himdi, R. Sauleau

Main structuring activities
a. Coordination of the delta project "High efficiency and multiple beam antennas" in strong cooperation with IT/IST, BAE and Alcatel Alenia Space.

In this framework, a joint project is currently running between IT/IST and IETR. The specifications have been defined by Alcatel Alenia Space. They deal with the design of compact lens antennas for global coverage in Ka band. This work includes the development of specific modules in home-made softwares, the design and optimization of lens antennas, the fabrication of lens prototypes and the experimental characterization of lens prototypes.

A copy of the joint report writen by IT/IST and IETR is given in Appendix 2.

b. Benchmark of lens analysis tools in cooperation with IT/IST and BAE.

A copy of the report is given in Appendix 3.

Student exchanges

Keith Lee, from University of Birmingham, spent three weeks at IETR (July 2005) for preliminary studies on composite right/left handed metamaterials.

List of joint papers

O. LAFOND, M. HIMDI, Y. CAILLOCE, O. VENDIER, "Multilayer antenna array in Q band for spatial communication", 11th International Symposium on Antenna Technology and Applied Electromagnetics, ANTEM 2005, Saint-Malo, France, 15-17 Juin 2005.

R. SAULEAU, C. A. FERNANDES, J. R. COSTA, "Review of lens antenna design and technologies for mm-wave shaped-beam applications", 11th International Symposium on Antenna Technology and Applied Electromagnetics, ANTEM 2005, Saint-Malo, France, 15-17 Juin 2005.

Contribution to other work packages

We precise below additional activities that are in strong relations with WP2.1-2:

- WP3.1-3: European School of Antennas
    - Organization of the course "Microwave and millimeter wave antennas",
    - Participation in the course "Analysis and design of large antennas" (R. Sauleau);
- WP2.1-3:
    - Reports on micromachining fabrication techniques, micromachined antennas and MEMS antennas,
    - Benchmarking lens antenna technology (in the framework of the above mentionned delta project);

2.1.1.3. Conclusions and future work

IETR has strong interests in contributing in the following activities:
- Analysis of mechanically reconfigurable mm-wave antennas

- Analysis and design of sub-mm wave planar arrays (300 GHz and beyond)

We previously studied conventional micromachined antennas. To our best knowledge, there is no tradeoff analysis about the technological aspects and the optimization of power distribution between the array elements (NRD guides, wave confinement using 3D EBG, etc.). Part of the work should also deal with the optimum design of the elementary feed.

Possible partners: Univ. Birmingham, EPFL, TUD, HUT.

- Quasi-optical antennas:
  - Single-shell and multi-shell shaped lenses (in cooperation with IT/IST and others partners like HUT for sub-mm wave devices)
    - Benchmark of numerical tools with emphasis on:
      - double-shell analysis softwares
      - optimization softwares
    - Reinforcement of the work on double-shell lenses
    - Lens miniaturization
    - Feasibility analysis of beam switching and multiple beam lens antennas at very high frequencies
    - Potential applications in imaging technology (mm or THz)
    - Definition of challenging joint projects in cooperation with industrial partners (Alcatel Alenia Space, BAE SYSTEM)
    - Hybrid structures combining active reconfigurable primary feeds and lenses
  - Inhomogeneous Luneburg lenses
  - Reflectarrays (probably with high gain and wide band capabilities or for multiple beam applications). Passive or reconfigurable structures. Wave interaction with MEMS structures at high frequencies (as suggested by Univ. Birmingham).

- Terahertz antennas (applications, challenges)

- Metamaterial based antennas

2.1.1.4. Appendix : Background

Activities on MM-Wave Passive Antennas

at IETR, Rennes, France

This reports summarizes research activities carried out at IETR about passive millimeter wave antennas.

Several technologies are investigated:

- Slot Waveguide Antennas,
- Microstrip Patch Antenna Arrays and Technologies,
- Lens Antennas,
- Gaussian Beam Antennas,
- Reconfigurable MEMS Antennas,
- Superconducting high-T_c Antennas.

Date of publication: May 30, 2004.

Antenna & Microwave Group, IETR, France (www.ietr.org).

1. Contents

2. Slot Waveguide Antennas

2.1 – Main results

IETR studies slot waveguide antennas and associated circuit up to 35 GHz, using classical waveguide technology (air-filled waveguide) and a technology developed at the IETR based on metallized foam. The structure is foam manufactured and then directly chemistry metallized (gold, silver or copper conductors). Then, slots are realized by mechanical milling. Our results show that there is no prohibitive degradation up to 35 GHz. The metal losses are mainly due to material roughness. However, a special process has been developed to reduce this problem.

Several slot waveguide antennas have been fabricated, using different slot positions to obtain vertical and horizontal polarizations.

2.1.1 – Transversal slot waveguide antenna

This example deals with a transversal slot waveguide antenna. Slots are titled and excited by the waveguide. Frequency scanning is possible around 30 GHz. A matched load is realized at the end of waveguide with graphite (Fig. 2.1).

Fig. 2.1: Transversal slot waveguide antenna.

Several patterns have been measured at different frequencies (Fig. 2.2). The measured gain equals 14 dB, compared to 15 dB for a classical transversal slot waveguide antenna.
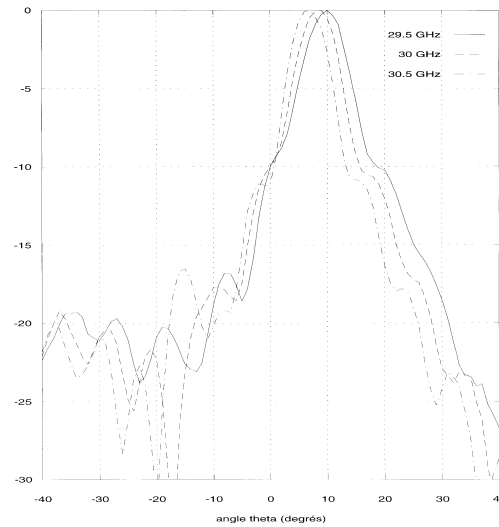
Fig. 2.2: E-plane pattern for 3 frequencies (29.5, 30.0 and 30.5GHz).

Antennas of Fig. 2.1 have an important cross-polarization level due to the slot tilting. A solution consists in feeding two transversal slot waveguides using a magic tee (Fig. 2.3). Both principal co-polarization components add, whereas the cross-polarization components cancel.

Fig. 2.3: Two transversal slot waveguide associated with a magic tee.

2.1.2 – Longitudinal slot waveguide antenna

This example deals with a longitudinal slot waveguide antenna. Slots are cut on the broad face of the waveguide, and displaced from the center of the waveguide. This displacement allows controlling the radiated power (Fig. 2.4).

Fig. 2.4: Longitudinal slot waveguide antenna.

The beam scanning is achieved by a frequency scanning around 33 GHz. The measured H-plane patterns are given in Fig. 2.5.
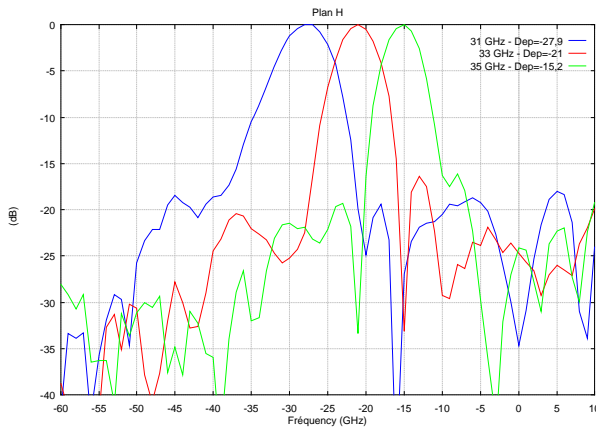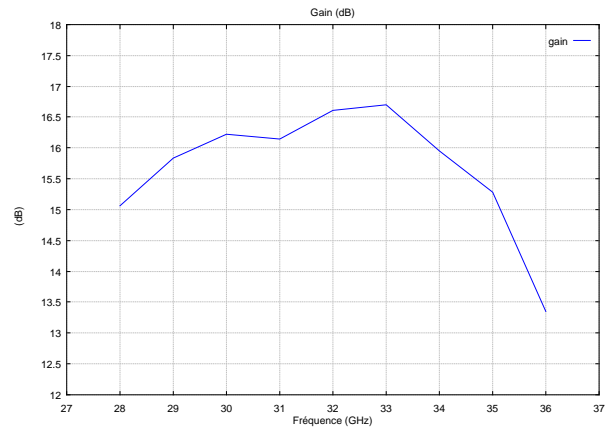
Fig. 2.5: H-plane patterns.

Fig. 2.6: Measured antenna gain.

The beam tilt measured is 21° at 33 GHz, the half power beamwidth is 5.2°. The theory predicted a 20° beam tilt and a 6.2° half power beamwidth. The measured gain (Fig. 2.6) is 16.7 dB at 33 GHz against 17.8 dB predicted, given an efficiency of 80 %.

2.1.3 – Longitudinal slot waveguide fed by probe

The antenna is represented in Fig. 2.7.

Fig. 2.7: Longitudinal slot waveguide Antenna fed by probe.

It is composed of a slot array placed at the center of the broad face of the waveguide. Slots are not fed by the waveguide current lines but by a probe plunging inside, as depicted in Fig. 2.8.
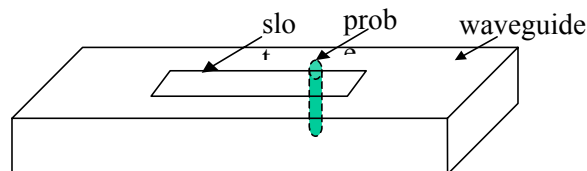

Fig. 2.8: Slot fed by probe.

The radiated power is controlled by the depth of the probe. Beam scanning is obtained thanks to a frequency scanning around 11 GHz. The measured H-plane pattern is given in Fig. 2.9. The total number of slots is equal to 11.
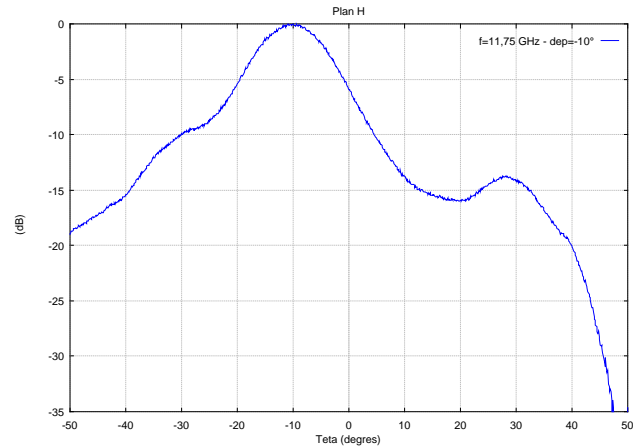
Fig. 2.9: H plane pattern.

The measured gain is 12 dB at 11 GHz.

2.2 – References

S.Chainon "Etude et conception d'antennes composée de guides d'ondes en technologie mousse métallisée. Application aux antennes à balayage électronique", Ph.D., University of Rennes 1,November 26, 2002

M. Himdi, J.-P.Daniel "Procédé de revêtement de mousse pour la fabrication d'éléments d'antenne." French Patent, FR 9808182

3. Microstrip Patch Antenna Arrays and Technologies

Three technologies of multilayer antennas are described :
- Low permittivity (TPX and Glass Teflon) technologies (section 3.1),
- Thin film technologies on quartz and alumina substrates (section 3.2),
- Silicone-based micromachining techniques (section 3.3).

These technologies have been validated up to 60 GHz.

3.1 – Multilayer Antennas: TPX and Glass Teflon technologies

These antennas are printed on Glass Teflon and TPX (Polymethyl-Pentene). Very similar technologies have been developped to realise active antennas.

The objective of the multilayer technology is to separate the feeding line network layer from the radiating elements layer. This allows to avoid spurious radiation due to feeding lines and active components. Examples are given below from 40 to 60 GHz.

3.1.1 – TPX technology

This technology has been developed in collaboration with a local company Avi-Peschard [1, 2, 3] in France. In this kind of technology, a thick metallic support is introduced between the different substrates layers to rigidify the circuit (Fig. 3.1). Moreover this allows to report active components (MMIC). To realise the multilayer circuits, several sheets of substrate are stacked and pressed at high temperature to obtain the TPX correct thickness (0.254 mm or 0.127mm in our cases).
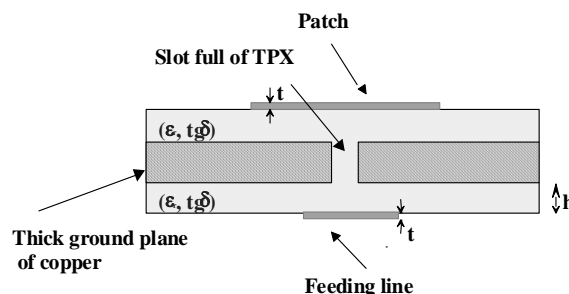

Fig. 3.1: Multilayer TPX technology

A lot of passive antennas have been fabricated up to 60 GHz, including aperture-coupled 16x16 element antenna arrays.

3.1.2 – Glass Teflon technology

This technology has been developed at IETR [3] for comparison with the previous technology. In terms of fabrication, the initial copper film is first removed ; the two substrate layers are then stuck and pressed at high temperature. It needs to oxide metallic support to stick substrate layers on this thick plane.
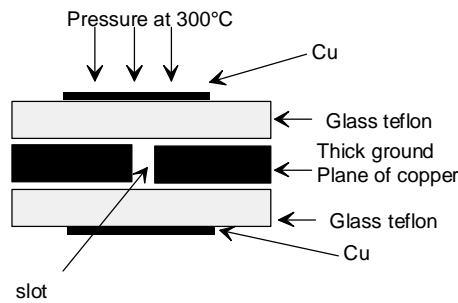

Fig. 3.2: Multilayer Glass teflon technology

A lot of kind of antennas have been manufactured with this technology and give good results in term of efficiency for example.

3.1.3 – Antennas and arrays printed on TPX substrates

Different kind of arrays have been optimised and fabricated between 40 and 60 GHz. The objectives were to study multilayer antennas and to obtain different radiation patterns.

Fig. 3.3 shows a linear array comprising 6 elements operating at 60 GHz. Each element is an aperture-coupled microstrip patch antenna. The feeding of each element is tapered to obtain a side lobe level lower than –25 dB. A good efficiency (55%) has been obtained with this array.

(a)   (b)

Fig. 3.3: Linear array. (a) Radiating elements.
(b) Feeding network Amplitude taper: (0.3; 0.7, 1, 1, 0.7, 0.3)

On the other hand, for indoor communication systems, it may be interesting that base stations antennas radiate a sector beam. A linear array of 6 patches is represented in Fig. 3.4. The radiating

elements are tapered in amplitude and phase to obtain the sector beam. The measured radiationg pattern is represented at 57.5 GHz in Fig. 3.5. The measured efficiency is equal to 58%.

To qualify this technology with important surfaces, some large array with 256 aperture-coupled patches have been studied (Fig. 3.6). Their radiation patterns measured at 59.5 GHz are represented in Fig. 3.7. In this case, no tapering has been applied ; this enables to obtain the highest directivity. Very good results are obtained in term of cross polarisation and side lobe levels. Compared to smaller arrays, the efficiency (30%) decreases because of the higher insertion losses (copper, dielectric loss tangent, …).

(a)   (b)

Fig. 3.4: Linear array. (a) Radiating elements (spacing between patches=0,72xλ_0, excepted between both central elements (0,5xλ_0). (b) Feeding network: Amplitude and phase taper: (0.15, 0°), (0.282, 180°), (1, 0°); (1, 0°), (0.282, 180°), (0.15, 0°).
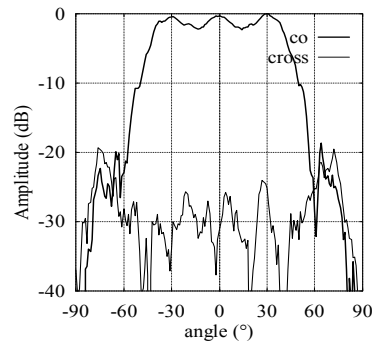
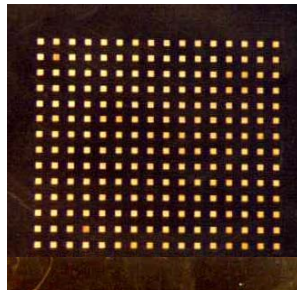

Fig. 3.5: Measured sector beam.
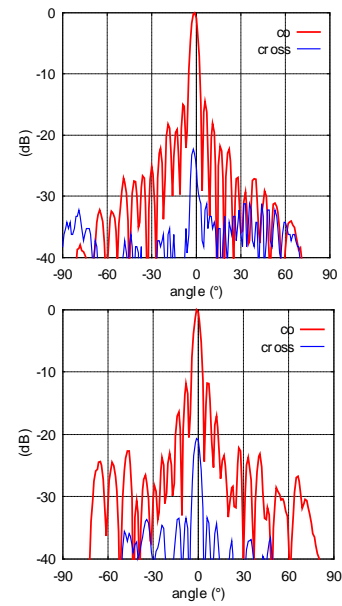
| Fig. 3.6: 16x16 patch antenna array. | Fig. 3.7: Measured radiation patterns. |

The same technology has been used to realise antennas operating in the 40 GHz band. In that case, via holes are used to connect the upper and lower layers. As an example, a 8 element linear array is represented in Fig. 3.8. It is fed by two via holes. This approach has been compared to a similar array whose feeding network is printed on the same layer as the radiating elements (Fig. 3.9). Their radiation patterns are represented in Fig. 3.10 and 3.11.
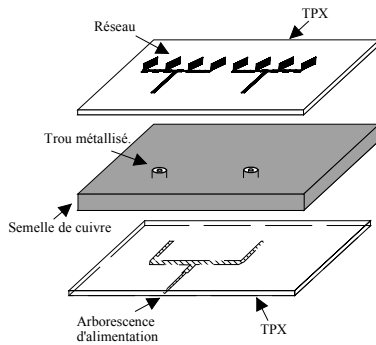

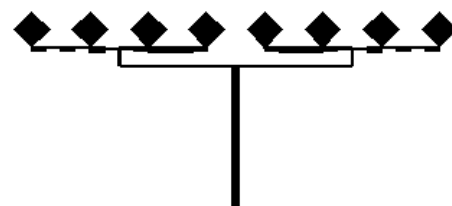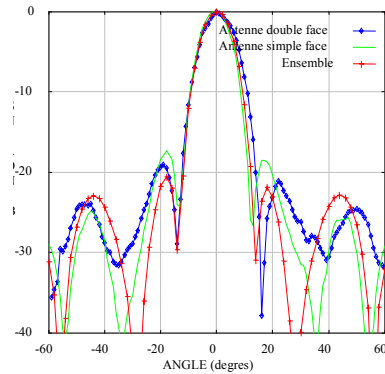| Fig. 3.8: Dual layer linear array with two via holes. | Fig. 3.9: Single layer linear array. |

Fig. 3.10: Measured co-polarization
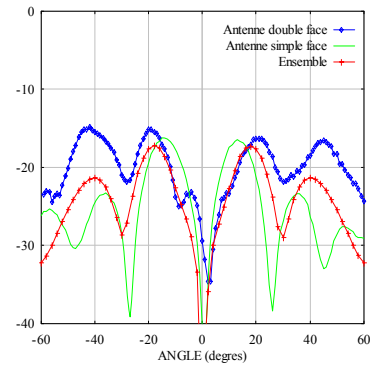components.

Fig. 3.11: Measured cross-polarization
components.

*A similar antenna has been fabricated using aperture-coupled patch antenna elements with a thick
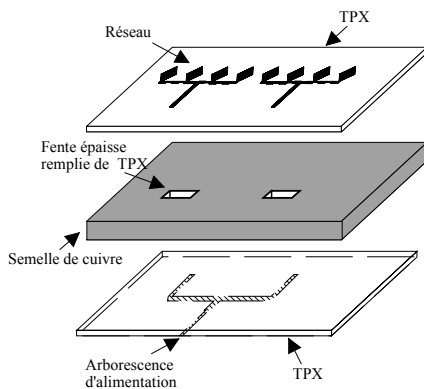ground plane (Fig. 3.12 and 3.13).*
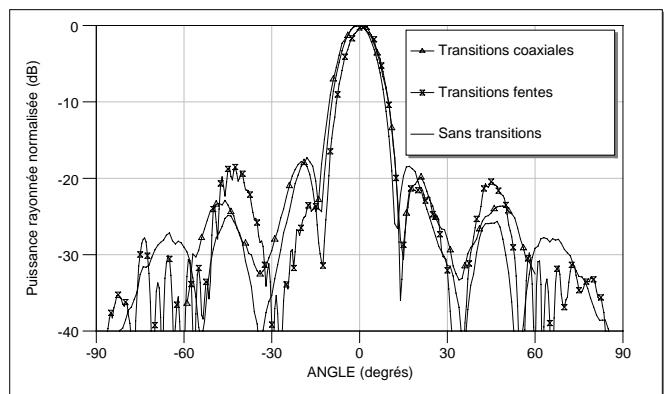

Fig. 3.12: Linear array with a
thick ground plane

Fig. 3.13: Measured radiation patterns (excitation using
via holes, coupling slots, microstrip line).

3.1.4 – Antennas and arrays printed on Glass Teflon substrates

*The same arrays as the ones described in the previous section have been fabricated using Glass
Teflon technology. For example, we compare the radiation patterns of two sector beam arrays in
Glass Teflon (Fig. 3.14) and TPX (Fig. 3.15) technologies. The main results are summarized in
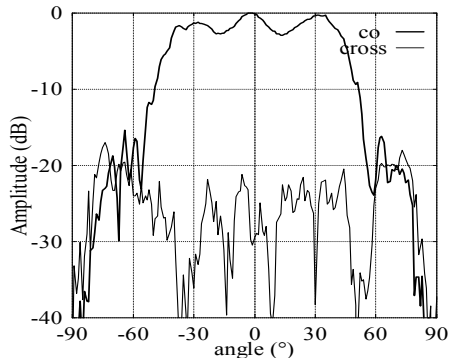Table 3.1. We should note that similar efficiencies are obtained.*

The information contained in this document should be used only for the scope of the contract for which this document is prepared.

Fig. 3.14: Measured sector beam at 57.5 GHz

(Glass Teflon technology).
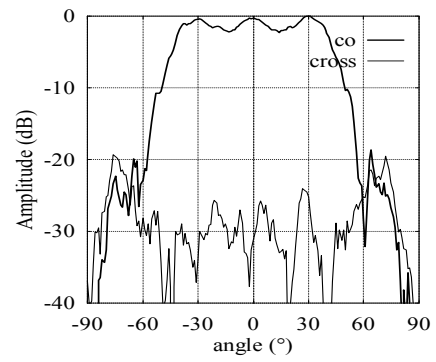
Fig. 3.15: Measured sector beam at 57.5 GHz

(TPX technology).

Substrates	Beamwidth	Sidelobe level	Cross-polar	Efficiency
Glass teflon	80°	< - 16 dB	< - 19 dB	55 %
TPX	84°	< - 20 dB	< - 20 dB	58 %

Table 3.1.

Multibeam antennas have also been fabricated with Glass Teflon substrates. Fig. 3.16 shows a 4-beams Butler matrix feeding a linear array comprising 4 aperture-coupled patch antennas in 60 GHz band. The measured and theoretical radiation patterns are represented in Fig. 3.17a to 3.17d for the four beams. Very good results are obtained in regard to the simulation in terms of tilt angle, beamwidth. The measured efficiency is quite good (40%) for the considering frequency.

All these millimetre antenna examples realised with Glass Teflon or TPX technology are only a part of studies done in IETR institute during these last years. Others devices have been optimised like hybrids (3dB, 90°), feeders for reflectors or lenses, etc.
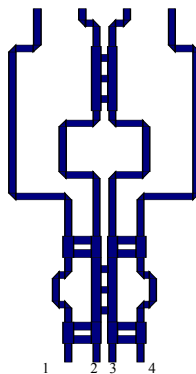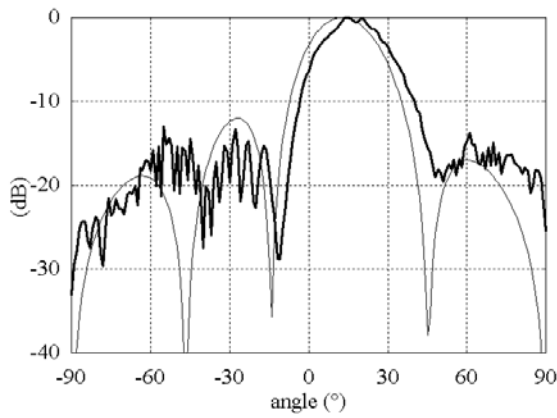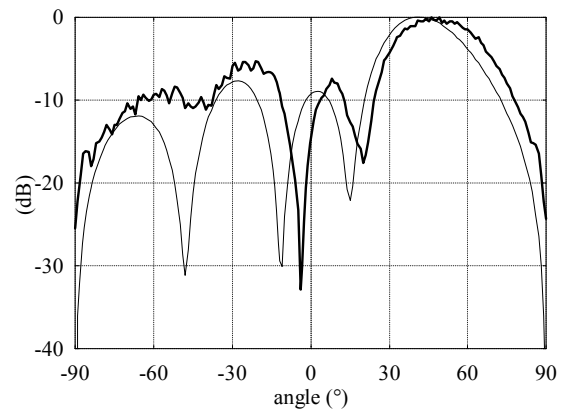

Fig. 3.16: Complete Butler matrix.

(a) Beam #1

(b) Beam #2
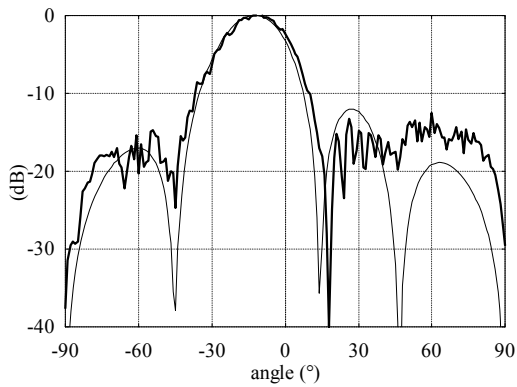
(c) Beam #3
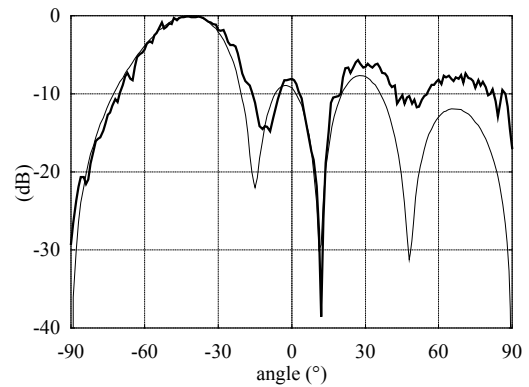
(d) Beam #4

Fig. 3.17: Measured and computed beams of the multibeam antenna.

3.1.5 – Transverse dipole arrays

The basic structure is represented in Fig. 3.18. With such a technique, it is possible to obtain very simple feeding structures comprising a simple microstrip line.
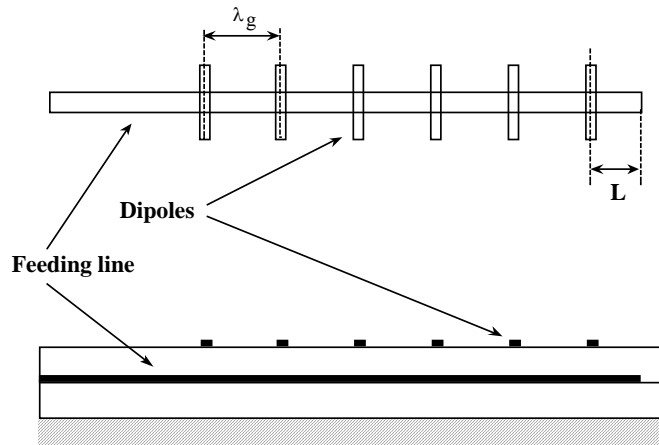
Fig. 3.18: Topology of a linear array.

The design is based on the method developed in [6-7]. Figs. 3.19 to 3.21 show some results obtained with linear arrays comprising 6and 4dipoles, respectively.

Angle in degree

Fig. 3.19: Radiation pattern of the 6 dipole linear array in H-plane (magnitude in dB).

Angle in degree

Fig. 3.20: Radiation pattern of the 4 dipole array in H-plane (magnitude in dB).
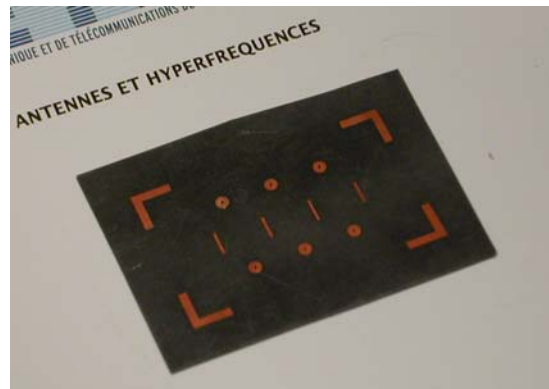
Fig. 3.20: 4 dipole array.

3.2 – Thin film Technologies

Thin film technologies [8-10] have been developed up to 75 GHz for the fabrication of microstrip antennas and quasi-optical structures (see section 5, Gaussian Beam Antennas). Chemical wet etching (Fig. 3.21) and lift-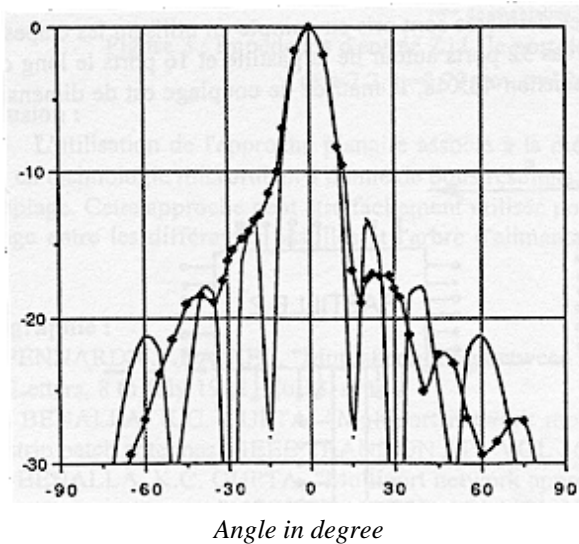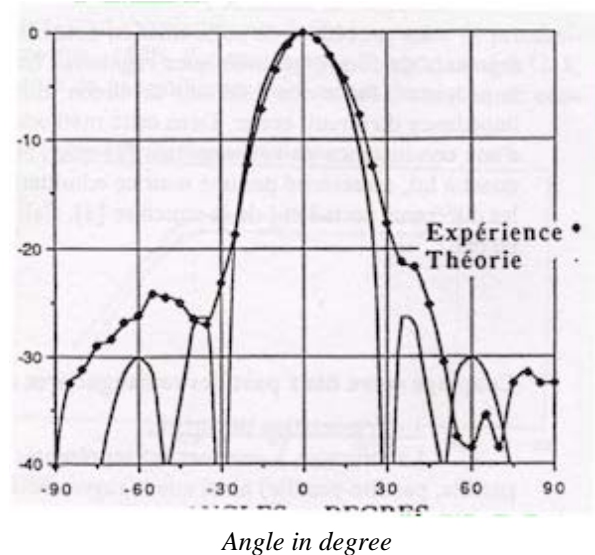off process (Fig. 3.22) have been optimized on fused quartz (ε_r=3.80, $\tan\delta<10^{-4}$) and alumina substrates (ε_r=9.6, $\tan\delta<5\times10^{-4}$) whose dimensions vary between 1 inch square and 5cm in diameter, and whose thickness is comprised between 100µm and 5mm. Conductors are either aluminum or copper. Metal losses are similar in both cases.
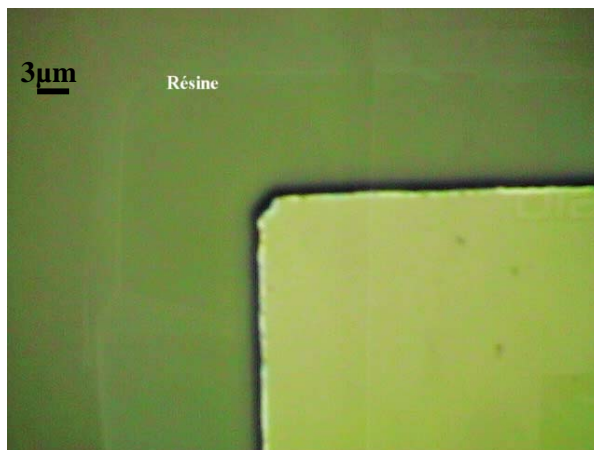
| Fig. 3.21: Corner of a patch antenna after photolithography. | Fig. 3.22: Corner of a patch antenna after lift-off of sputtered copper film. |
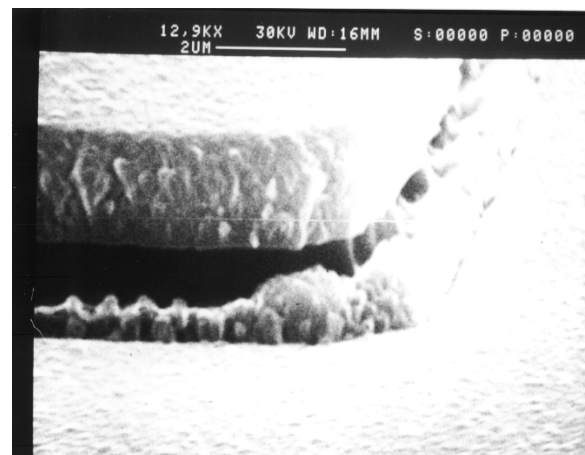
Examples of fabricated antennas using both technologies are represented in Fig. 3.23a (single layer microstrip patch antenna array printed on a 150µm thick alumina substrate), in Fig. 3.24 (aperture-coupled microstrip patch antenna printed on two 140µm thick fused quartz substrates), and in Fig. 3.25a-b (aperture-coupled microstrip antenna array printed on two 137µm thick fused quartz substrates).
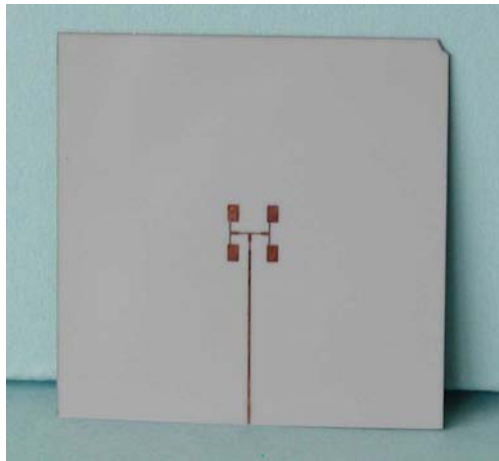
(a)
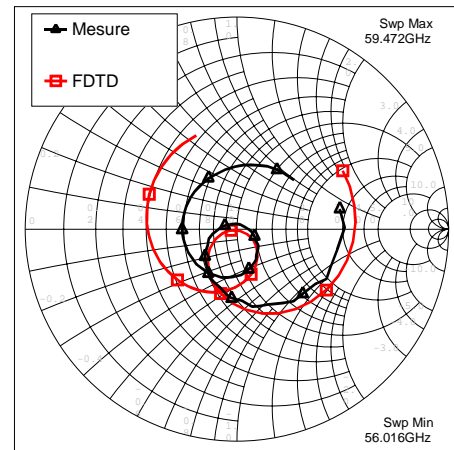
(b)
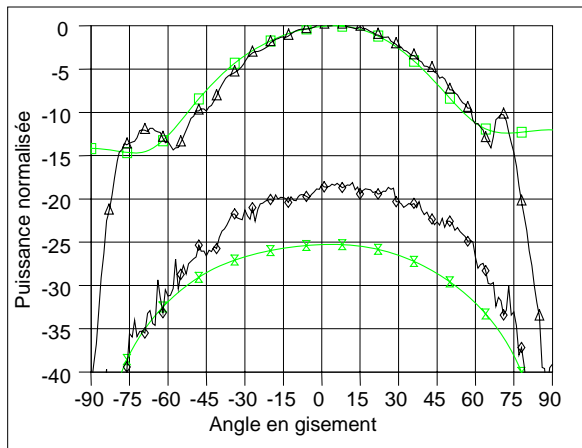
(c)
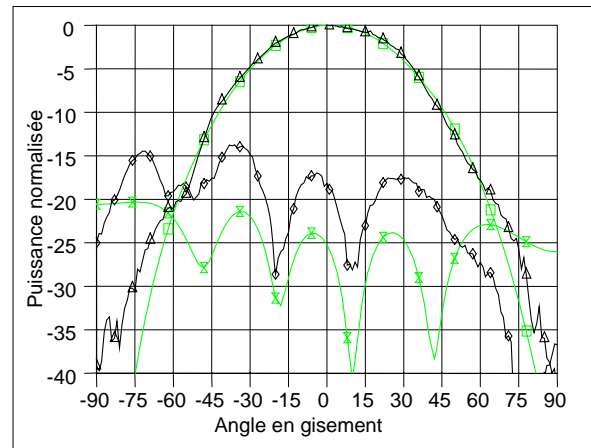
(d)

Fig. 3.23: Single layer microstrip patch antenna array printed on a 150μm thick alumina substrate. (a) Prototype. (b) Measured and computed input impedance. (c,d) Measured and computed radiation patterns in E- (c) and H- (d) planes at 57.5 GHz.

(a)
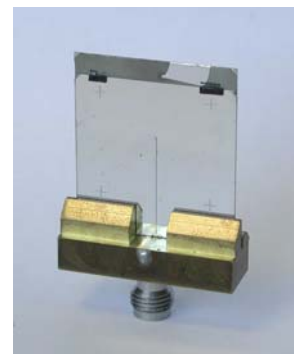
(b)

Fig. 3.24: Aperture-coupled microstrip patch antenna printed on two 140μm thick fused quartz substrates. (a) Radiating element. (b) Microstrip feeding line.
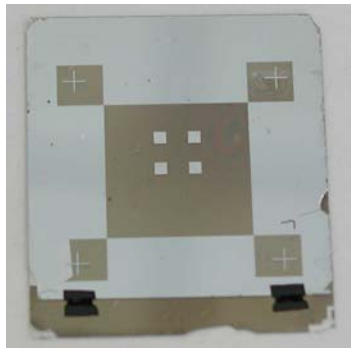
(a)

(b)
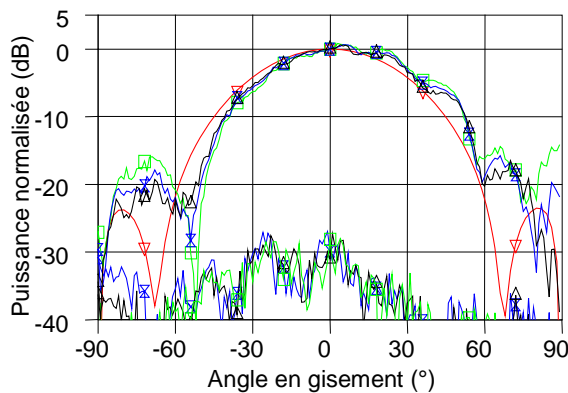
(c)
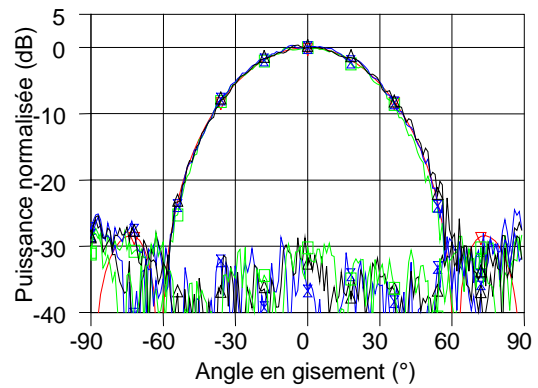
(d)

Fig. 3.25: Aperture-coupled microstrip antenna array printed on two 137µm thick fused quartz substrates rates. (a) Radiating elements. (b) Microstrip feeding network. (c,d) Measured and computed radiation patterns in E- (c) and H- (d) planes at 58 GHz.

Specific wafer bonding techniques have been developed for the fabrication of multilayer microstrip antennas [10]. Influence of residual air gaps for operation in linear and circular polarization have been also investigated theoretically and experimentally [11].

Tables 3.2 and 3.3 summarize the overall radiation performances obtained around 60 GHz microstrip patch antennas and arrays printed on fused quartz and alumina substrates.

Substrate	Cross-polar E-plane	Cross-polar H-plane	Radiation efficiency
Alumina (h=170 µm)	< -20 dB	≈ -20 dB	45% ~ 50%
Fused quartz (h=150 µm)	< -20 dB	≈ -25 dB	80% ~ 84%

Table 3.2 : Radiation performance of microstrip patch antennas at 60 GHz.

Substrate	Technology	Cross-polar E-plane	Cross-polar H-plane	Radiation efficiency
Alumina (t=150 µm)	Single layer	< -18 dB	<-15 dB (≈ -20 dB broadside)	≈ 60 %
Fused quartz (h=140 µm)	Single layer	< -25 dB	<-15 dB (≈ -25 dB broadside)	≈ 75 %
Fused quartz (h=140 µm)	Dual layer	≈ -30 dB	≈ -30 dB	≈ 80 %

Table 3.3 : Radiation performance of microstrip patch antenna arrays at 60 GHz.

3.3 – Silicone-based Micromachining Techniques

It is well known that surface waves alter the performance of printed antennas in terms of radiation characteristics (edge diffraction, mutual coupling between array elements, radiation efficiency). The use of substrates lenses (section 4) or electromagnetic bandgap materials (EBG) has been suggested to reduce this effect.

An alternative solution consists in fabricating the radiating elements on a thin membrane obtained from surface and volume micromachining techniques. Fig. 3.26 represents some antenna structures operating around 60 GHz [12]. The feeding network is fabricated on fused quartz substrates (see section 3.2) whereas the radiating elements are supported by a SiO_2/Si_3N_4 (0.67μm/1μm) membrane. The technological process is described in [12]. Fig. 3.27 shows two examples of prototypes. The theoretical and experimental radiation patterns of the aperture-coupled array of Fig. 3.27a are given in Fig. 3.28.

(a) Aperture-coupled patch antenna.

(b) Aperture-coupled antenna arrays. The membrane is supported (*right*) or not (*left*) by silicon pillars.

(c) Aperture-coupled stacked patch antenna.
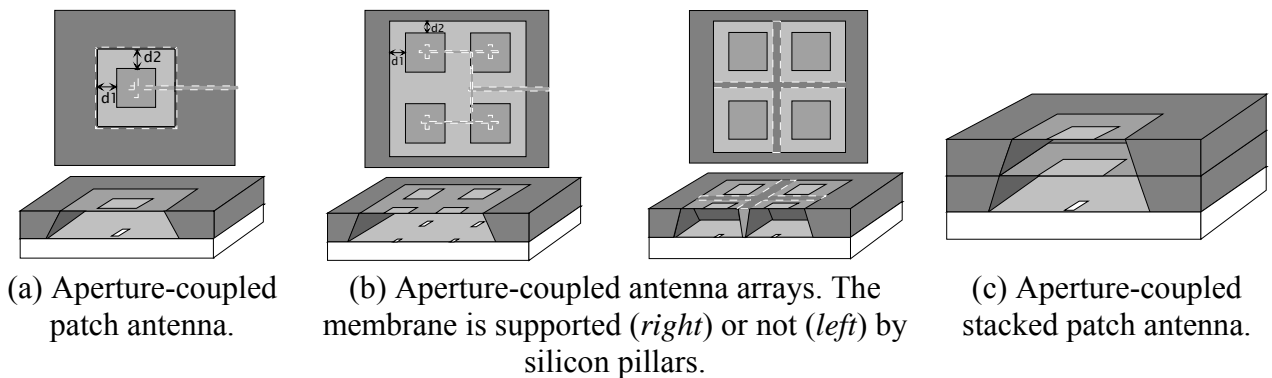
Fig. 3.26: Micromachined antennas

(a)   (b)
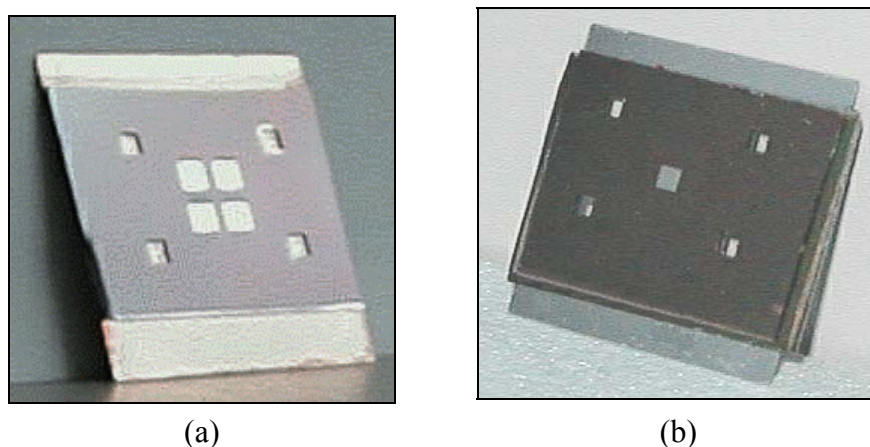
Fig. 3.27: Fabricated antennas. (a) Aperture-coupled antenna arrays. (b) Aperture-coupled stacked patch antenna.
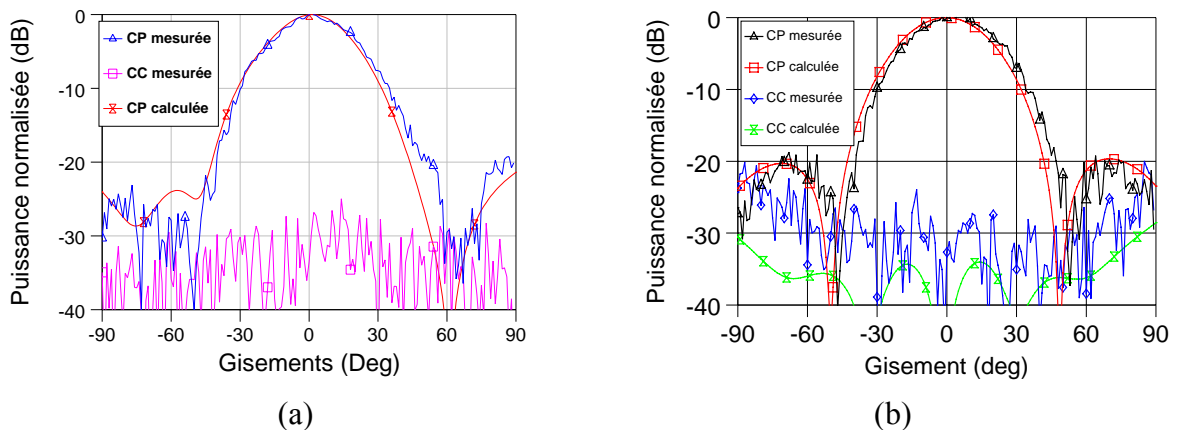
Fig. 3.28: Measured and computed radiation patterns of the array of Fig. 3.27a at 58 GHz.
(a) E-plane. (b) H-plane.

3.4 – References

[1] AVI&PESCHARD : ZAC de la Goulgatière, 35000 Châteaubourg, France.

[2] French Patent, Avi&Peschard, FR 2753724, "Procédé de traitement de surface d'un objet en Polyméthyl-Pentène en vue de sa métallisation", March 1998.

[3] M. EL HAJ SLEIMEN, "Etude de réseaux d'antennes imprimées en millimétrique", Ph.D., University of Rennes 1, March 2, 1999.

[4] O. LAFOND, "Conception et technologies d'antennes imprimées multicouches à 60 GHz", Ph.D., University of Rennes 1, December 4, 2000.

[5] O. LAFOND, M. HIMDI, J.P. DANIEL, "Thick slot coupled printed antennas arrays for a 60 GHz indoor communication system", Microwave and Optical Technology Letters, Vol. 25, n°2 pp. 105-108, 20th January 2001

[6] J.M. FLOC'H, "Conception de réseaux de dipôles transverses en bande millimétrique", JNM 95, Paris, 4, 5, 6 Avril 1995.

[7] J.M. FLOC'H, L. DESCLOS, "Method determines the performance of dipole array", Microwaves & RF, pp. 104-110, September 1995.

[8] R. SAULEAU, "Etude d'antennes imprimées et de cavités de Pérot-Fabry aux fréquences millimétriques. Conception d'antennes à faisceau gaussien", Ph.D, University of Rennes 1, December 9, 1999.

[9] Ph. COQUET, R. SAULEAU, H. LHERMITE, J.-P.DANIEL, T. MATSUI, "Antennes planes bi-couches imprimées sur quartz. Considérations technologiques et performances à 60 GHz", Treizièmes Journées Nationales Micro-ondes, Lille, France, Session 5D19, May 21-23, 2003.

[10] Ph. COQUET, R. SAULEAU, K. SHINOHARA, T. MATSUI, "Multi-Layer microstrip antennas on quartz substrates. Technological considerations and performance at 60 GHz", Microwave and Optical Technology Letters, vol. 40, n°1, pp. 41-47, Jan. 5, 2004.

[11] R. SAULEAU, Ph. COQUET, "Input impedance of electromagnetic bandgap resonator antennas", Microwave and Optical Technology Letters, to appear, June 5, 2004.

[12] A. GAILLARD, R. SAULEAU, H. LHERMITE, Ph. COQUET, "Antennes et réseaux d'antennes millimétriques multi-couches micro-usinées sur Silicium", Treizièmes Journées Nationales Micro-ondes, Lille, France, Session 3B5, May 21-23, 2003.

4. Lens Antennas

Two main categories of dielectric lens antennas were or are currently studied at ITER :
- Homogeneous lenses with conventional or arbitrarily shaped profiles (section 4.1),
- Non homogeneous Luneburg lenses (section 4.2).

The main references are given at the end of each sub-sections (4.1.6 and 4.2.2).

4.1 – Homogeneous lenses

4.1.1 – Analysis, Synthesis and Optimization tools

Dedicated design tools are developed to investigate and optimize the radiation characteristics of homogeneous dielectric radiating structures, such as antenna radomes or dielectric antennas. They have been firstly implemented for the analysis of lens antennas. The organization and the links between the analysis, synthesis and optimization tools are summarized in Fig. 4.1. Their main features are as follows:

- *Asymptotic analysis tools* using:
  - Geometrical Optics (GO),
  - Physical Optics (PO).

- *Resolution of inverse problems*. The aim consists in defining the best shape(s) of lens antennas to achieve a prescribed radiation pattern (directive or shaped patterns), for a given primary source. Multiple internal reflections are usually neglected. This assumption is generally valid if two conditions are satisfied: (1) the relative dielectric constant of the material is smaller than four, and (2) the diameter of the dielectric structure is sufficiently large (at least greater than two or three wavelengths). The inverse problem is solved using GO principles (power conservation principle and vectorial Snell's laws). In the most general case, this leads to a second-order strongly non linear partial differential equation of the Monge-Ampere kind and whose unknown is the lens profile. This equation can be solved by successive iterations after linearization using centered finite differences. The resulting lens shape is thus the solution of the GO problem. This profile can then be optimized using either optimization tools based on PO, or full-wave electromagnetic approaches. Note that this formulation can be drastically simplified for axis-symmetric (BoR) or quasi-axis-symmetric structures.

- *Shape optimization*. The initial lens shape obtained from GO laws has to be optimized to fulfill the initial requirements. Examples of optimized structures are given in Fig. 1.

- *Global analysis*. Our simulation tools rely either on an internally-developed semi-professional Finite-Difference Time-Domain (FDTD) software, or on modal decompositions (Plane Wave Spectrum [PWS] and Spherical Wave Spectrum [SWS]). Commercial softwares, such as CST microwave studio™ and HFSS™, are also used for the analysis of reduced size structures.
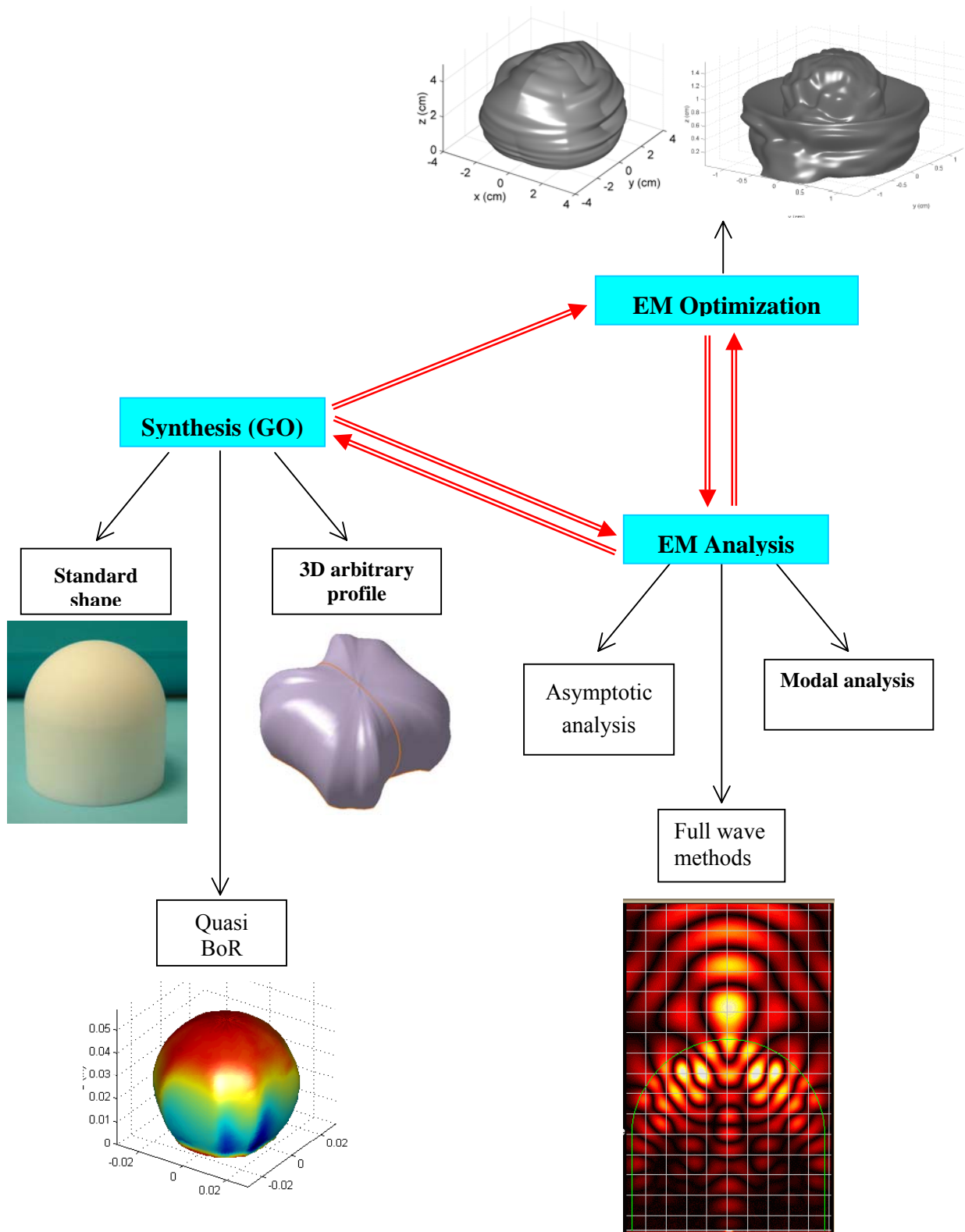
Fig. 4.1: Analysis, Synthesis and Optimisation tools.

(BoR: Body of Revolution; GO: Geometrical Optics; PO: Physical Optics; PWS: Plane Wave Spectrum;

SWS: Spherical Wave Spectrum)

4.1.2 – Examples of canonical structures

Conventional lenses (hyperbolic [Fig. 4.2], extended hemispherical [Fig. 4.3] and hyperhemispherical [Fig. 4.4]) fabricated in Teflon (Figs. 4.2, 4.3) or in Rexolite (Fig. 4.4) have been studied in K-band (from 27.5 to 42.5 GHz and at 38 GHz) and V-band (60 GHz) for high data rate indoor (WLAN) and outdoor (LMDS) communications systems.

(a)

(b)
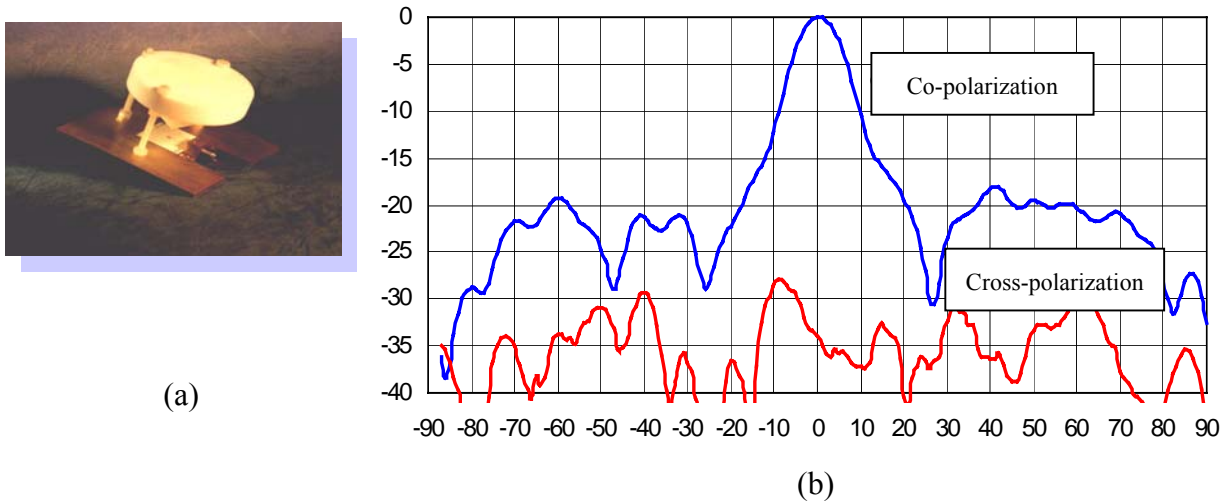
Fig. 4.2: (a) Hyperbolic Teflon lens (diameter=4.2cm, focal length=1.7mm) illuminated by a microstrip patch antenna printed on an Alumina substrate.
(b) Measured radiation pattern in E-plane at 38 GHz.

(a)   (b)
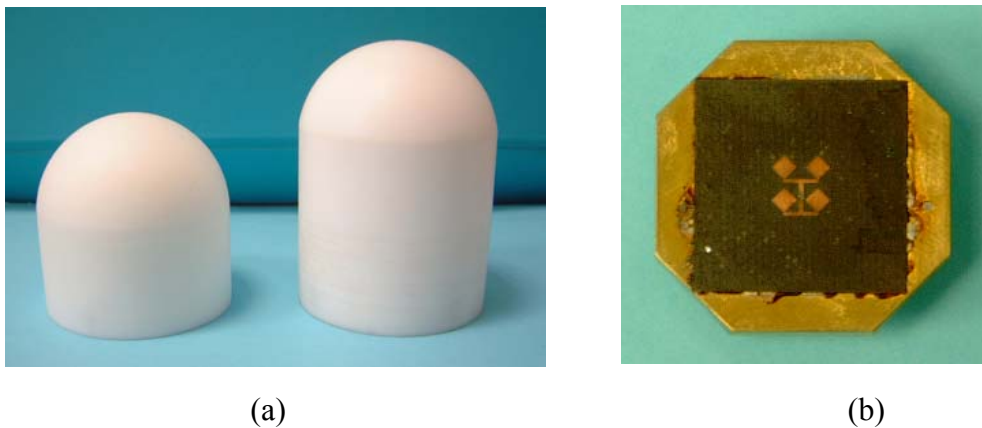
Fig. 4.3: (a) Extended hemispherical Teflon lenses (diameter=6cm) illuminated by a microstrip patch antenna array (b) printed on an RT/Duroïd 5880 substrate (58.5 GHz).

(a)
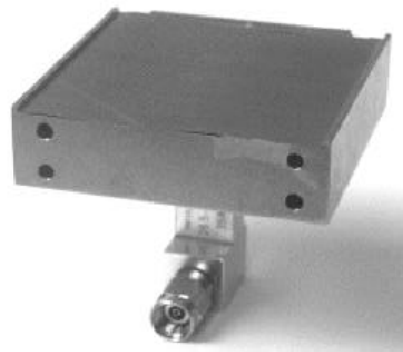
(b)
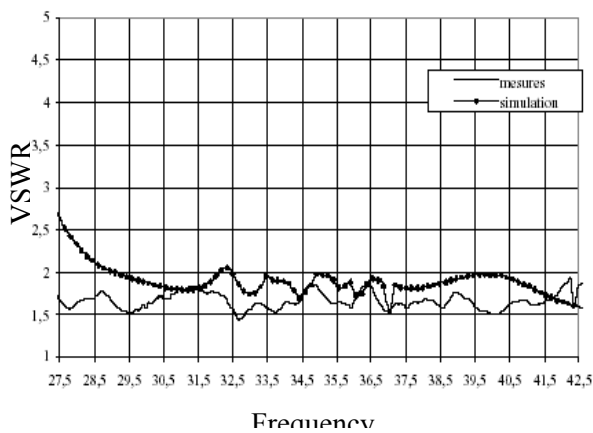
(c)
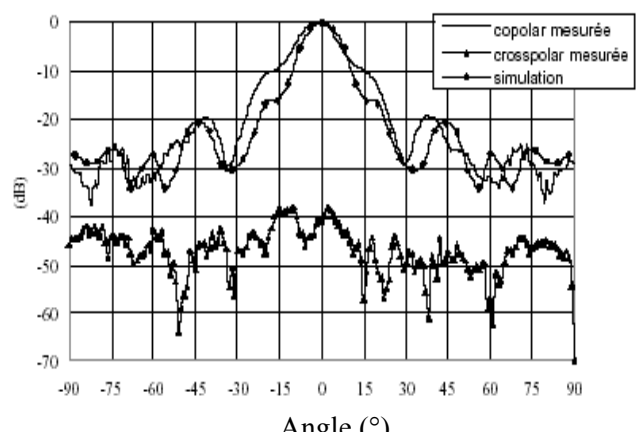
(d)
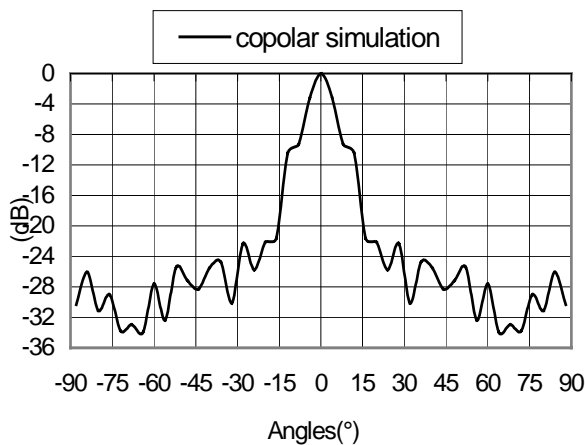
(e)
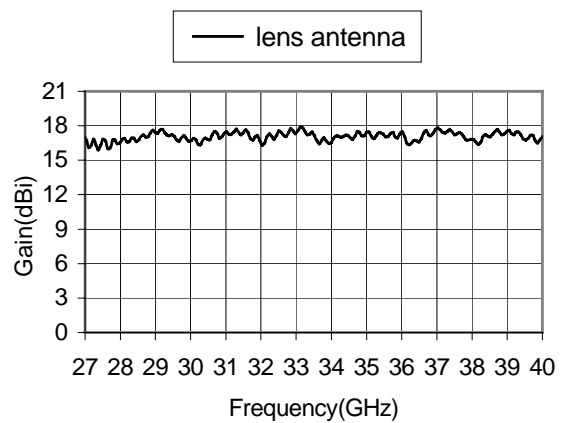
(f)

Fig. 4.4: (a) Hyperhemispherical Rexolite lens illuminated by a waveguide-fed (WR-28) radiating slot. (b) Primary source alone. (c) Measured and computed VSWR. (d) Measured and computed radiation patterns at 28.5 GHz in H-plane. (e) Measured and computed radiation patterns at 41.5 GHz in E-plane. (f) Measured gain.

4.1.3 – Examples of nearly axis-symmetric structures

Fig. 4.5 and 4.6 show two prototypes of lens antennas fabricated in Teflon (ε_r=2.1) and operating at 58.5 GHz. Both lenses are fed by the same coaxial-probe 2x2 elements microstrip patch antenna array printed on a RT/Duroïd 5880 substrate (h=127µm, Fig. 4.3b). The lens shapes have been defined to obtain a symmetric Gaussian radiation pattern with a half power beamwidth equal to 30°. They have been synthesized either from a "cut-plane" approach (Fig. 4.5, lens #1) or from a rigorous formulation of the Monge-Ampere problem (Fig. 4.6, lens #2). Their theoretical 3D power pattern are represented in Fig. 4.7 and 4.8, respectively. Measured radiation patterns in E- and H-planes are given in Fig. 4.9. The maximum directivity and gain of lens #1 (resp. lens #2) equal 19.9 dBi and 17.1 dB (resp. 18.1 dBi and 17.4 dB).

Fig. 4.5: Lens antenna (#1) operating at 58.5 GHz.
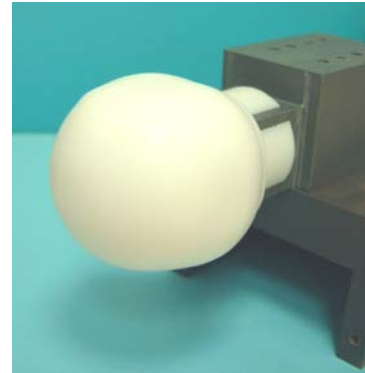
Fig. 4.6: Lens antenna (#2) operating at 58.5 GHz.
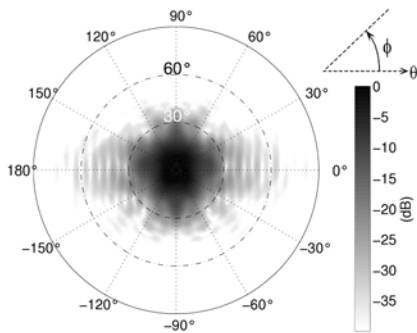
Fig. 4.7: Theoretical 3D power pattern of lens #1.
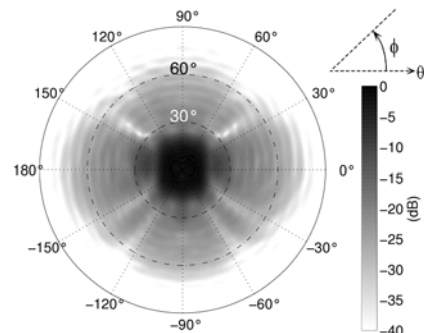
Fig. 4.8: Theoretical 3D power pattern of lens #2.

(a)   (b)
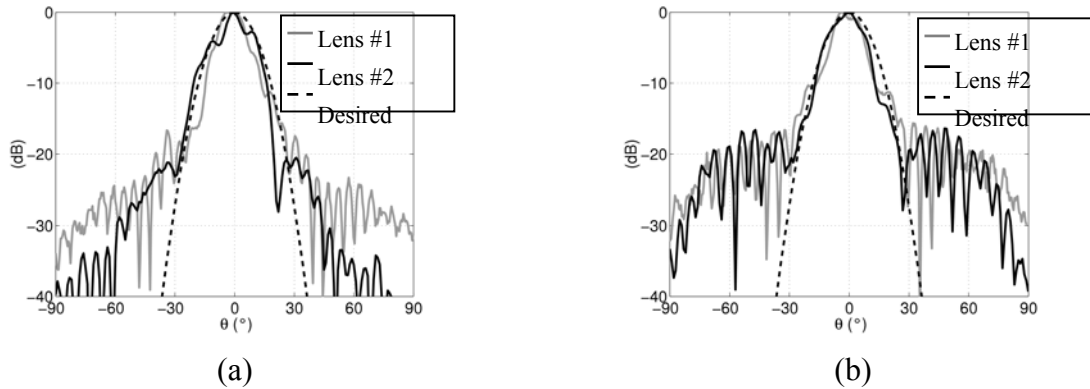
Fig. 4.9: Measured co-polarization components of both lenses at 58.5 GHz.
(a) E-plane, (b) H-plane.

4.1.4 – Examples of structures of arbitrary shape

Similar methodologies can be implemented to design 3D lenses of arbitrary shape. Fig. 4.10 and 4.11 show the 3D view and top view of a 3D lens antenna before and after optimization. In this example, the aim consists in determining the profile of a reduced sized lens antenna (smaller than three wavelengths in free space) generating, over the frequency band 47.2-50.2 GHz, a symmetric radiation pattern with normalized side lobe levels smaller than –12 dB beyond ±24° and a broadside directivity higher than 19dBi. Theoretical and measured results have confirmed the theoretical predictions (Fig. 4.12).

(a)   (b)
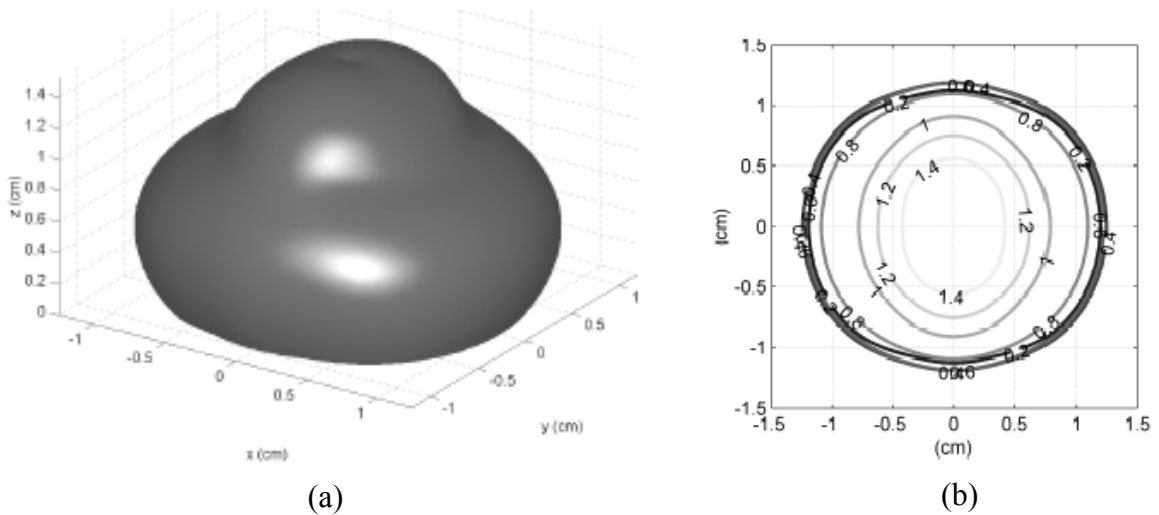
Fig. 4.10: Initial lens profile (before optimization): (a) 3D view, (b) Top view.

(a)   (b)
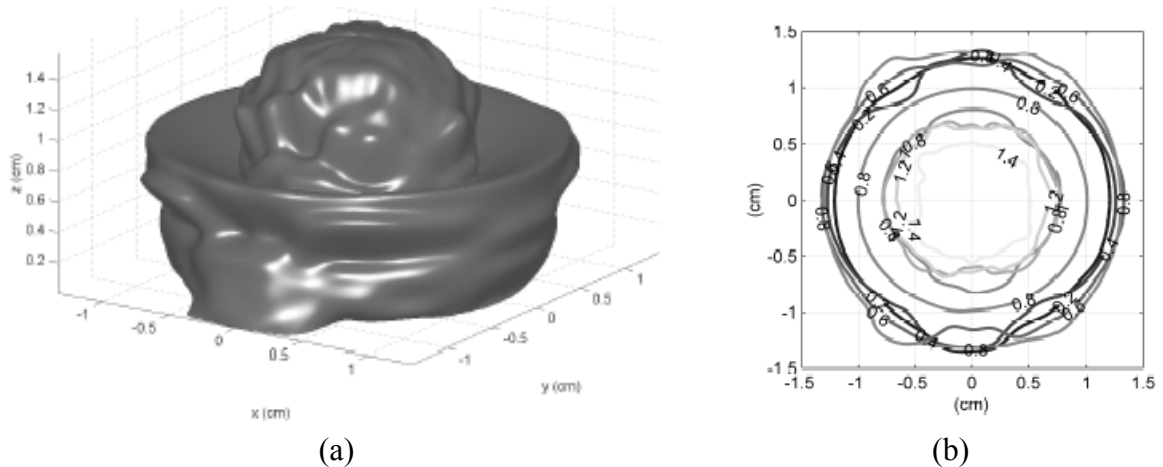
Fig. 4.11: Final lens profile (after optimization): (a) 3D view, (b) Top view.

(a)   b)   (c)
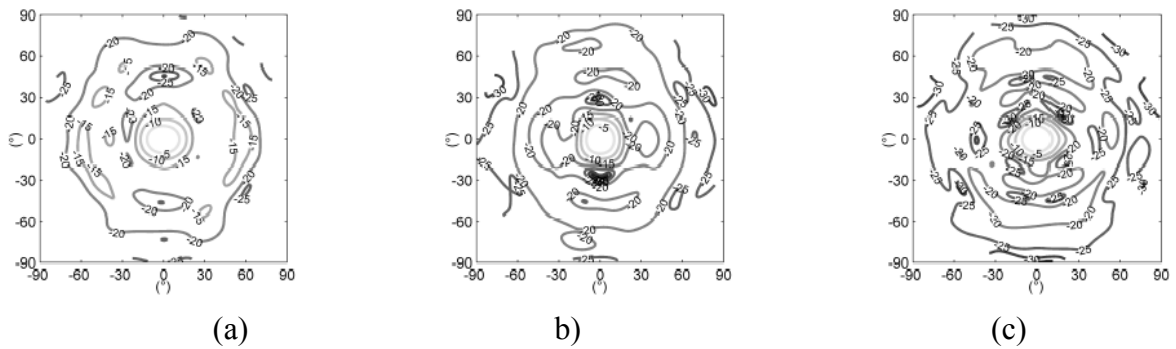
Fig. 4.12: Radiation patterns: (a) 47.2 GHz, (b) 49 GHz, (c) 50.2 GHz.

4.1.5 – Optimization procedure

The use of GO principles for the resolution of inverse problems leads to an approximate solution for the lens profile. An optimization procedure can then be implemented to improve the radiation characteristics of the lens.

Figs. 4.13 to 4.16 show the measured and computed radiation patterns, as well as the corresponding lens shape, before and after optimization, respectively.
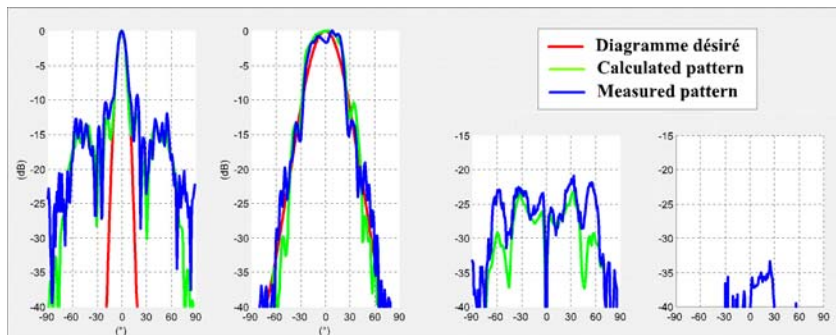
Fig. 4.13: Radiation patterns *before* optimization.
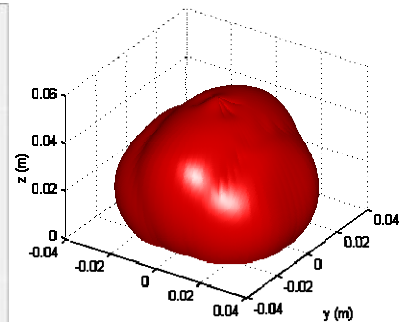
Fig. 4.14: Lens shape *before* optimization
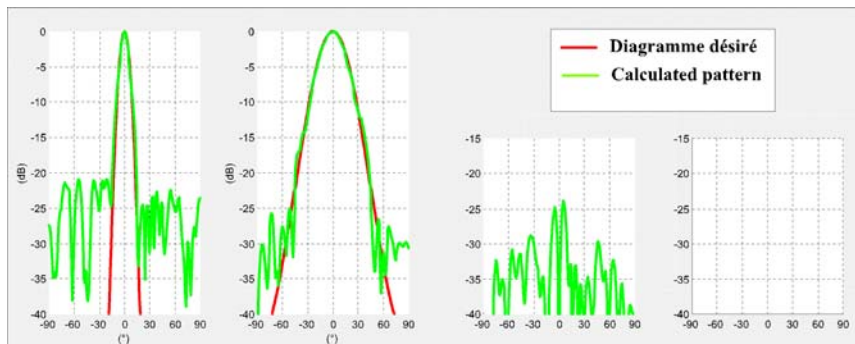
Fig. 4.15: Radiation patterns *after* optimization.
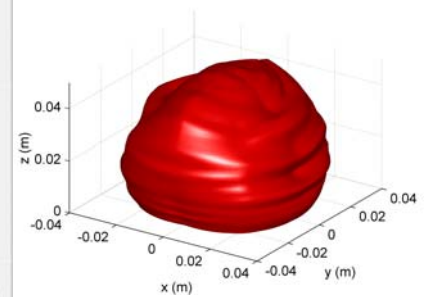
Fig. 4.16: Lens shape
after optimization

4.1.6 – References

Ph.D

Y. Cailloce, "Antennes actives et réseaux d'antennes en millimétrique", University of Rennes 1, April 1997.

B. Barès, "Analyse et synthèse d'antennes lentilles diélectriques de forme arbitraire", University of Rennes 1, scheduled in November 2004.

R. Alkhatib, "Etude de systèmes antennaires à fort gain. Applications aux fréquences millimétriques", INSA of Rennes, scheduled in December 2005.

G. Godi, "Etude et optimisation d'antennes lentilles miniatures et/ou large bande", University of Rennes 1, scheduled in December 2006.

Journal papers

G. Godi, R. Sauleau, "Performance of electrically small substrate lens antennas for millimetre-wave communications", submitted to *IEEE transactions on Antennas and Propagation*, Feb. 2004.

B. Barès, R. Sauleau, K. Mahdjoubi, L. Le Coq, « A new accurate design method for millimeter-wave substrate lens antennas for arbitrary shape», submitted to *IEEE transactions on Antennas and Propagation*, Feb. 2004.

Conferences

B. Chantraine-Barès, R. Sauleau, K. Mahdjoubi, "Accurate synthesis of millimeter wave homogeneous dielectric lenses of arbitrary shape", *2003 IEEE AP-S International Symposium,* vol. 4, pp. 518-521, Columbus, Ohio (US), 22-27 June 2003.

B. Chantraine-Barès, R. Sauleau, G. Godi, "Design of a millimeter wave lens antenna for satellite communications in Q-band", *26th ESA Antenna Workshop on Satellite Antenna Modelling and Design Tools, Innovation and Challenges, 12-14 November 2003, ESTEC, Noordwijk, The Netherlands,* pp. 229-236.

G. Godi, R. Sauleau, "FDTD analysis of reduced size substrate lens antennas", *IEEE AP-S International Symposium,* Monterey, California (US), June 20-26, 2004.

R.Alkatib, M.Drissi "Broadband Lens Antenna for Wireless Communications", *2004 IEEE AP-S International Symposium on Antennas and Propagation and USNC/URSI National Radio Science Meeting,* Monterey, California, USA on June 20-26, 2004.

R.Alkatib, M.Drissi, "Broadband Low Cost Antennas for Wireless Applications", International Conference on Information and Communication Technologies*, ICTTA'04, April 19-23, 2004, Damascus, Syria.*

4.2 – Non homogeneous lenses

4.2.1 – Main results

The Lüneburg lens represents a very attractive candidate for many applications such as multibeam antennas, multifrequency scanning and spatial scanning, due its peculiar focusing properties. The refractive index *n* follows the following radial distribution: $n^2 = 2 - r^2$, where *r* is the normalized radial position. Practically, these lenses are usually manufactured using a finite number of concentric shells. To make easier the fabrication process, the lens can also be divided in parallel slices with a specific distribution of holes to approximate the ideal distribution *n(r)*. The sphere discretization and the consecutive slices fitment are represented in Fig. 4.17a and 4.17b, respectively. (Fig. 4.17). Fig. 4.17c and 4.17d show the calculating lens assembling, and a photograph of the prototype fabricated in Teflon, respectively. It comprises 19 Teflon slices with a total number of 23047 drilled holes. The lens radius equals 150mm and the drilled hole have a diameter of 1mm.

(a)

(b)

(c)

(d)
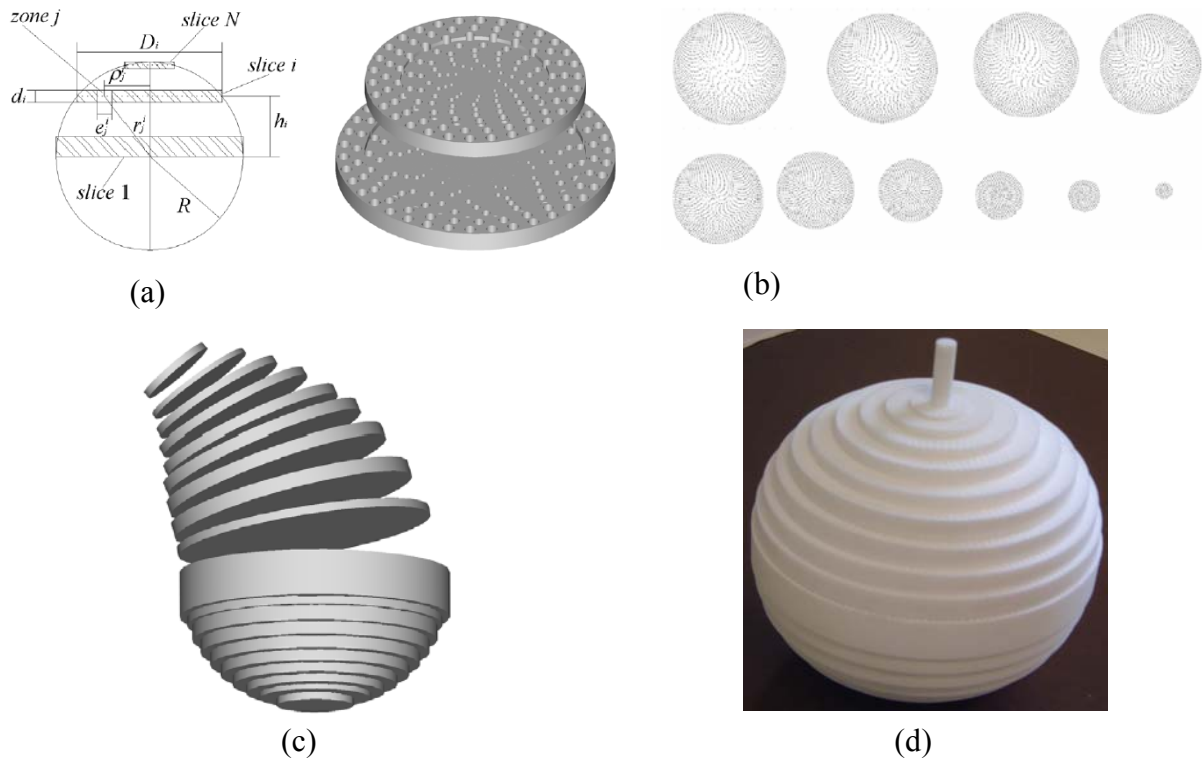
Fig. 4.17: (a) Sphere discretization of the Lüneberg lens. (b) Distribution of drilled holes in each slice. (c) Lens assembling. (d) Fabricated prototype.

The lens is illuminated by an open-ended WR28 waveguide. The measured and computed radiations patterns in E- and H-planes at 27.5 GHz and 32 GHz are represented on Figs. 4.18 and 4.19, respectively. The measured gain (Fig. 4.20) is maximum (28.5dB) at 27.5 Ghz. It is very stable over a wide frequency band. The surface efficiency varies from 50% at 26.5 Ghz down to 22% at 32 GHz. In the same way, the global efficiency (gain over directivity) decreases from 30% at 26.5 GHz down to 15% at 32 GHz.
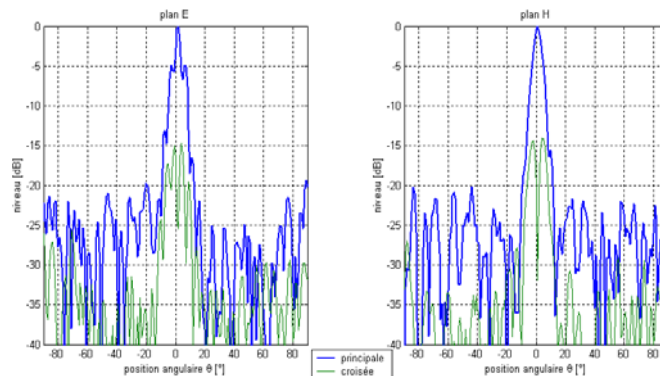
Fig. 4.18: Measured and computed radiation patterns at 27.5 GHz.
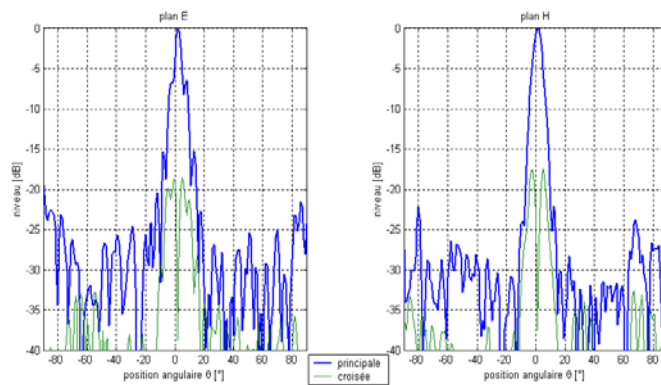
Fig. 4.19: Measured and computed radiation patterns at 32 GHz.
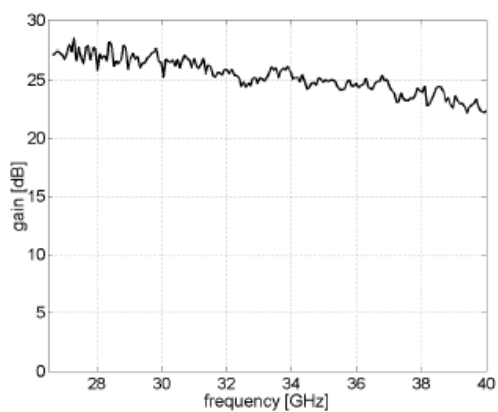
Fig. 4.20: Measured gain.

4.2.2 – References

Ph.D

S. Rondineau, "Modélisation de lentilles sphériques à gradient d'indice et sources conformes associées", University of Rennes 1, December 13, 2002.

Journal papers

S. Rondineau, A.I. Nosich, J.-P. Daniel, M. Himdi, S.S. Vinogradov, "MAR-based analysis of a spherical-circular printed antenna with a finite ground excited by an axially-symmetric probe", *IEEE Trans. Antennas and Propagation*, vol. 52, n°4, 2004.

S. Rondineau, M. Himdi, J. Sorieux, "A sliced spherical Lüneburg lens", *IEEE Antennas and Wireless Propagation Letters*, vol. 2, pp. 163-166, 2003.

Conferences

S. Rondineau, A.I. Nosich, M. Himdi, J.-P. Daniel, "Discrete Luneburg lens fed by a spherical-circular printed antenna in axisymmetrical mode – accurate analysis by MAR", *IEEE Antennas Propagat. Symp. Digest*, San Antonio, 2002.

S. Rondineau, A.I. Nosich, M. Himdi, J.-P. Daniel, "Simulation of a discrete Luneburg lens fed by a conformal printed antenna", *Proc. Int. Conf. Mathem. Methods in EM Theory (MMET*02)*, Kiev, pp. 594-596, 2002.

S. Rondineau, A.I. Nosich, M. Himdi, J.-P. Daniel, "Design of a discrete Luneburg lens fed by slot-excited spherical-circular conformal printed antenna", *Proc. European Microwave Conf. (EuMC-02)*, Milan, vol. 3, pp. 697-700, 2002.

5. Gaussian Beam Antennas

The use of Fabry-Perot (FP) cavities to enhance the directivity of a primary source is a well-known principle. This concept has been applied to design low-profile directive antennas operating in the 60 GHz band. The FP resonators are generally plano-convex in order to generate Gaussian radiation patterns, by analogy with dielectric loaded compact open resonators. This peculiar property is of particular interest for indoor wireless systems for which multipath propagation and co-channel interference should be reduced.

The properties and design rules of FP cavities are firstly described in section 5.1. Their association with guided or printed primary sources is then considered in section 5.2. Main references are finally given in section 5.3.

5.1 – Fabry-Perot Cavities

FP cavities with semi-transparent inductive metal meshes have been studied theoretically and experimentally in the 48-60 GHz band. Their main characteristics (resonant frequency, insertion losses, Q-factor) have been defined as a function the thickness of the fused quartz substrates (ε_r=3.80, tanδ<5×10^{-4}) and the grid parameters (spatial period a, width of the metal strips d). The influence of critical parameters, such as the conductivity of the metals strips, has been also investigated. Two theoretical approaches have been implemented. The first one is based on equivalent circuit modeling (only valid in the long wavelength regime); the second one relies on the Finite-Difference Time-Domain (FDTD) technique combined with periodic boundary conditions.

The validity and the accuracy of conventional transmission line models (proposed by Marcuvitz, Ulrich, Chen, Lee, Wang, …) of grids reactances have quantified. New ultra wideband formulations of wave impedances have been proposed for inductive and capacitive grids. Fig. 5.1 shows some FP resonators (of various diameters and radii of curvature) with 2D inductive metal meshes. The semi-transparent mirrors were fabricated using a lift-off process of sputtered (or evaporated) copper, chromium or aluminum thin films.

The typical characteristics of FP cavities are represented in Fig. 5.2 (fundamental resonant frequencies), Fig. 5.3 (-3dB bandwidth) and Fig. 5.4 (insertion losses) as a function of their mirror power reflectivity. In these figures, two sets of cavities are considered: the grid mirrors have a constant spatial period a and a variable filling factor d/a (set #1), and vice-versa (set #2). A recent review about FP cavities is proposed in the references (section 5.3).
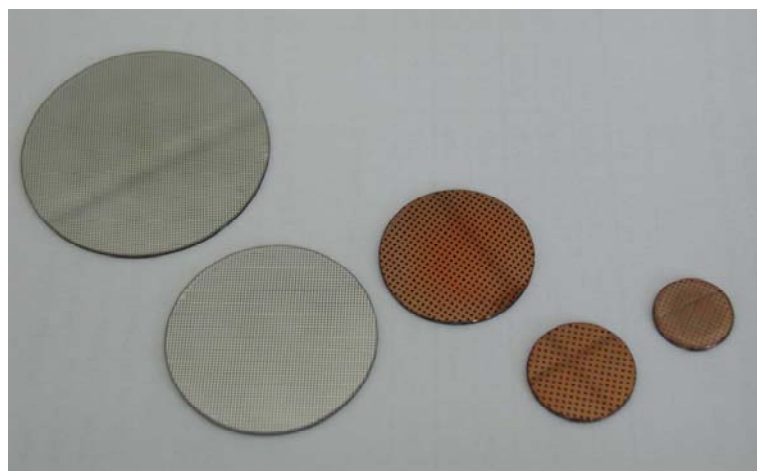
Fig. 5.1: Examples of FP cavities operating in V-band. Their diameters vary between 15mm and 50mm.
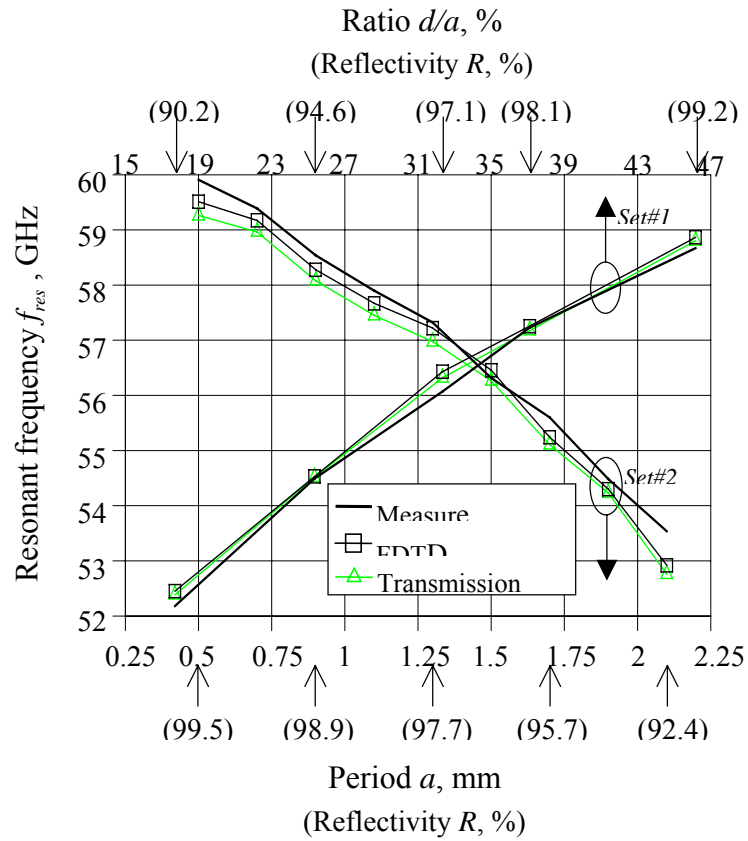
Fig. 5.2: Variation of the measured and theoretical fundamental resonant frequencies of FP cavities as a function of their mirror geometry (*a*, *d*/*a*).
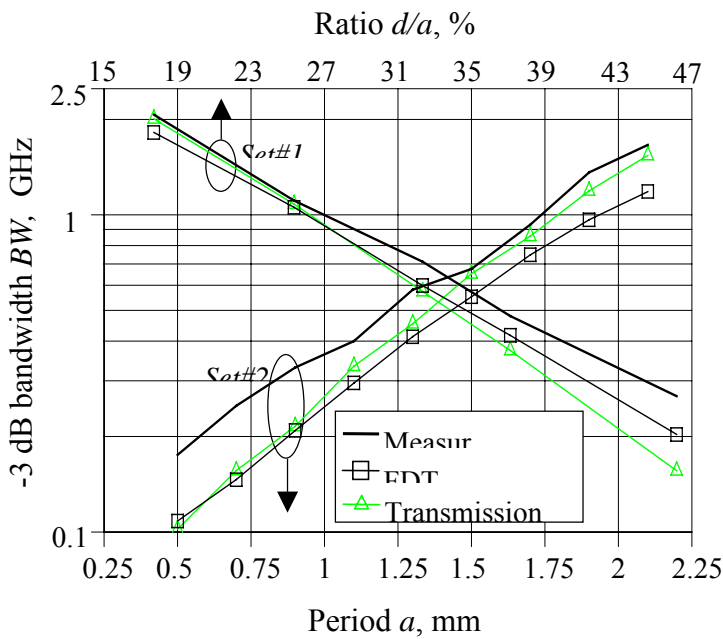
Fig. 5.3: Variation of the measured and theoretical -3dB bandwidths of FP cavities as a function of their mirror geometry (*a*, *d*/*a*).
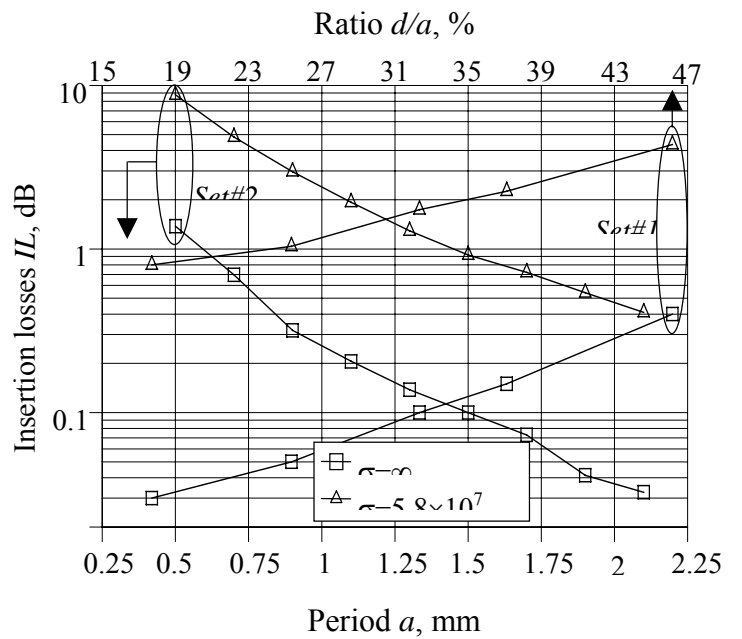
Fig. 5.4: Variation of the measured and theoretical insertion losses of FP cavities as a function of their mirror geometry (*a*, *d*/*a*).

5.2 – Gaussian Beam Antennas

As stated in the introduction of this section, the use of FP cavities enables to reduce the angular range of radiated power, resulting in directive radiation patterns. Several kinds of primary sources (wire antennas, waveguides, horn antennas, printed antennas) and metallo-dielectric Electromagnetic Bandgap (EBG) resonator superstrates have been reported in literature. At IETR, plano-convex (with a variable radius of curvature R_0) and plane-parallel ($R_0=\infty$) FP cavities have been coupled to printed and guided sources operating in linear and circular polarization in the 60 GHz band.

Fig. 5.5 and 5.6 show a schematic diagram of these antennas. The reflecting mirrors are periodic inductive metal meshes.
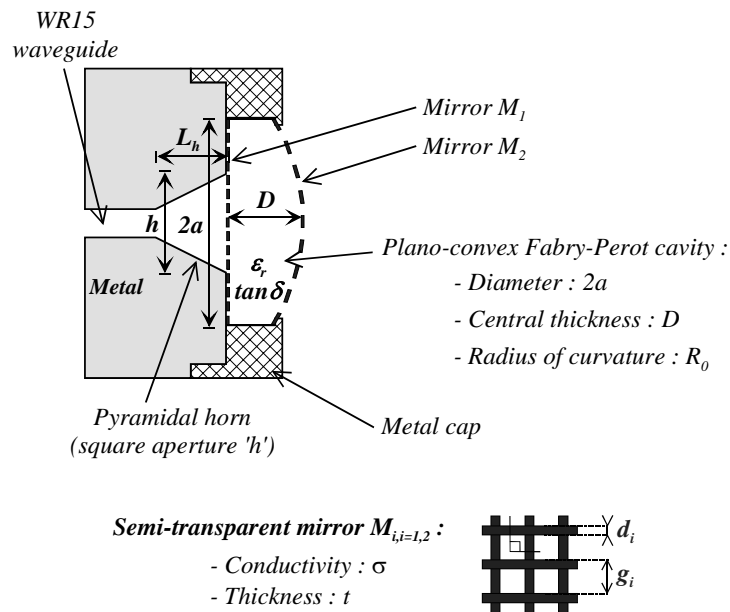
Fig. 5.5: Plano-convex FP cavity fed by a horn antenna.
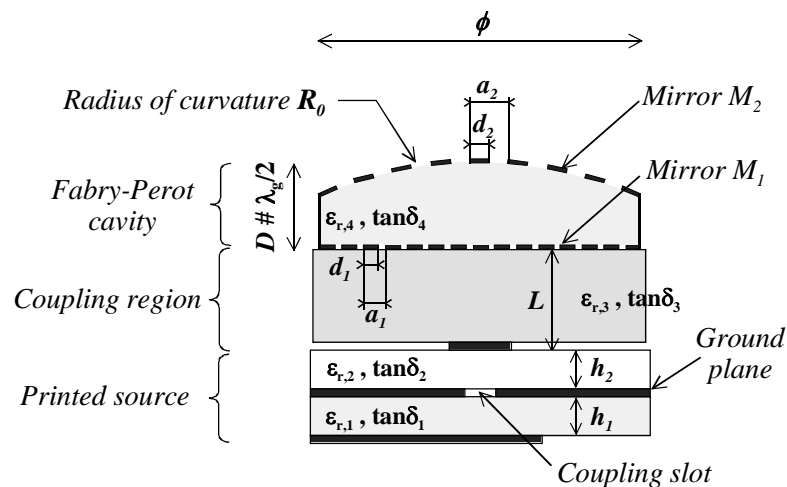
Fig. 5.6: Plano-convex FP cavity fed by an aperture-coupled microstrip patch antenna.

The typical radiation patterns of these antennas are represented in Fig. 5.7 and 5.8. They are theoretically Gaussian. These antennas are thus named Gaussian Beam Antennas (GBAs). Their radiation characteristics and input impedance have been investigated exhaustively as a function of (*i*) the topology primary source (printed or guided technology), (*ii*) the radius of curvature of the FP cavity, (*iii*) the thickness *L* of the dielectric coupling region (Fig. 5.6), and finally (*iv*) the *Q*-factor of the cavity (see Fig. 5.3). The main results are given in some journal papers given in section 5.3.

As an example, Fig. 5.7 compares the measured and computed radiation patterns of a GBA excited by a 2×2 aperture-coupled linearly-polarized microstrip antenna array. Comparison with the radiation pattern of the primary source alone clearly demonstrates the focusing effect induced by the cavity. Similar results are obtained with horn antennas (Fig. 5.8); nevertheless, the resulting structures are bulky (Fig. 5.9).

Fig. 5.7: Theoretical and experimental radiation patterns at 56.75 GHz.
(theory: red line; measurement: black line; primary source: green line)

Fig. 5.8: Theoretical and experimental radiation patterns at 59.45 GHz.
(theory: red line; measurement: black line; primary source: blue line)
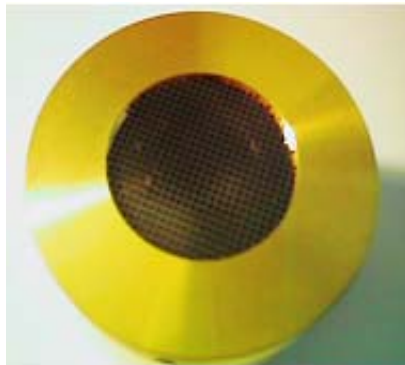
(a)
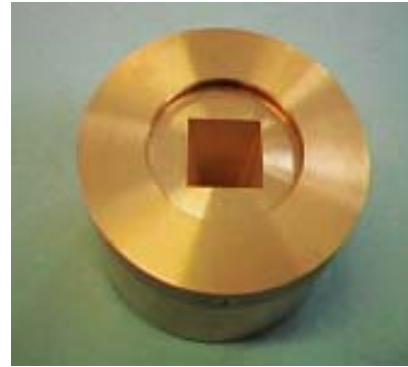
(b)

Fig. 5.9: GBA (a) fed by an electroformed gold plated horn antenna (b).

Fig. 5.10 and 5.11 show measurement setups for input impedance and radiation patterns characterizations, respectively. These setups are compatible with full two-port TRL calibration procedures.
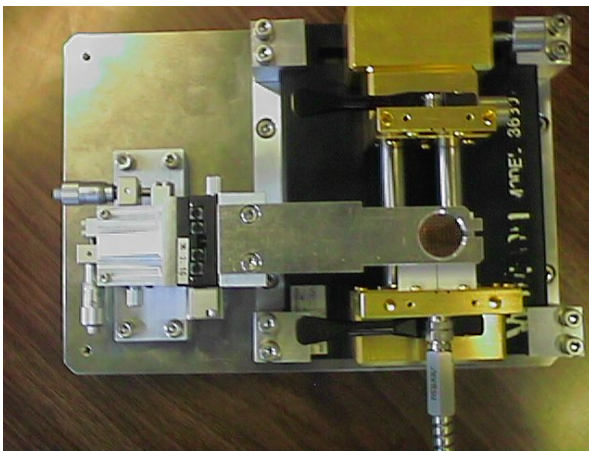
Fig. 5.10: Experimental setup for input impedance characterization. This setup enables an accurate control of the relative of the printed source and the cavity.

Fig. 5.11: Experimental setup for radiation patterns and gain measurements.

The overall radiation performance is as follows:
- The theoretical directivity varies between 15dBi and 25dBi depending on the radius of curvature of the FP resonator,
- The radiation efficiency is comprised between 20% and 70%, depending on the Q-factor of the cavity,

- *The side lobe level is generally lower than –20dB and –25dB for FP cavities fed by printed sources and guided sources, respectively.*

Moreover, to optimize the mutual coupling conditions between the cavity and the primary source, the thickness of the dielectric coupling region should be close to λ/2 (this corresponds to the opening of a defect mode inside the photonic crystal comprising the actual FP cavity and its electrical image with respect to the ground plane of the primary radiator).

Periodic reflecting mirrors behave as equiphase surfaces, as predicted by Gaussian optics. It has been demonstrated that the use of *plane-parallel* FP cavities with *non-uniform grids* (Fig. 5.12) enables to generate a Gaussian radiation pattern (Fig. 5.13). In the same way as for GBAs with *plano-convex* resonators and *periodic mirrors* (Fig. 5.7 and 5.8), the side lobe level obtained with non-uniform grids is lower than –20 dB (Fig. 5.13). Comparison with the measured pattern of the primary source alone (here a microstrip patch antenna) evidences the directivity enhancement produced by the cavity.
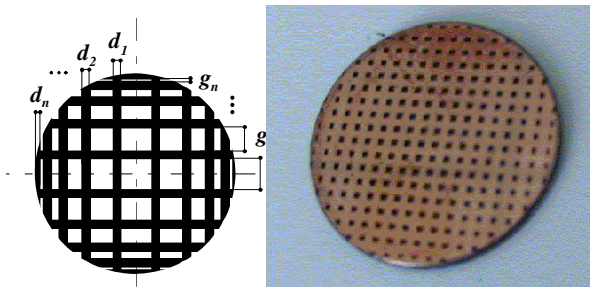
Fig. 5.12: Non-uniform grid mirror at 57.6 GHz.
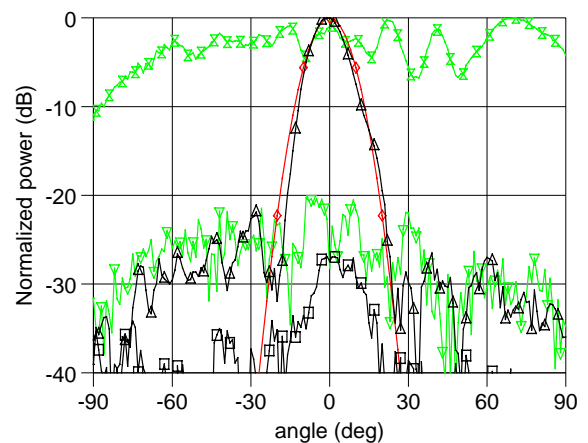
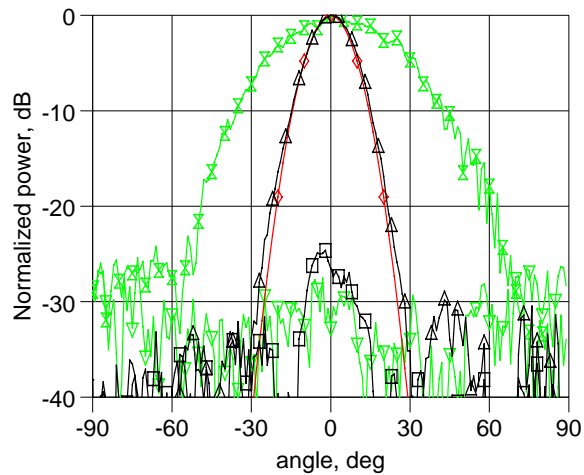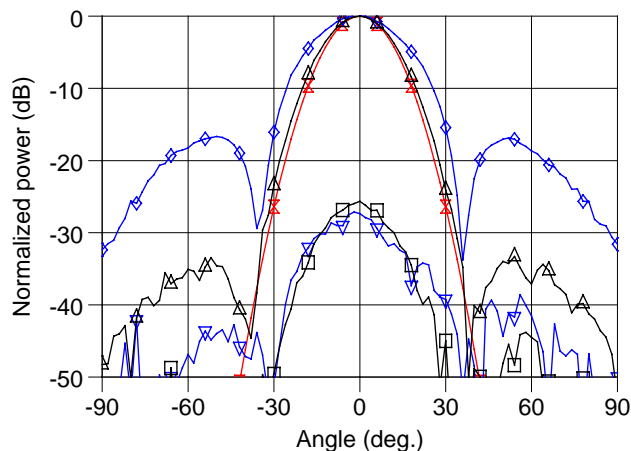Fig. 5.13: Theoretical and experimental radiation pattern in E-plane at 57.6 GHz. (theory: red line; measurement: black line; primary source: blue line)

5.3 – References

Ph.D

R. Sauleau, "Etude d'antennes imprimées et de résonateurs de Perot-Fabry en bande millimétrique. Conception d'antennes à faisceau gaussien", University of Rennes 1, December 9, 1999.

Journal papers

R. Sauleau, Ph. Coquet, J.P. Daniel, T. Matsui, N. Hirose, "Study of Fabry-Perot cavities with metal mesh mirrors using equivalent circuit models. Comparison with experimental results in the 60 GHz band", *International Journal of Infrared and Millimeter Waves*, vol. 19, n°12, pp. 1693-1710, Dec. 1998.

R. Sauleau, Ph. Coquet, D. Thouroude, J.P. Daniel, H. Yuzawa, N. Hirose, T. Matsui, "FDTD analysis and experiment of Fabry-Perot cavities at 60 GHz", *IEICE trans. Electron.*, vol. E82-C, n°7, pp. 1139-1147, July 1999.

R. Sauleau, Ph. Coquet, J.-P. Daniel, "Validity and accuracy of equivalent circuit models of passive inductive meshes. Definition of a novel model for 2D Grids", *International Journal of Infrared and Millimeter Waves*, vol. 23, n°3, pp. 475-498, March 2002.

R. Sauleau, Ph. Coquet, D. Thouroude, J.-P. Daniel, T. Matsui, "Radiation characteristics and performance of millimeter wave horn-fed gaussian beam antennas, *IEEE transactions on Antennas and Propagation*, vol. 51, n°3, pp. 378-387, March 2003.

R. Sauleau, Ph. Coquet, T. Matsui, J.-P. Daniel, "A new concept of focusing antennas using plane-parallel Fabry-Perot cavities with non-uniform mirrors", *IEEE transactions on Antennas and Propagation*, vol. 51, n°11, pp. 3171-3175, Nov. 2003.

R. Sauleau, Ph. Coquet, T. Matsui, "Low-profile directive quasi-planar antennas based on millimeter wave Fabry-Perot cavities", *IEE proc. Microwaves, Antennas and Propagation*, vol. 150, n°4, pp. 274-278, Aug. 2003.

R. Sauleau, Ph. Coquet, T. Matsui, "Near-Field Coupling Between a Printed Antenna and a Fabry-Perot Resonator: Experimental Study of the Radiation Properties at Millimeter Wave Frequencies", *Microwave and Optical Technology Letters*, vol. 38, n°6, pp. 438-443, 20 Sept. 2003.

R. Sauleau, "Fabry-Perot resonators", The Wiley Encyclopedia of RF and Microwave Engineering, to appear in 2004.

R. Sauleau,, N. Falola, "Ultra-wideband wave reactances of capacitive grids", submitted to *Microwave and Optical Technology Letters*, April 2004.

a||e

6. Reconfigurable MEMS Antennas

6.1 – Reconfigurable Antennas

MEMS technologies are of particular interest for the design of millimeter-wave reconfigurable antennas:

- polarisation diversity (linear or circular),
- pattern agility (variable directivity),
- operating frequency agility.

These studies are carried out in collaboration with IEMN (Institute of Electronic and Microelectronic of Nanotechnology, Lille, France) and with LAAS (Laboratory for Analysis and Architecture of Systems, Toulouse, France).

Fig. 6.1 shows an example of prototype with a reconfigurable radiation pattern. The reconfiguration is achieved using capacitive MEMS switches The theoretical radiation patterns are represented in Fig. 3.2 and 6.3 when the switches are in the OFF state and ON state, respectively.
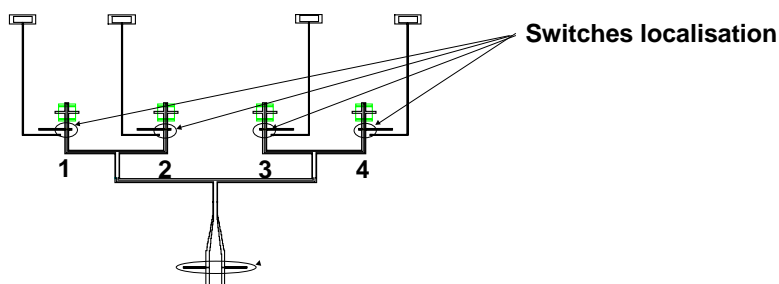
(a)
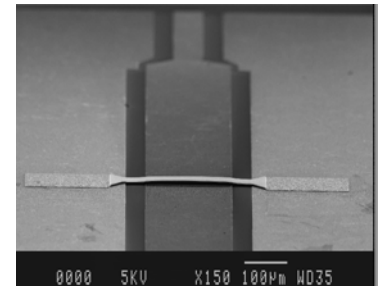
(b)

Fig. 6.1: (a) Antenna array with RF-switches integrated in the CPW feeding line for radiation pattern reconfiguration. (b) Capacitive switch fabricated at LAAS, France.

The information contained in this document should be used only for the scope of the contract for which this document is prepared.
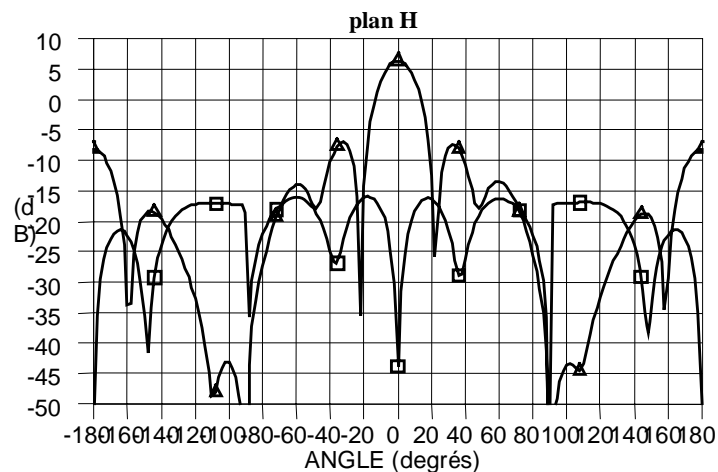
Fig. 6.2: Radiation pattern in H-plane when all switches are in the OFF state.
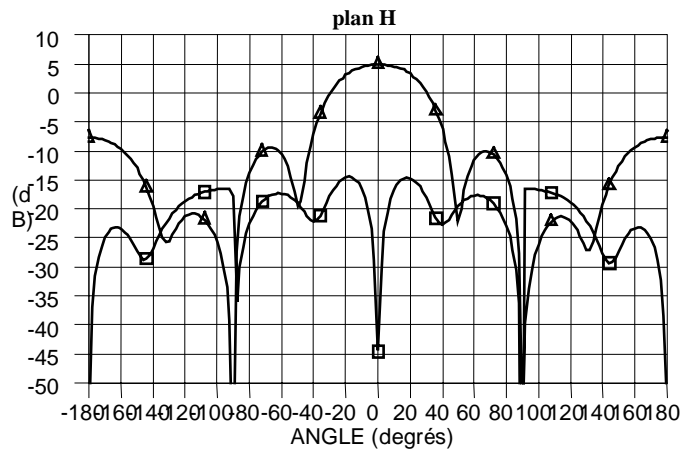
Fig. 6.3: Radiation pattern in H-plane when switches #1 and #4 are in the ON state.

Other prototypes, involving, similar or completely different technologies are currently under development. Fig. 6.4 shows a prototype with polarization agility.
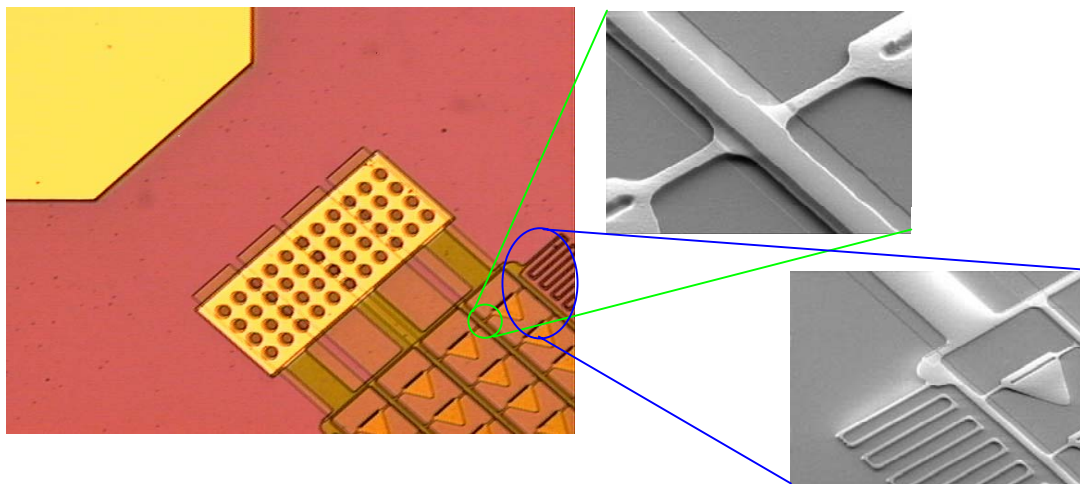
Fig. 6.4: MEMS antenna with polarization agility. The antenna has been fabricated at IEMN, France.

6.2 – References

Ph.D

L. Le Garrec, "Etude d'antennes millimétriques reconfigurables en technologie MEMS", University of Rennes 1, scheduled in December 2005.

Conferences

L. Le Garrec, M. Himdi, R. Sauleau, L. Mazenq, K. Grenier, R. Plana, "Cpw-fed slot microstrip MEMS-based reconfigurable arrays", *IEEE AP-S International Symposium,* Monterey, California (US), June 20-26, 2004.

7. Superconducting high-T_c Antennas

Superconducting microstrip antennas operating at 38 GHz have been designed by patterning ⬚ thin films epitaxially grown on single crystal substrates of ⬚ and ⬚ (⬚) ⬚ (R-sapphire) by pulsed laser deposition. Results obtained on the two types of substrates are presented and compared to a similar silver antenna. Antennas arrays and associated circuits are also described.

7.1 – Introduction

High-T_c superconductors (HTS) present some advantages in many applications [1]. In view of microwave applications, the significant parameter to evaluate thin films is the surface resistance R_s. Superconducting ⬚ presents a R_s about one hundred times lower at microwave frequencies than the best metallic material at the same cryogenic temperature [2].

We used two low loss dielectric substrates adapted to millimeter-wave frequencies specificities. At first, MgO substrate is used because of its dielectric properties at cryogenic temperatures (ε'=9.6 and $\tan\delta$=6.2×10^{-6} at 10 GHz and 77K) ; however, it is difficult to obtain required values for R_s due to the competition of two different in-plane orientations of the superconducting material, leading to an array of a high angle grain boundaries.

So, thin films of ⬚ have been grown on R-sapphire substrate with ⬚ as a buffer layer. Sapphire is an excellent candidate with a reasonable dielectric constant ($\varepsilon'_\perp$=9.4 and $\varepsilon'_{//}$=11.6) and the lowest known $\tan\delta$ ($\tan\delta$=10^{-8} at 10 GHz and 77K). It has been shown that films with R_s values in the range of 0.5-2 mΩ (at 77K and 10 GHz) can be obtained reproducibly if the thickness of the buffer layer and growth conditions are correctly controlled [3].

Experimental performance of a HTS single element microstrip patch antenna operating at ⬚ are determined using a home-made vacuum setup (Fig. 7.1) for each substrate and compared with a silver element of similar geometry in the case of MgO substrate.
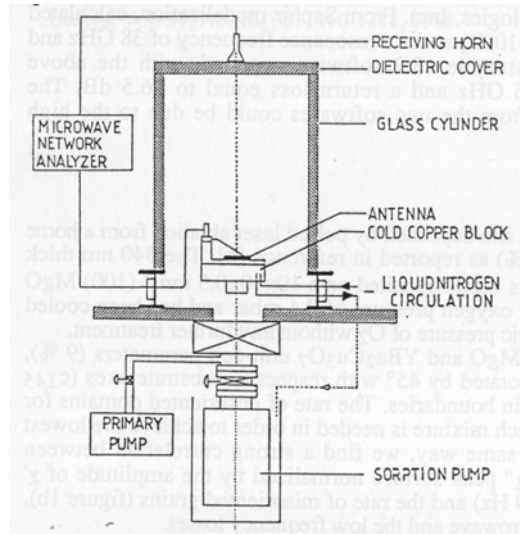
Fig. 7.1: Experimental test set for superconducting antenna measurements.

7.2 – Main results

The HTS antenna efficiency at 80 K relative to the silver one is 1.2 dB and 2.2 dB at 80 K and 300 K respectively. The reflection coefficient is presented in Fig. 7.2 [4].

For a similar antenna geometry, results obtained on R-sapphire substrate are shown from Fig. 7.3 to 7.6. We notice that this HTS antenna has the same behaviour as the one printed on a MgO substrate. However, we observe an improvement in terms of signal to noise ratio for ☐ coefficient at 300 K due to the use of a shorter cryogenic cable with better performance through the vacuum structure.
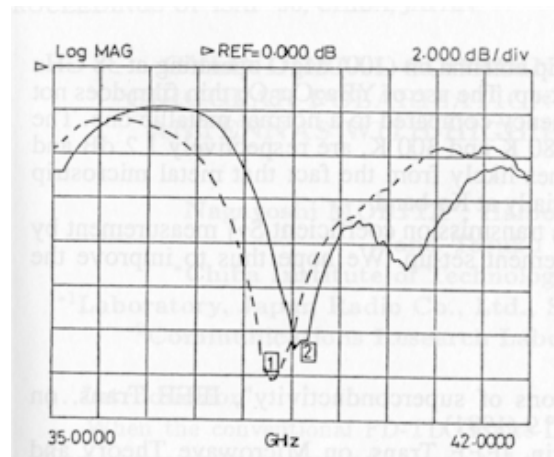
Fig. 7.2: Reflection coefficient S_{11} of antenna on silver, (1) at 300 K, (2) at 80 K.
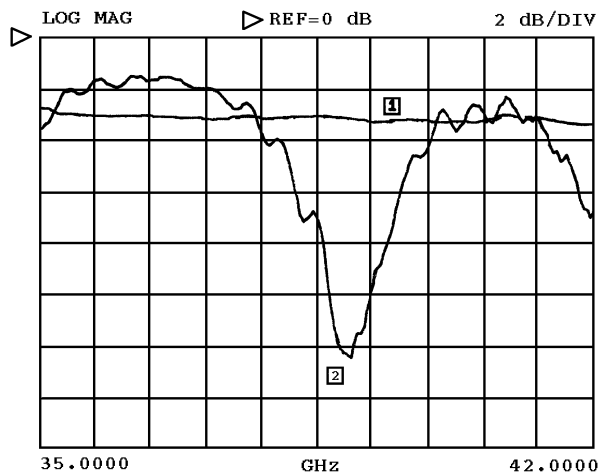
Fig. 7.3: Reflection coefficient S_{11} of the antenna printed on MgO, (1) at 300 K, (2) at 80 K.
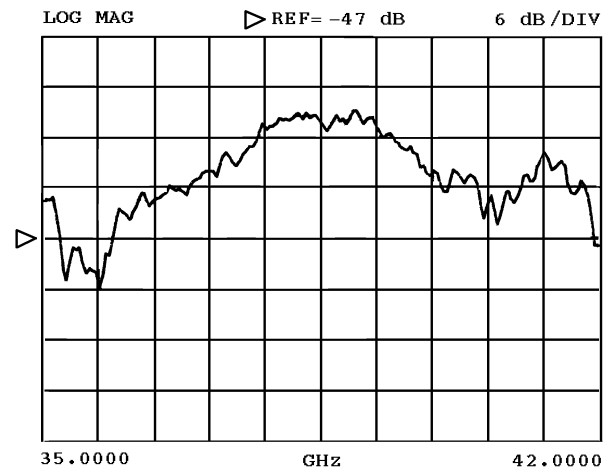
Fig. 7.4: Transmission coefficient S_{21} of the antenna printed on MgO at 80 K.
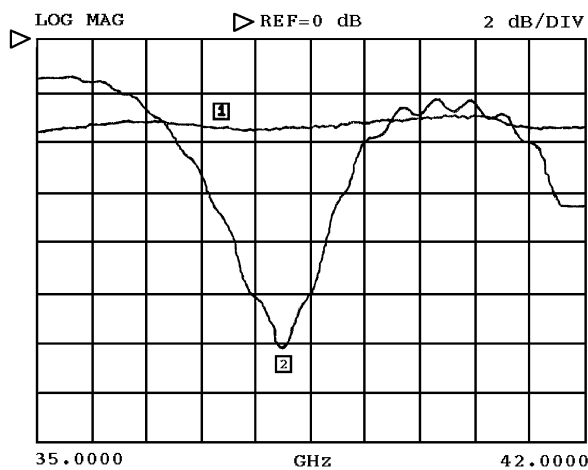
Fig. 7.5: Reflection coefficient S_{11} of the antenna printed on saphir, (1) à 300 K, (2) at 80 K.
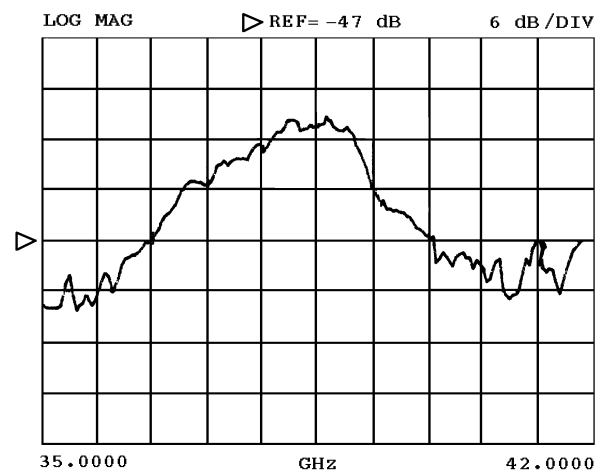
Fig. 7.6: Transmission coefficient S_{21} of the antenna printed on saphir at 80 K.

	Gain at 300 K (dB)	Gain at80 K (dB)
Ag/MgO	5.7	6.7
$YBa_2Cu_3O_7$/MgO	/	8.2
$YBa_2Cu_3O_7$/CeO_2/Al_2O_3	/	8.2

Fig. 7.7: Gains of silver antenna and superconducting antenna.

Fig. 7.8 to 7.10 show some examples of superconducting filters and antenna arrays.
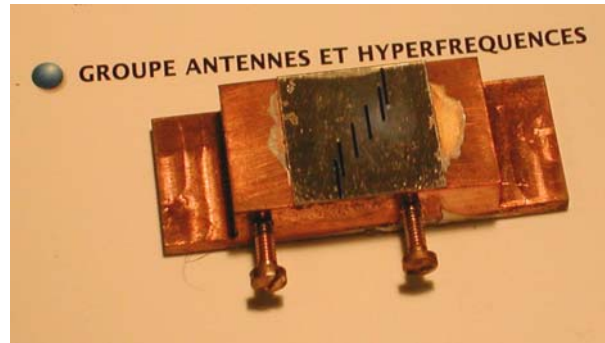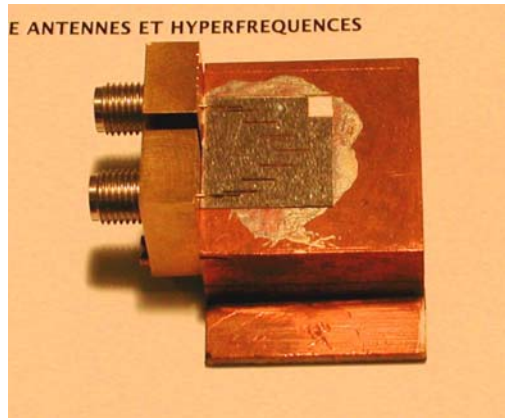
Fig. 7.8: Superconducting 4th and 7th order filters.
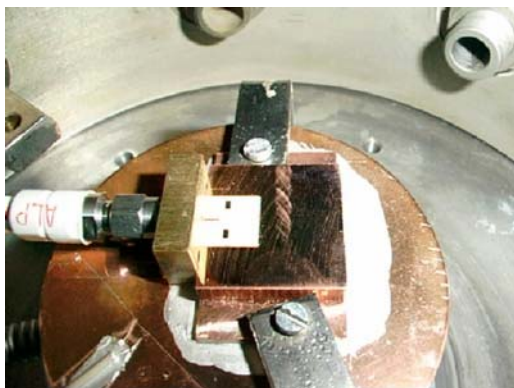
Fig. 7.9: 2 elements array located in the measurement setup.
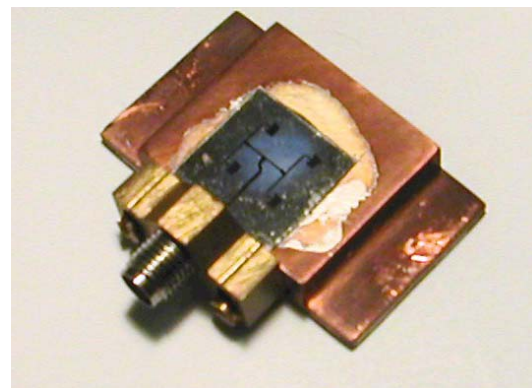
Fig. 7.10: 4 elements microstrip antenna array.

7.3 – References

[1] N. Newman, W. G. Lyons, "High-temperature superconducting microwave devices : fundamental issues in materials, physics and engineering," *J. Superconducting,* 6 (1993), pp. 119-160.

[2] M. A. Richard, K. B. Bhasin, C. Gilbert, S. Metzler, G. Koepf, and P. C. Clapsy, "Performance of a Four-Element Ka-Band High-Temperature Superconducting Microstrip Antenna," *IEEE Microwave Guided Wave Lett*., MGW-2 (1992), pp. 143-145.

[3] X. Castel, M. Guilloux-Viry, A. Perrin, C. Le Paven-Thivet, and J. Debuigne, "Correlation between microwave surface resistance, a.c. susceptibility and in-plane ordering in ⬚ thin films epitaxially grown on (100) MgO substrates," *Physica C*, 255 (1995), pp. 281-292.

[4] X. Castel, J. M. Floc'h, M. Guilloux-Viry, K. Mahdjoubi, C. Terret, A. Perrin, "Experimental results on a 38-GHz High Temperature Superconducting Microstrip Antenna," *Microwave and Optical Tech. Letters*, 13 (1996), pp. 255-259.

[5] X. Castel, S. Quété, J. M. Floc'h, M. Guilloux-Viry, A. Perrin, C. Terret, J. Citerne, "Millimeter Superconducting High-Tc Antennas on Low Dielectric Losses Substrates : (100) MgO and R-plane Al_2O_3", 1998, *EuMC'98.*

8. Conclusions

This report summarizes research activities of IETR (Rennes, France) on millimeter-wave antennas.

Apart specific requirements for the electromagnetic analysis and optimization of complex antennas systems (involving for instance multi-scale approaches – see our contributions for modeling / Optimization integrated activities), future prospects could deal with:

- **Smart focusing antennas** (reflectarrays, lenses, reflector antennas, dielectric antennas) for various applications (space, automotive, …),
- **3D antennas** based on **microtechnologies**,
- **Reconfigurable antenna structures** using **agile materials**,
- **Reconfigurable antenna structures** based on **MEMS technologies**,
- **Smart materials** (**EBG** and **metamaterials**) and sheets, and applications to mm-wave and sub-mm wave antennas (radiation patterns and gain improvement, …).

Lens Antenna Benchmarking Report

(COMPACT Ka-BAND ANTENNA for GLOBAL COVERAGE

from LEO SATELLITES)

Institut d'Electronique et de Télécommunications de Rennes

Instituto Superior Técnico/IT

December 2005

Contributors

Ronan Sauleau
IETR
Université de Rennes 1
Campus de Beaulieu
Avenue du Général Leclerc
35042 – RENNES Cedex
FRANCE
Ronan.Sauleau@univ-rennes1.fr
Tel: +33 2 23 23 56 76
Fax: +33 2 23 23 69 69

Prof. Carlos A. Cardoso Fernandes
Instituto de Telecomunicações / IST
Torre Norte
Av. Rovisco Pais, 1
1049-001 LISBOA
PORTUGAL

carlos.fernandes@lx.it.pt
Tel: 21 841 84 81
Fax: 21 841 84 72

Gaël GODI
IETR
Université de Rennes 1
Campus de Beaulieu
Avenue du Général Leclerc
35042 – RENNES Cedex
FRANCE
gael.godi@univ-rennes1.fr
Tel: +33 2 23 23 58 12
Fax: +33 2 23 23 69 69

Prof. Jorge R. Costa
Instituto de Telecomunicações / IST
Torre Norte
Av. Rovisco Pais, 1
1049-001 LISBOA
PORTUGAL
jorge.costa@lx.it.pt
Tel: 21 841 80 91
Fax: 21 841 84 72

Ludovica Collacciani

Instituto de Telecomunicações / IST
Torre Norte
Av. Rovisco Pais, 1
1049-001 LISBOA
PORTUGAL

1. OBJECTIVES

The main objective of this preliminary report is to investigate and discuss the feasibility of designing axis-symmetrical and 3D compact double-shell lens antennas.

2. PROJECT SPECIFICATIONS

The end-application that will be used to support this benchmark is a compact Ka-band lens antenna for global Earth coverage. Basic specifications are given in Table 1:

#	Frequency	26 GHz
1	VSWR on 50 Ω	≤ 1.5:1 (≤-14dB)
2	Polarization	RHCP
3	Elevation aperture	0 - 65° off-nadir
4	Gain template in elevation plane	< -8 dBi at 0°
		> -5 dBi at 40°
		> +5.5 dBi at 65°
5	Azimuth template (two alternatives)	a) Omnidirectional
		b) The one providing the best possible gain
6	Axial Ratio off-nadir angles	< 7 dB @ 0-70°
7	Materials	ECCOSTOCK K=10
		ECCOSTOCK K=3
8	Weight	< 200g
9	Diameter	< 70 mm

Table 1 – Lens target specifications.

3. DESIGN DESCRIPTION

Two alternative approaches will be evaluated, one based on an axial-symmetric design (eventually involving two materials), and another one based on a 3D lens (using one or two materials) producing higher gain.

3.1 Axial symmetric lens

This solution is composed of a printed feed caped by a dome lens. The feed is a patch antenna with right-hand circular polarization. The patch used is based upon the quasi-square printed antenna configuration with the feeding point in the patch diagonal [1]. The dome antenna is made of ECCOSTOCK K=10 with both an inner and outer quarter wavelength matching layer of ECCOSTOCK K=3. The shape of the dome lens was optimized for the desired Azimuth template.

3.1.1 Patch antenna feed

The microstrip antenna will be manufacture from a Duroid 5880 wafer with permittivity ε_r=2.2 and 10mil (corresponding to 0.254mm) of height. The antenna will be coaxially fed with a EZ-86 50Ω coaxial cable with an inner conductor of 0.51mm of diameter and dielectric diameter of 1.65mm.

The microstrip antenna will be used with a dome lens and there will be no direct contact between the patch and the dielectric material of the lens. Therefore is reasonable accurate to design the patch individually without the lens considering that it is radiating into unbound air. The patch antenna was designed, simulated and optimized using ENSEMBLE DESIGNER V1.1 software. The antenna dimension and feeding point were optimized with the goal of minimizing both the cross-polarization and the input impedance mismatch with a coaxial feeding cable of 50Ω. The obtained dimensions are indicated in Figure 1. The patch corresponds to the green almost square while the underneath brown patch is intended to act has the ground plane. The finite ground layer has 4 times the area of the patch. During the optimization it was observed that best performance appeared when the feeding point was near but not in the patch diagonal.

Figure 2 presents the antenna input impedance and the corresponding amplitude of the reflection coefficient for a 50Ω cable. In Figure 3 one can observe the left-hand circular cross-polarization level in the z-axis (θ=0º) and the axial ratio in the same axis. The radiation pattern of the left and right hand polarized electrical field at 26GHz is presented in Figure 4 in both φ=0º and φ=90º planes.
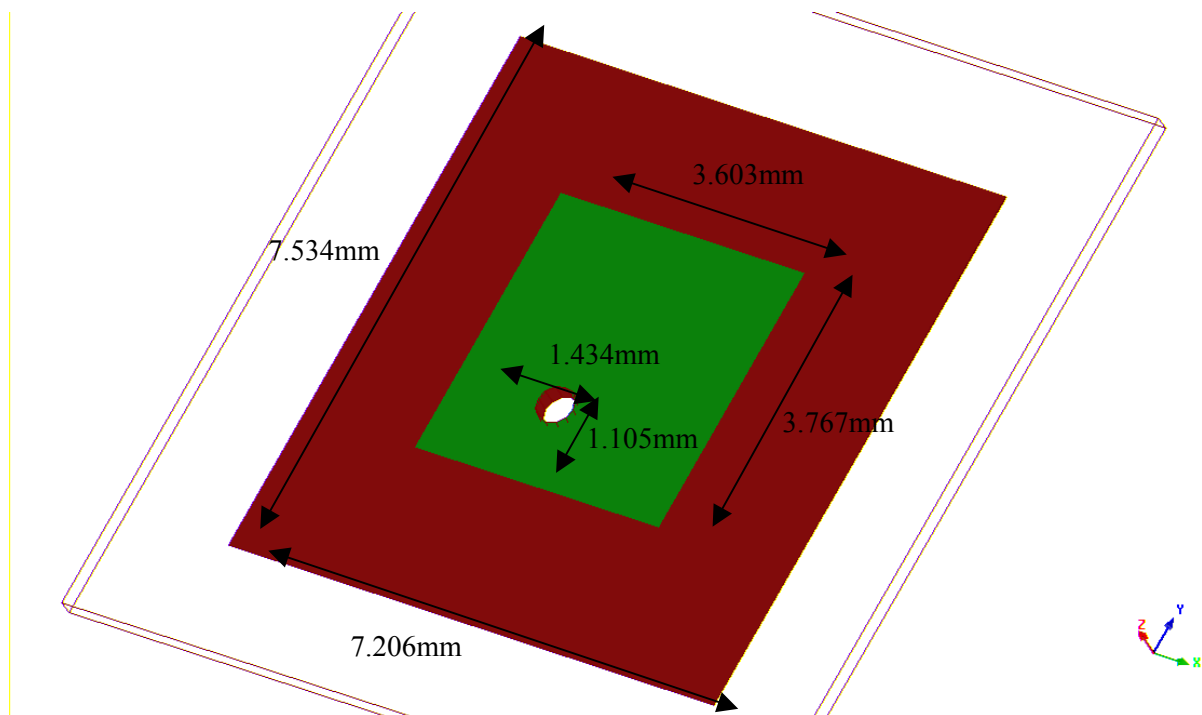
Figure 1 – Patch antenna feed dimensions.

dB

(a)

(b)
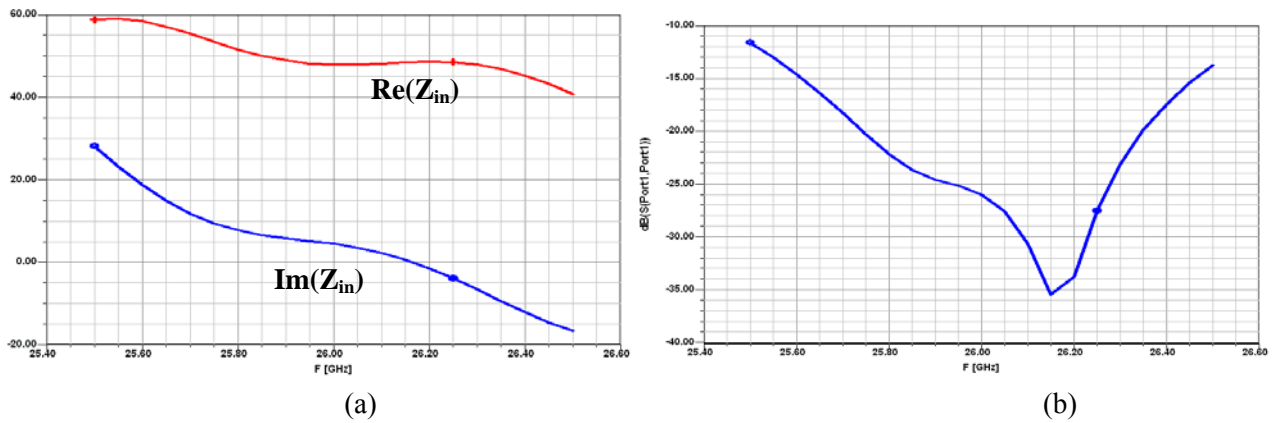
Figure 2 – (a) Input impedance; (b) Reflection coefficient.

(a)

(b)
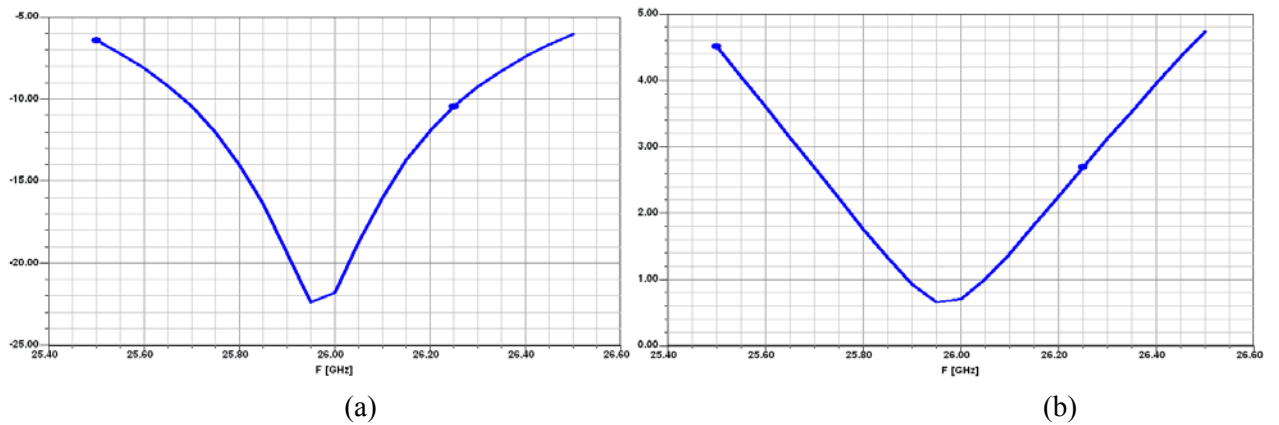
Figure 3 – In the z-axis: (a) cross polarization; (b) axial ration.

(a)

(b)
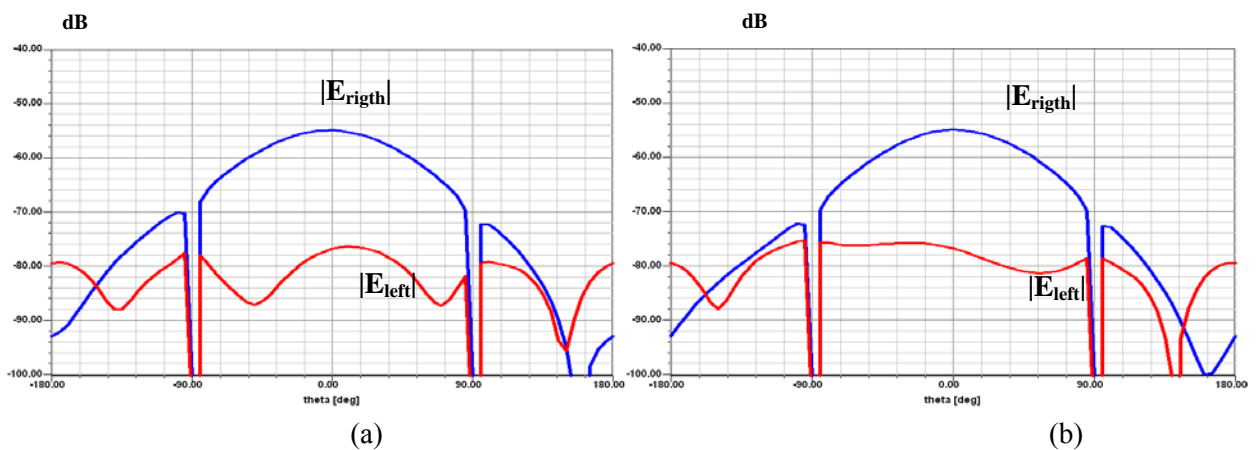
Figure 4 – Right and left polarization electric field at 26GHz in the plane (a) $\phi=0°$; (b) $\phi=90°$.

3.1.2 Dome lens

A dome lens is placed above the patch antenna in order to modify the radiation pattern according to the desired azimuth template. The lens is axial symmetric and made of ECCOSTOCK K=10. In order to reduce the internal reflections in the lens interfaces both an inner and other matching layer of ECCOSTOCK K=3 are added to the lenses surface. This is done to maximize the lens radiation efficiency.

An initial profile of the lens is obtained from a direct approach based upon the Geometric-Optics formulation [2], see Figure 5(a). The lens profile was then optimized to try to approach the radiation pattern closer to the specified target. The new obtained profile is presented in Figure 5(b).

(a)　　　　　　　　　　　　　　　　　　(b)
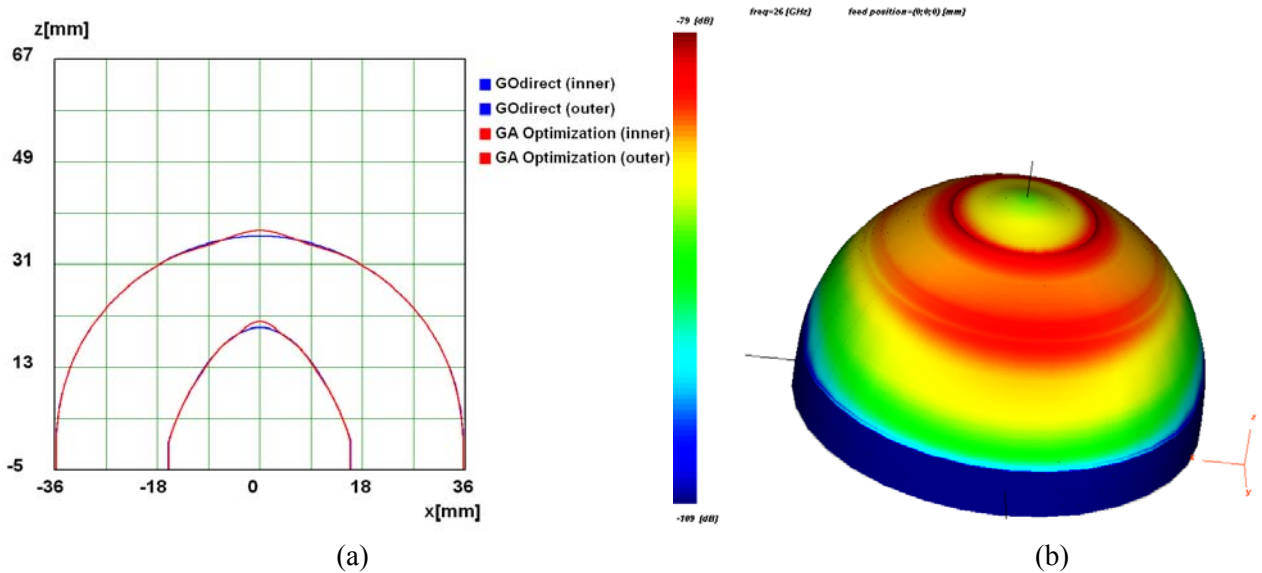
Figure 5 – (a) Lens profile; (b) equivalent electrical current amplitude in the outer shell of the GA optimized lens.

The radiation pattern of both the initial lens and the optimized one are presented in Figure 6 and Figure 7. It was chosen to present the result for the desired right-hand polarization component and for the correspondent left-hand cross polarization component.
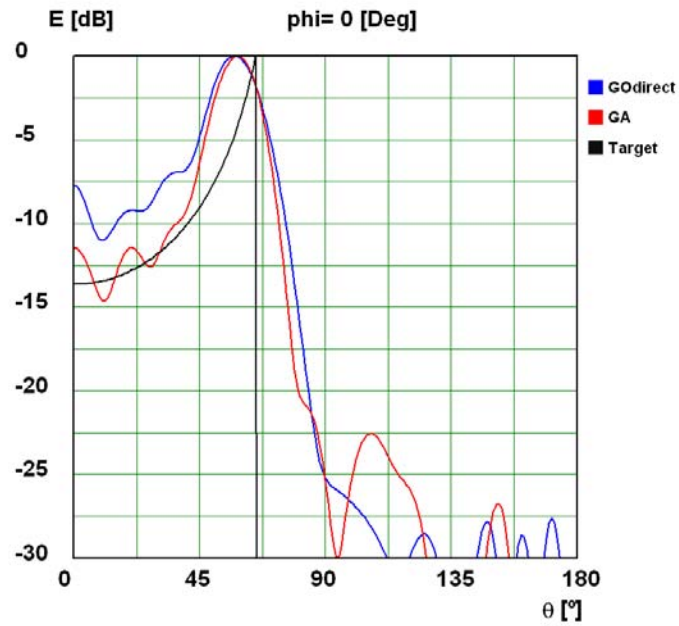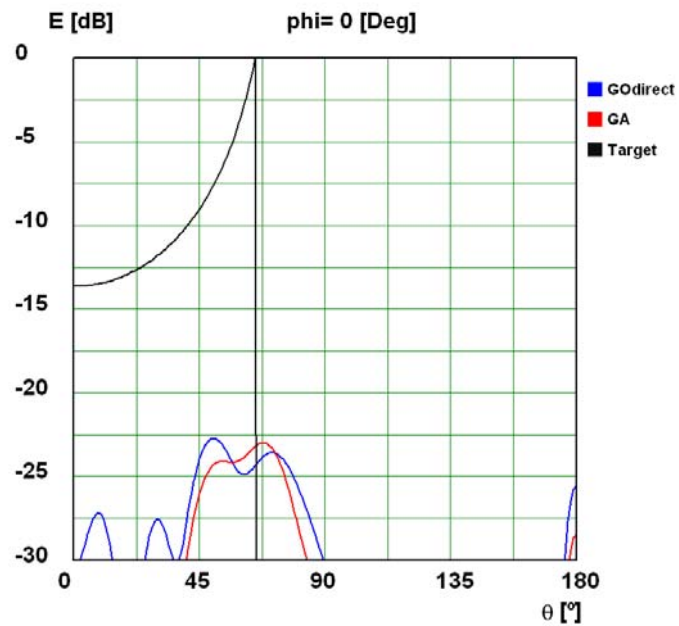
Figure 6 – Radiation pattern at φ=0º (a) RHCP electrical field component; (b) LHCP electrical field component.

(a)   (b)
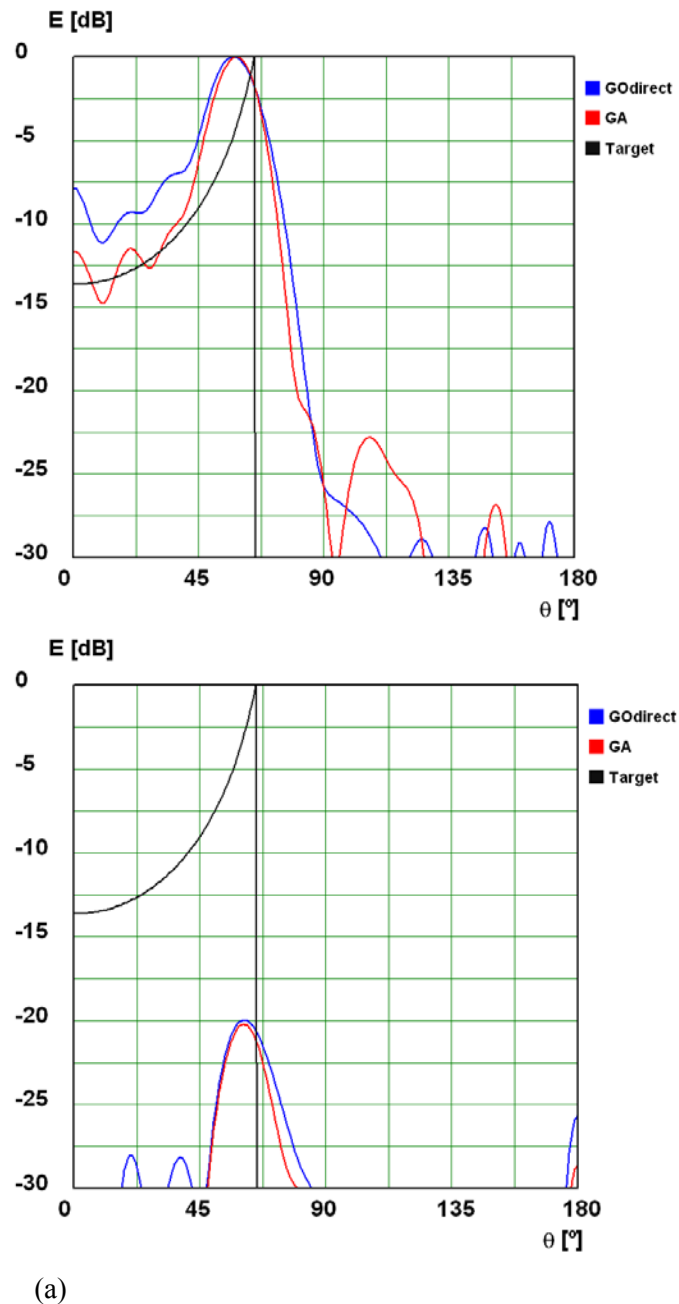
Figure 7 – Radiation pattern at ϕ=90º (a) RHCP electrical field component; (b) LHCP electrical field component.

The axial ratio of the radiated fields in both ϕ=0º and ϕ=90º planes is presented in Figure 8.

(a)   (b)
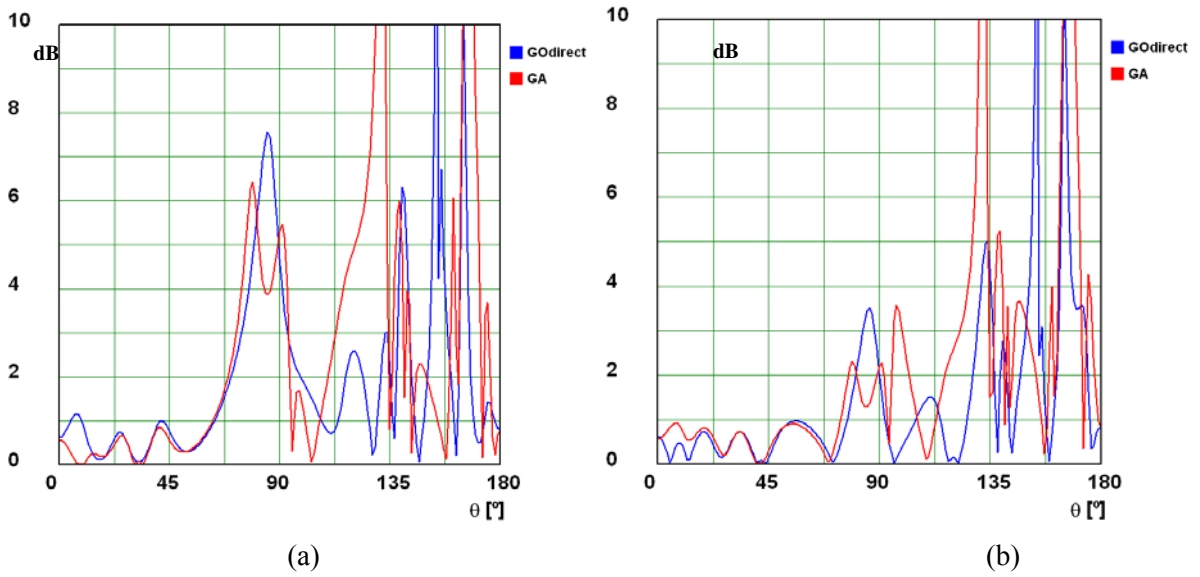
Figure 8 – Axial Ratio (a) ϕ=0º; (b) ϕ=90º.

Considering that the density of ECCOSTOCK K=10 is 2.2 g/cm^3 the weight of both lenses is presented in Table 2. It was also calculated the gain of the radiation patterns.

Table 2 – Parameters of the design lenses

	GO lens	GA optimized lens
Weight [g]	239.14	238.7
Directivity [dBi]	7.66	8.35
Gain [dBi]	7.59	8.28

3.1.3 Lens sensitivity to permittivity variations

The lens will be fabricated from materials to be bought from EMERSON & CUMING. For this material the supplier indicates that the permittivity value has an uncertainty of $\pm$ 3% [3]. Therefore, it is important to perform simulations to access the influence of the variation in the permittivity value upon the performance of the lens. In Table 3, one can observe the dependence of the GA optimized lens gain with variations in the dome permittivity value up to $\pm$ 6%. It was verified that similar variations in the matching layer did not produce significant modifications in the lens performance.

Permittivity	Gain [dBi]	Cost	Rad. Pattern	Permittivity	Gain [dBi]	Cost	Rad. Pattern
K=9.4	8.2	33.84		**K=10.1**	8.29	29.07	
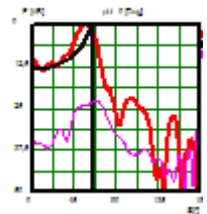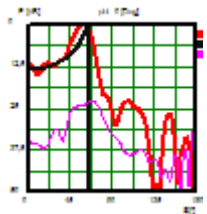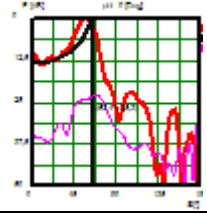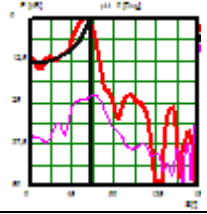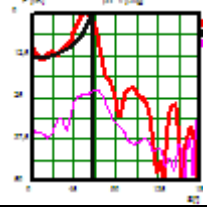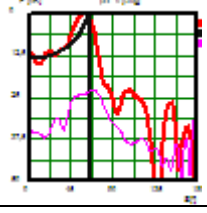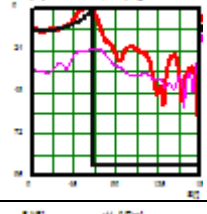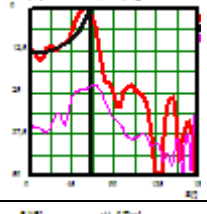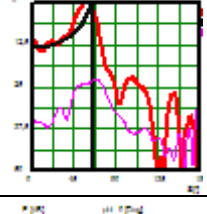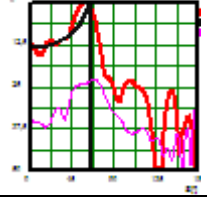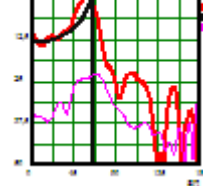
K=9.5	8.22	32.92		**K=10.2**	8.31	28.61	
K=9.6	8.23	32.15		**K=10.3**	8.32	28.22	
K=9.7	8.24	31.58		**K=10.4**	8.34	27.79	
K=9.8	8.26	30.91		**K=10.5**	8.35	27.48	
K=9.9	8.26	30.18		**K=10.6**	8.35	27.30	
K=10	8.28	29.59					

Table 3 – GA optimized lens sensitivity to the permittivity variation

Table 3 also presents a cost value which indicates the proximity of the obtained radiation pattern to the desired target curve. The lower the cost the closer is the radiation pattern to the target. For a perfect match the cost value is zero. The radiation pattern of the RHCP field component (red line) and the LHCP component (magenta line) are both presented in Table 3, along with the target curve (black line), for the different values of permittivity.

From the results in Table 3, one can conclude that the presented lens design can maintain an adequate and stable performance within the permittivity value variation indicated by the supplier. One can observe in Figure 9 that for the extreme permittivity values of Table 3, the correspondent lens radiation patterns are very similar.
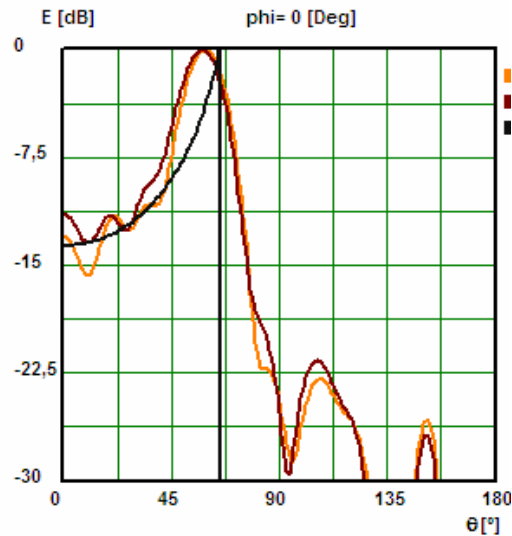
Figure 9 – GA optimized lens RHCP radiation pattern at $\phi=0^o$ for K=9.4 (darker line) and K=10.6 (brighter line).

3.2 Generic 3D-lens antennas, circular polarization

This antenna is composed of a printed feed exciting a double-shell MACOR (ε_r=5.67) / Rexolite (ε_r=2.53) shaped lens. No matching layer are taken into account. The shape of each shell was optimized for the desired template in one phi-cut-plane.

3.2.1 Patch antenna feed, circular polarization

The primary feed is a conventionnal aperture-coupled rectangular patch antenna fed by a microstrip line (Figure 9). The patch antenna operates in left-handed circular polarization with a minimum axial ratio at 26 GHz. It is designed to to radiate into lenses with an inner core made of MACOR (ε_r=5.67). It is worth mentionning that the optimization of the feed (choice of the topology, etc.) should be investigated later on. A primary source for operation in right-handed circular polarization has been designed and lead to the same results as the left-handed circular polarized antennas.
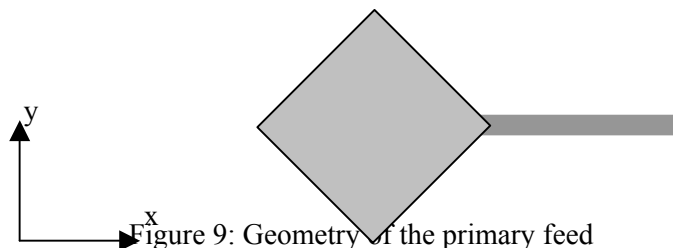
Figure 9: Geometry of the primary feed

FDTD results for the feed radiating in an half space of MACOR are given in Figures 10 and 11.
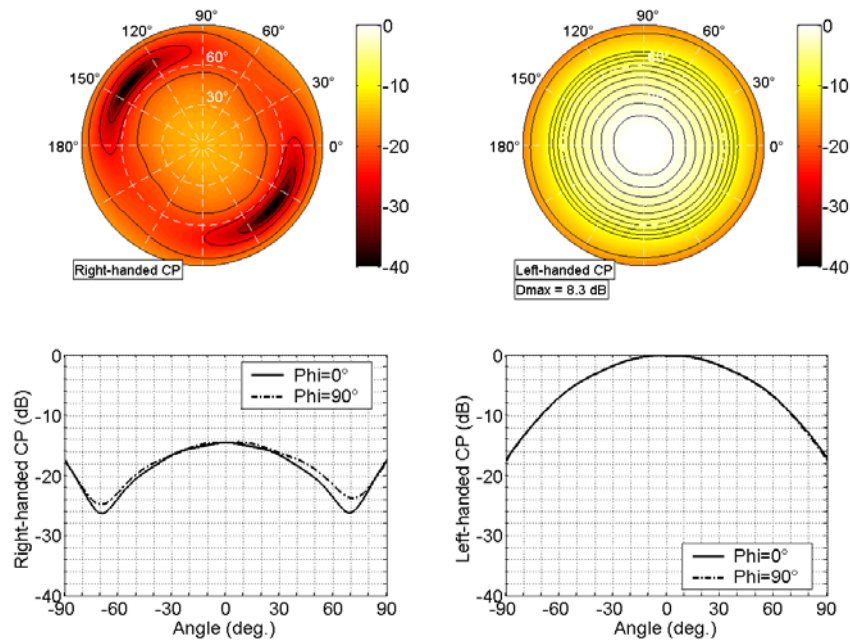
Figure 9: FDTD far-field patterns computed at 26 GHz
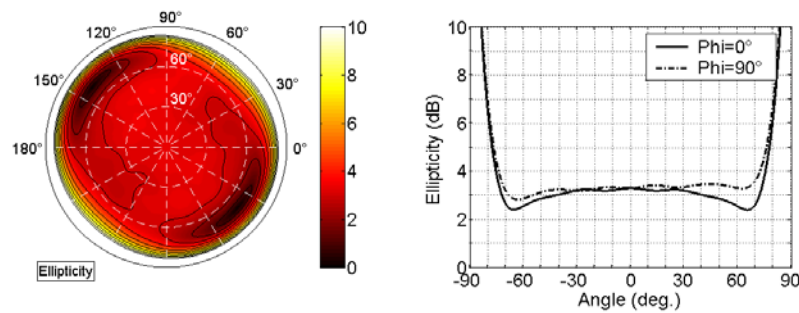
Figure 11: Ellipticity of the feed (FDTD results at 26 GHz)

3.2.2 Generic 3D lens, circular polarization

The far-field template is represented in Figure 12 (shaped for φ=0° and maximum gain at θ=65° for φ=0°). Additional information should be provided by ALCATEL ALENIA SPACE for the design of the final prototype.
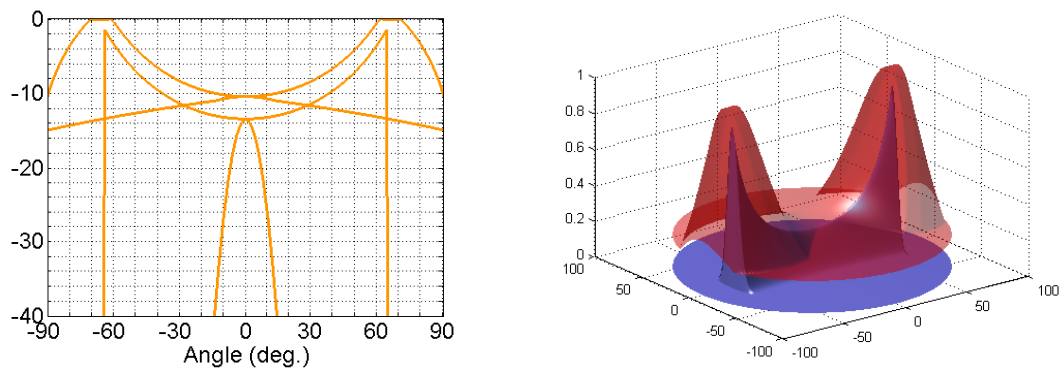
Figure 12: Left : Desired amplitude template in cut planes φ=0° and φ=90°. Right : 3-D view

A 3-D lens is designed with a genetic algorithm (GA) combined with a geometrical / physical optics kernel (GO/PO) [4]. Mechanical contraints (convex shapes) are included in the optimization for manufacturing purposes.

The internal reflections are not taken into account in the GO/PO computations.

The optimized lens shape is represented in Figures 13 and 14.
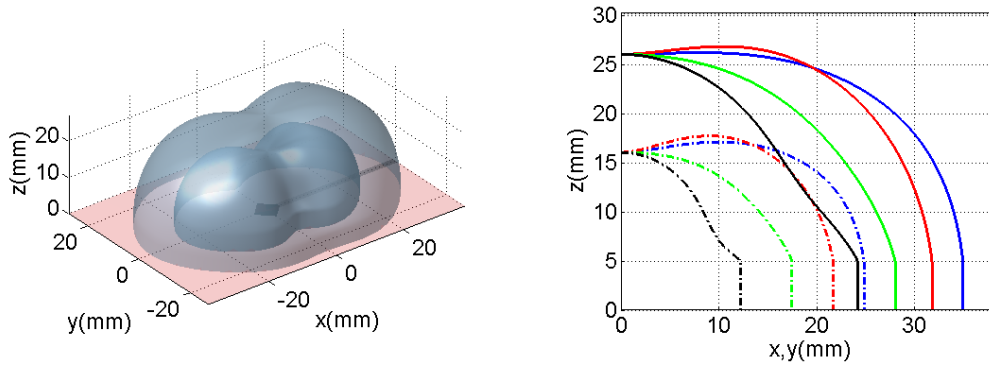
Figure 13: 3-D shape and cut-planes (φ=0°, 30°, 60°, and 90°) of the lens
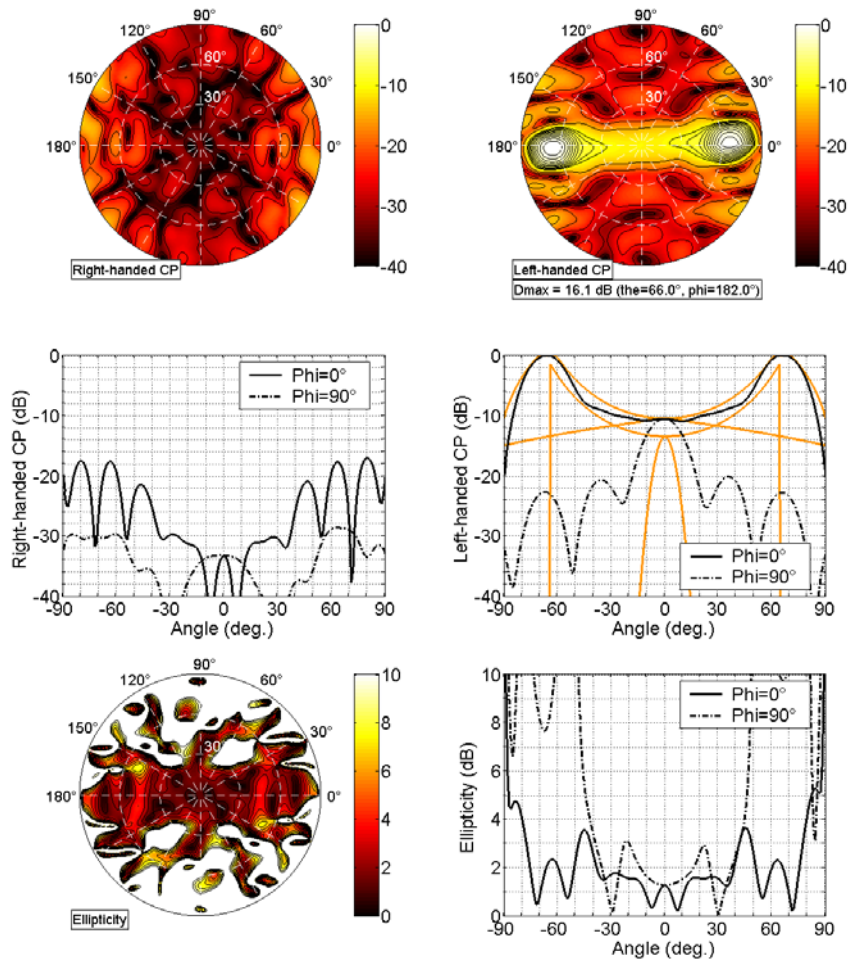
Figure 14: Far-fields and ellipticity of the lens computed at 26 GHz with GO/PO

Comparison with FDTD computations is given in Figure 15.
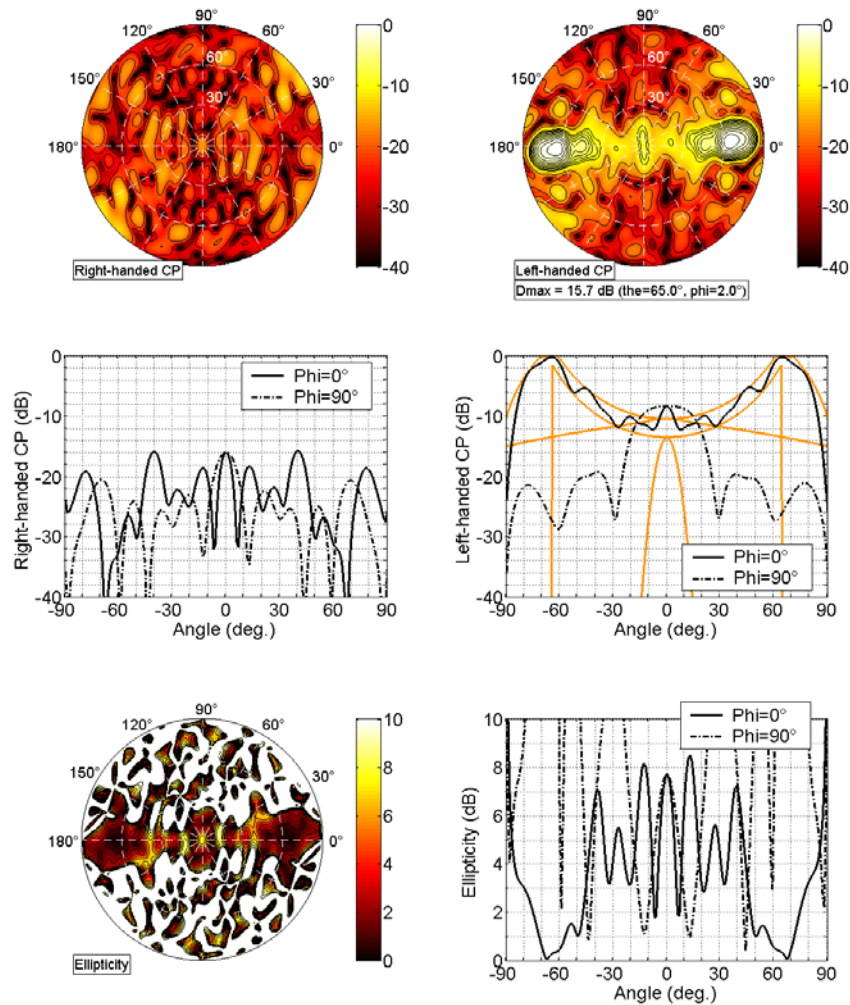
Figure 15: Far-fields and ellipticity of the lens computed at 26 GHz with FDTD

3.3 Generic 3D-lens antenna, linear polarization

Figure 15 shows that that axial ratio is strongly affected by internal reflections in the boresight direction. A linear polarization generic 3D-lens antenna has been designed to investigate this depolarization effect.

3.3.1 Patch antenna feed, linear polarization

The primary feed is a conventional aperture-coupled rectangular patch antenna fed by a microstrip line (Figure 16). The patch antenna operates in linear polarization with a resonant frequency of 26 GHz. It is designed to radiate into lenses with an inner core made of MACOR (ε_r=5.67).
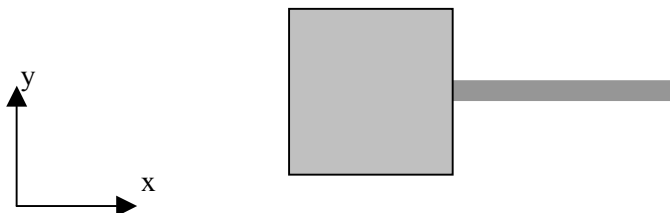
Figure 16: Geometry of the primary feed

FDTD results for the feed radiating in an half space of MACOR are given in Figure 17.
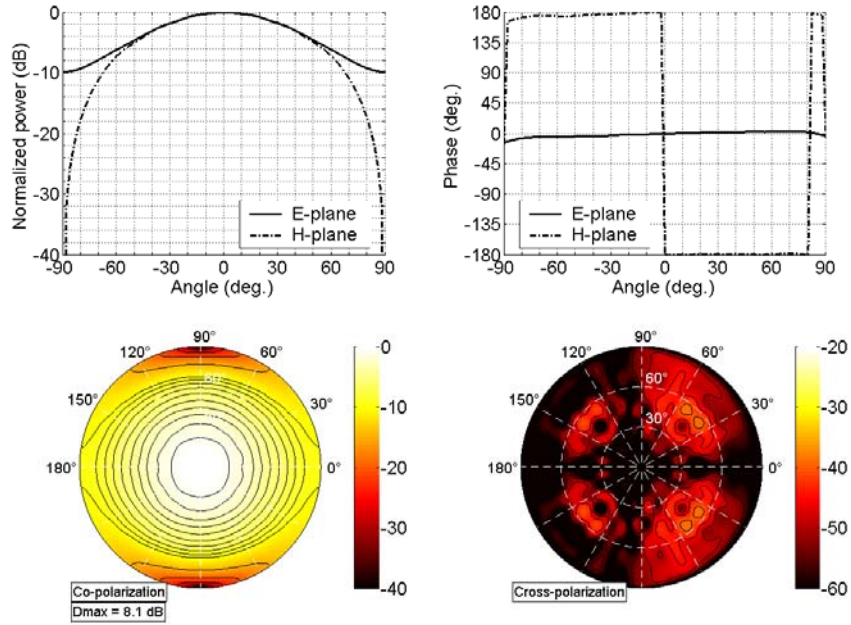
Figure 17: FDTD far-field patterns computed at 26 GHz

3.3.1 Generic 3D lens, linear polarization

The far-field template presented in section 3.2.2 is used to design a lens antenna with linear polarization. The optimized lens shape and the far-field results are represented in Figures 18 and 19.
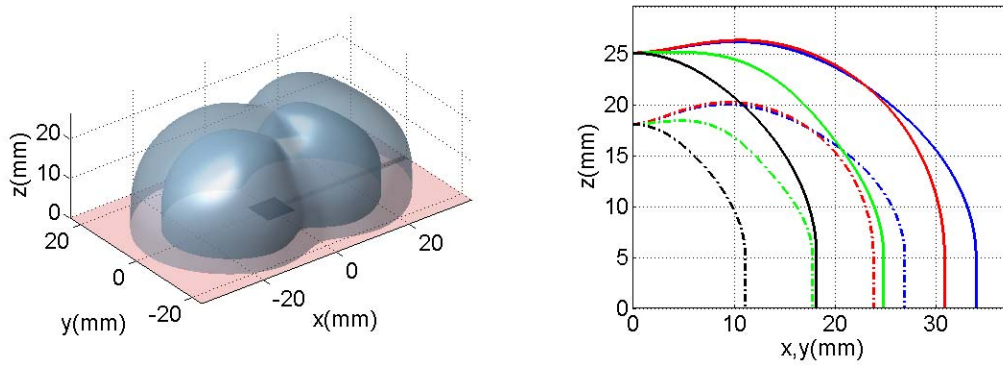
Figure 18: 3-D shape and cut-planes (φ=0°, 30°, 60°, and 90°) of the lens
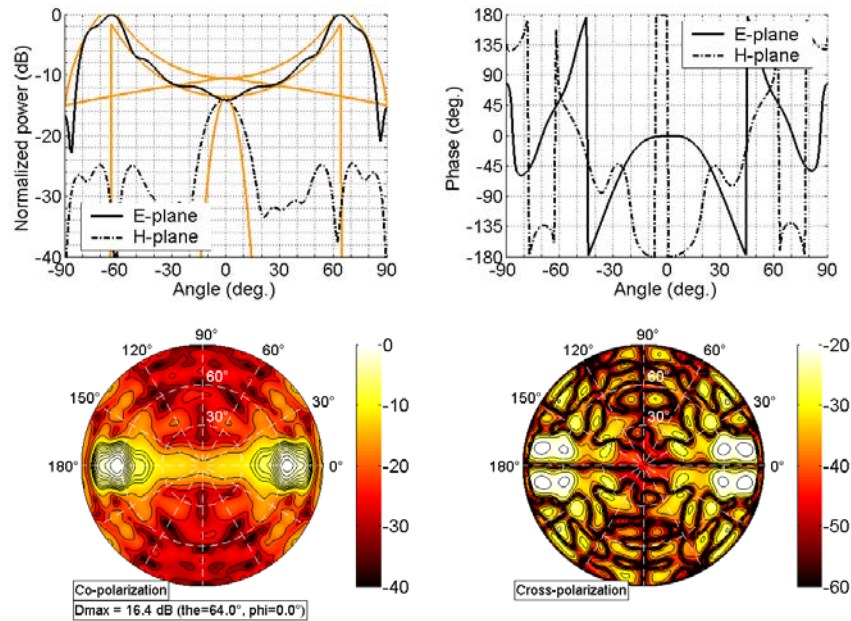
Figure 19: Far-fields of the lens antenna computed at 26 GHz with GO/PO

Comparison with FDTD computations is given in Figure 20.
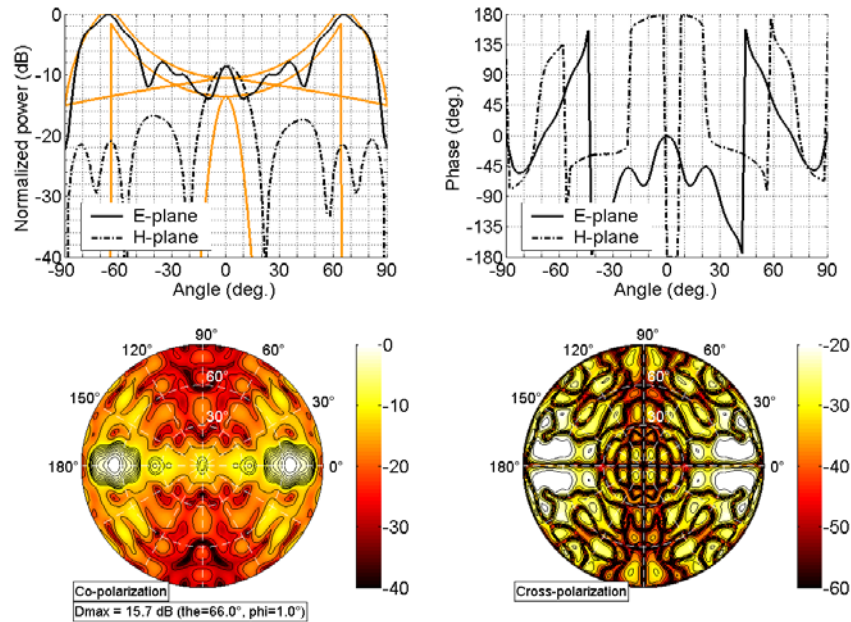
Figure 20: Far-fields of the lens antenna computed at 26 GHz with FDTD

Compared to GO/PO computed far-fields, the FDTD results have ripples in the co-polarization component. It is due to the internal reflections inside the lens body. These reflections could be reduced with anti-reflection coatings at the dielectric interfaces.

The antenna designed for linear polarization (Fig. 18) is under prototyping.

The information contained in this document should be used only for the scope of the contract for which this document is prepared.

4. MEASURED RESULTS

4.1 Axial symmetric lens

Lens fabrication materials are expected to arrive at IST by mid December.

4.2 Generic 3D lens, linear polarization

This lens is under fabrication at IETR.

5 CONCLUSIONS

Results so far show that from the design point of view, the design specifications seem feasible. The axial symmetric dome lens complies with specifications and a sensitivity analysis with respect to permittivity shows a reasonably robust design. Further analysis requires the coming experimental results.

6 REFERENCES

[1]   P. C. Sharma and K. C. Gupta, "Analysis and Optimized Design of Single Feed Circularly Polarized Microstrip Antenna", IEEE Trans. Antennas and Propagation, Vol. 31, N. 6, pp. 949-955, Nov. 1983.

[2]   M. Silveirinha; C. Fernandes; "Shaped Double-Shell Dielectric Lenses for Wireless Millimetrewave Communications", Proc. IEEE AP-S Conference, Salt Lake City, Utah, pp. 1674-1677, 2000.

[3]   http://www.eccosorb.com/catalog/eccostock/HIK500.pdf

[4]   G. Godi, R. Sauleau, D. Thouroude, "A computer-aided design tool for the optimization of arbitrarily-shaped homogeneous single- and double-shell dielectric lenses", Int. Joint Conf. of 4th ESA Workshop on Millimeter-Wave Technology and Applications, 8th Topical Symp. on Millimeter Waves, 7th Millimeter-Wave Int. Symp., Espoo, Finlande, 15-17 Feb. 2006.

2.1.3

Benchmarking of Lens Simulation Softwares

Institution	Authors
BAE Systems	Gareth M. LEWIS, E. E. OKON
IST	Jorge R. COSTA, Carlos A. FERNANDES
IETR	Gaël GODI, Ronan SAULEAU

Document Evolution		
Revision	Date	Reason of change
0	13.12.05	

1. INTRODUCTION AND MOTIVATIONS

The purpose of this document is to benchmark numerical softwares for the modeling of integrated lens antennas at millimeter-wave frequencies. This report is a joint contribution of BAE Systems / Advanced Technology Centre, IT/IST and IETR.

Antenna test cases

The antenna test cases are twofold:

- Single-shell homogeneous dielectric substrate lenses [1,2] with variable extension lengths. These dielectric lenses are fed by a printed patch antenna,
- Double-shell dielectric lenses [3,4].

Modeling tools

For benchmarking purposes, two categories of simulation tools are considered:

- Global numerical softwares:
  - Home-made sofwares:
    - The IMELSI software (Impulse Electromagnetic Simulator) based on the FDTD method and developed by IETR [5,6,7],
    - The BAE SYSTEMS FDTD software,
  - Commercially available tools:
    - Ansoft Designer {Contribution of BAE SYSTEMS},
    - Ansoft HFSS {Contribution of BAE SYSTEMS},
    - WIPLD {Contribution of IST},
- Asymptotic tools based on the hybrid Geometrical Optics / Physical Optics (GO/PO) method:
  - Home-made tools:
    - The ILASH software developed by IT/IST [4],
    - The GO/PO tool developed by IETR [8].

Motivations

IT/IST and IETR have independently developed software tools for the analysis and design of shaped dielectric lenses for millimeter wave applications. Some of these tools use different approaches to tackle the same kind of problems.

As a first step for the desirable data and knowledge interchange on the topic of dielectric lenses, a benchmarking initiative is being carried out between the two institutions. The objective is to compare results obtained from the different tools for some predefined test structures, interpret the differences and eventually improve the simulators.

A couple of reference structures were previously identified for this objective. They span from very simple ideal lens structures up to more elaborate ones. IETR has preformed some preliminary calculations for these structures using IMELSI. The following sections present the corresponding results obtained with the GO/PO based ILASH tool a tentative interpretation of the differences.

The GO/PO results are also compared to "reference data" obtained from global numerical tools.

Outline

The antenna geometry and the main characteristics of the primary feed are presented in Sections 2 and 3, respectively. The accuray of the above-mentionned numerical tools is investigated and discussed in Sections 4 and 5, by considering extended hemispherical substrate lenses. The results obtained with double-shell lenses are given in Section 6. Conclusions are finally drawn in Section 7.

2. ANTENNA GEOMETRY

2.1 Primary feed

The primary feed is an aperture-coupled microstrip patch antenna printed on a RT\5880 Duroïd substrate ($\varepsilon_{r,subs} \approx 2.23$; h=127µm). The ground plane is infinite. The geometry and dimensions of the patch antenna are given in Figure 2.1.

The patch antenna operates in Q-band (around 49.5 GHz).
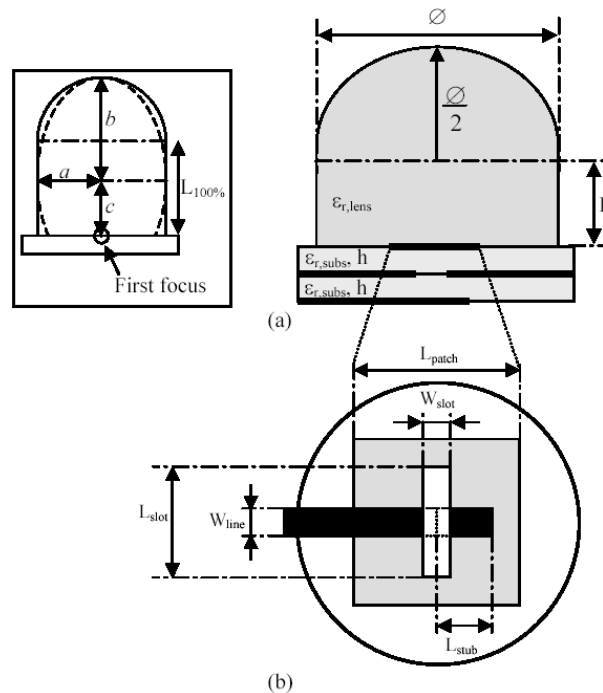
Figure 2.1 – Geometry and dimensions of the aperture-coupled microstrip patch antenna [2]. (W_{line}=0.36mm, L_{stub}=0.51mm, W_{slot}=0.20mm, L_{slot}=0.87mm, L_{patch}=1.38mm)

The predictions for this geometry are presented in Section 3.

2.2 Integrated lens antenna

The fused quartz dielectric lens is illuminated by the patch antenna described in Section 2.1. Three cases are considered depending on the extension length of the lens:

- Hemispherical lens (L=0mm),

- Extended hemispherical lens (L=5.834mm),

- Synthesized elliptical lens (L=11.549mm).

The corresponding numerical results are detailled in Section 4.

3. CHARACTERISTICS OF THE APERTURE COUPLED MICROSTRIP PATCH ANTENNA

The feed was initially modelled radiating into an infinite half-space of dielectric material (fused quartz, ε_r=3.80, tanδ=5×10^{-4}) above an infinite ground plane.

3.1 Reflection coefficient

The performance of this geometry was predicted using Ansoft Designer. The geometry is shown in Figure 3.1. Designer is a 2½ Dimensional code, and so is suited to this geometry.

A comparison of reflected power (return loss) predictions is shown in Figure 3.2. It can be seen that there is a very good agreement between predictions of the resonant frequency from Ansoft Designer, IETR and BAE SYSTEMS FDTD codes.
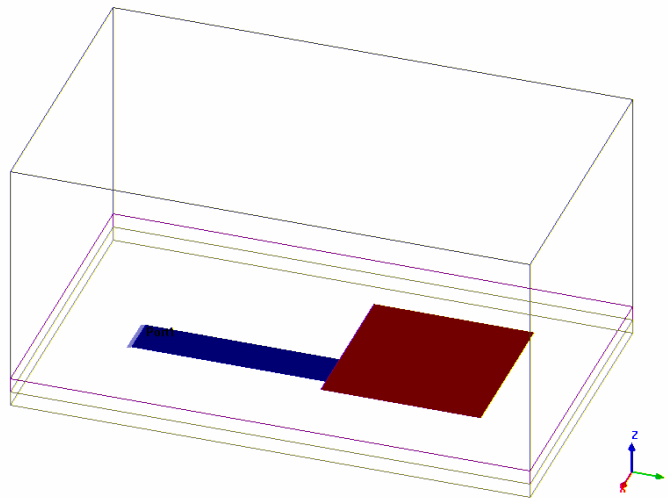
Figure 3.1 – Ansoft Designer model of the Aperture-Coupled Microstrip Patch antenna
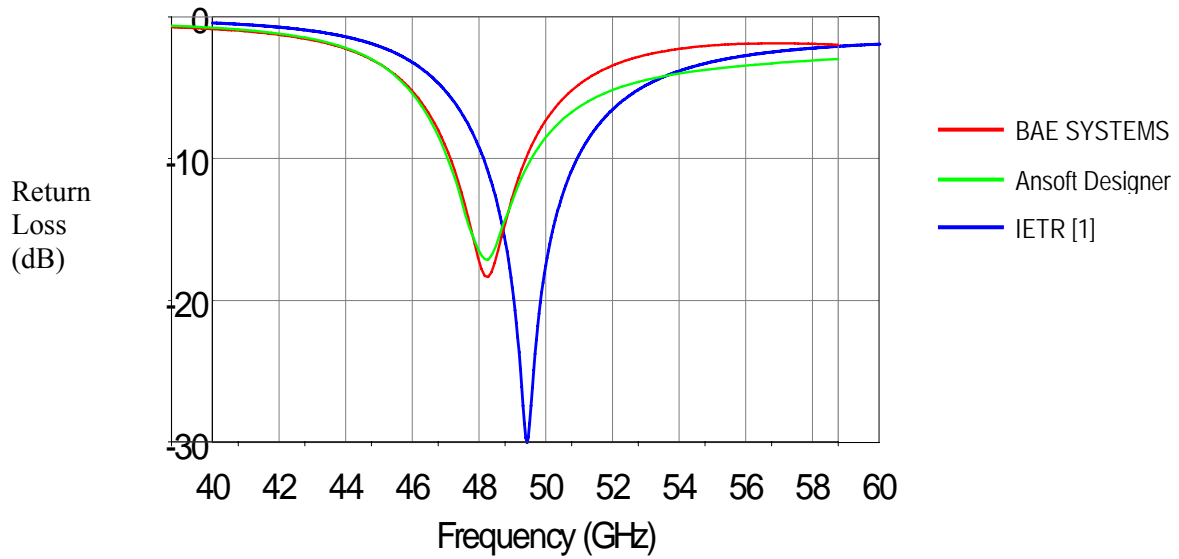
Figure 3.2 – Comparison of the predictions from BAE SYSTEMS FDTD, Ansoft Designer and IETR

3.2 Radiation patterns

The theoretical radiation patterns computed using IMELSI, the IETR FDTD code, are represented in Figure 3.3. No data are available from IST and BAE SYSTEMS.
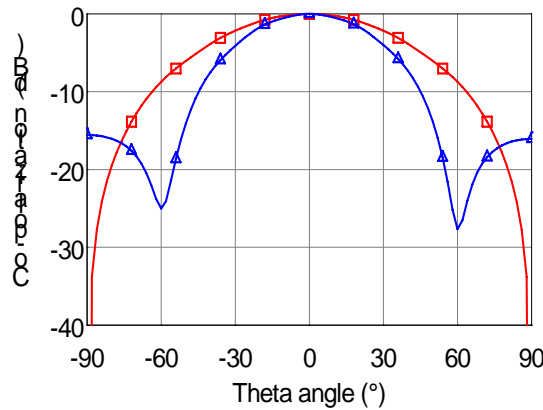
Figure 3.3 – Far-field radiation patterns
at 49.5GHz in E- ( ) and H-planes ( ).

4. FUSED QUARTZ EXTENDED HEMISPHERICAL LENSES

4.1 L=0 mm

BAE SYSTEMS contribution

The HFSS model of this geometry is shown in Figure 4.1. A range of alternative boundary conditions could be applied to the model. The radiation boundary is typically used for antenna

geometries, but requires that the boundary is at least a quarter-wavelength from the antenna geometry. However, in this case the substrate and ground plane meet the boundary. Therefore, the model was also run with PML boundaries to provide a comparison. As can be seen in Figure 4.2, there is little difference between the results calculated using the two boundary conditions.
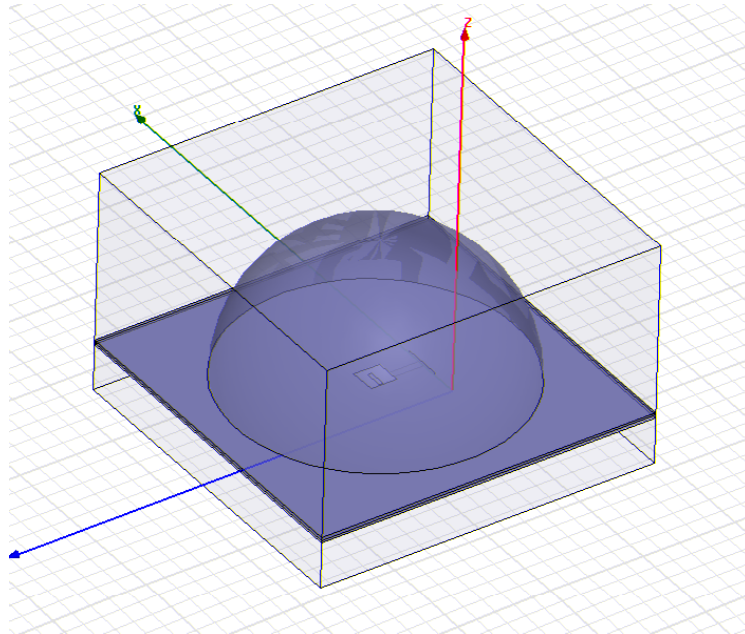
Figure 4.1 – HFSS model of the hemi-spherical lens (L=0mm)

The BAE SYSTEMS FDTD code predicts radiation patterns by using the equivalent currents on the surface of a box enclosing the geometry. However, in these benchmarking cases, the ground plane and the upper half-space of dielectric material are required to be infinitely large. To do this they must meet the PML boundary which cannot then be enclosed. The FDTD code was modified to ignore this criterion, but it must be accepted that some inaccuracy will be imposed on the radiation pattern.

The BAE SYSTEMS FDTD code was run on a Linux PC cluster. This model required approximately 6GB of memory, almost twice as much as HFSS, which is in large part due to the amount of free-space within the problem volume.

The predictions for the input return loss are presented in Figure 4.2. For both the BAE SYSTEMS FDTD and HFSS results there are two nulls over the frequency band, but they differ slightly in frequency and depth. Both cases also seem to differ in detail from the IETR results [2].

The predictions for the E-plane and H-plane radiation patterns are presented in Figures 4.3 and 4.4 respectively. The results for both codes, and in both planes, appear to agree well, with the only significant difference being in the nulls in the E-plane pattern. The E-plane 3dB beamwidth is 50° whilst the H-plane 3dB beamwidth is 68°. One notable difference between these and the IETR ([2] and Figures 5.4 and 4.6) results is the amplitude at 90° in the H-plane: the H-plane amplitude presented here does not roll-off as much as might be expected for an infinite ground plane. This is due to the application of image theory in IMELSI when the ground plane is infinite.

Aperture coupled patch with hemispherical lens (L=0mm)
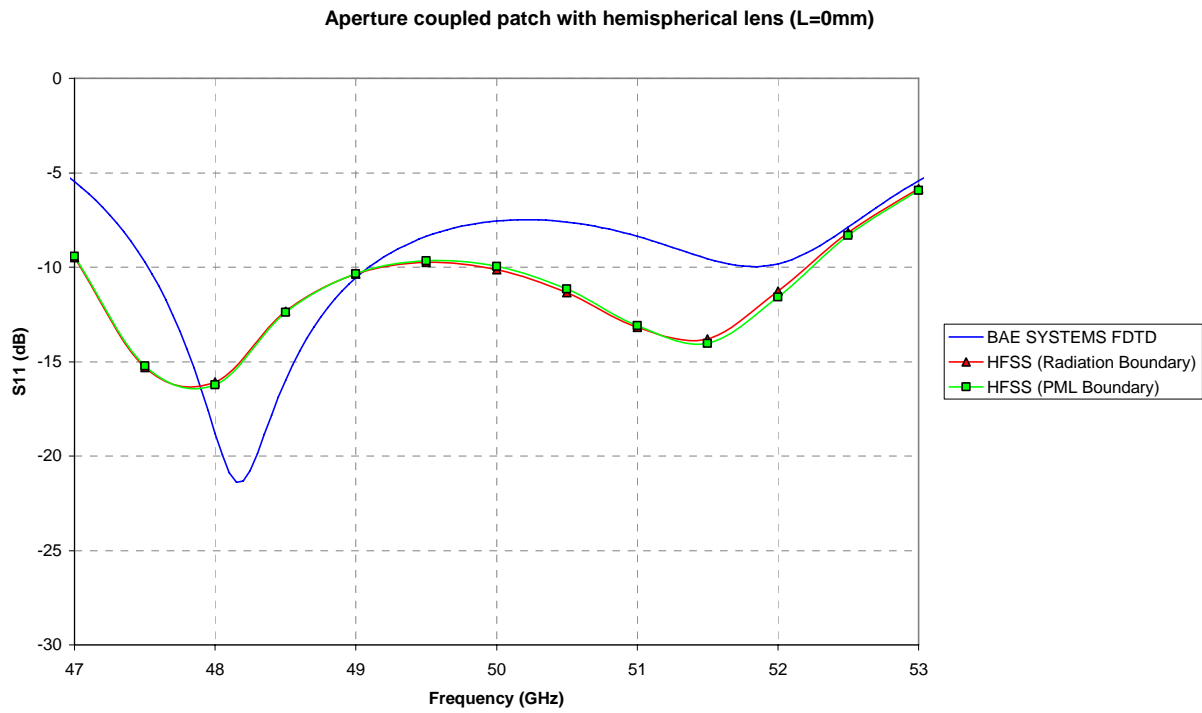
Figure 4.2 – Comparison of BAE SYSTEMS FDTD and HFSS (Radiation and PML Boundaries) predictions of return loss

Aperture Coupled Patch with Hemispherical Lens (Quartz) & Infinite ground plane
E-plane

Figure 4.3 – Comparison of BAE SYSTEMS FDTD and HFSS (Radiation Boundary) predictions of E-plane Radiation Pattern

Figure 4.4 – Comparison of BAE SYSTEMS FDTD and HFSS (Radiation Boundary) predictions of H-plane Radiation Pattern

IETR and IST contributions

The IETR GO/PO computations are done <u>without ground plane</u> placed at the base of the lens (same hypothesis as IST). The following figures compare the IST and IETR results for the same geometries.

Figure 4.5 – Far-field radiation patterns computed by IST for L=0. (a) E-plane; (b) H-plane
(Blue line: FDTD ; Red line: ILASH) – f=49.5 GHz
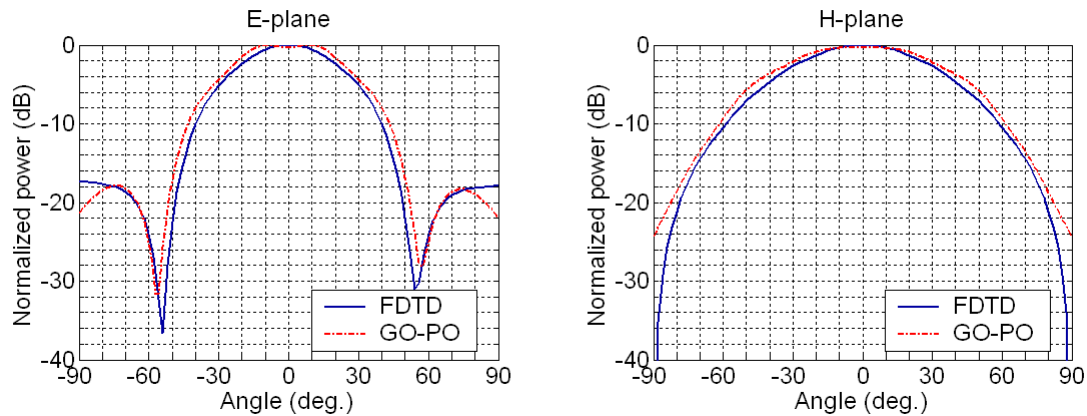
Figure 4.6 – Far-field radiation patterns computed by IETR for L=0.
(a) E-plane; (b) H-plane – f=49.5 GHz

The GO/PO results found by IETR are closed to those obtained by IST:

- A small ripple appear at θ=0° in the E-plane, in contrast to FDTD patterns,

- The levels at θ=90° are almost equal.

4.2 L=5.834 mm

BAE SYSTEMS contribution

The HFSS and BAE SYTEMS FDTD models are both identical to those presented in the previous chapter except for the height of the pedestal (L=5.834mm).

The HFSS model of this geometry is shown in Figure 4.7. The radiation boundary is typically used for antenna geometries, but requires that the boundary is at least a quarter-wavelength from the antenna geometry. Unfortunately, due to the memory requirements for this geometry the boundary had to be placed only one-tenth of a wavelength from the geometry.

For the BAE SYSTEMS FDTD code, as before, the substrate and ground plane were run into the PML at the boundary in order to simulate an infinite ground plane. Therefore, the error checking for the equivalent surface was again disabled. The BAE SYSTEMS FDTD code was run on a Linux PC cluster. This model required approximately 8GB of memory.

The predictions for the input return loss are presented in Figure 4.6. The BAE SYSTEMS FDTD and HFSS results' most significant difference is at 49GHz. The FDTD results most closely match the IETR [1] results.

The predictions for the E-plane and H-plane radiation patterns are presented in Figures 4.8 and 4.9 respectively. The results for both codes, and in both planes, appear to agree well, with the only significant difference at around 45° in the E-plane pattern. The E-plane 3dB beamwidth is 22° whilst the H-plane 3dB beamwidth is 23°.
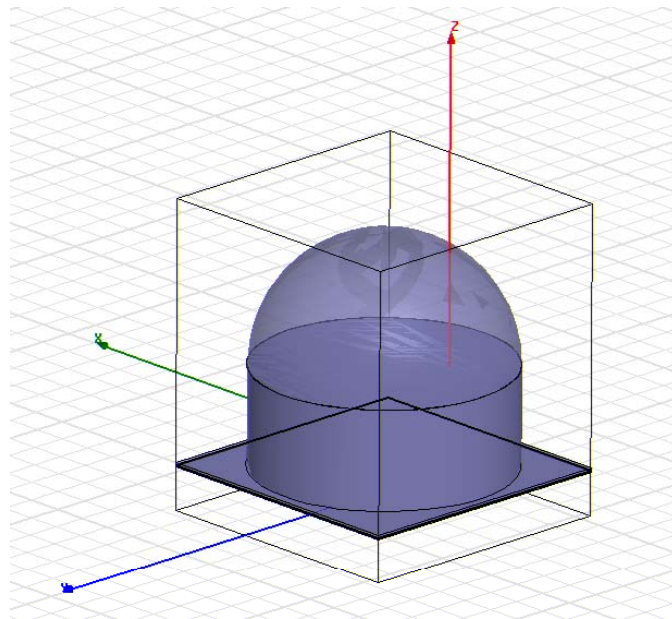
Figure 4.7 – HFSS model of the extended hemi-spherical lens (L=5.834mm)

Aperture coupled patch with extended hemispherical lens (L=5.834mm)
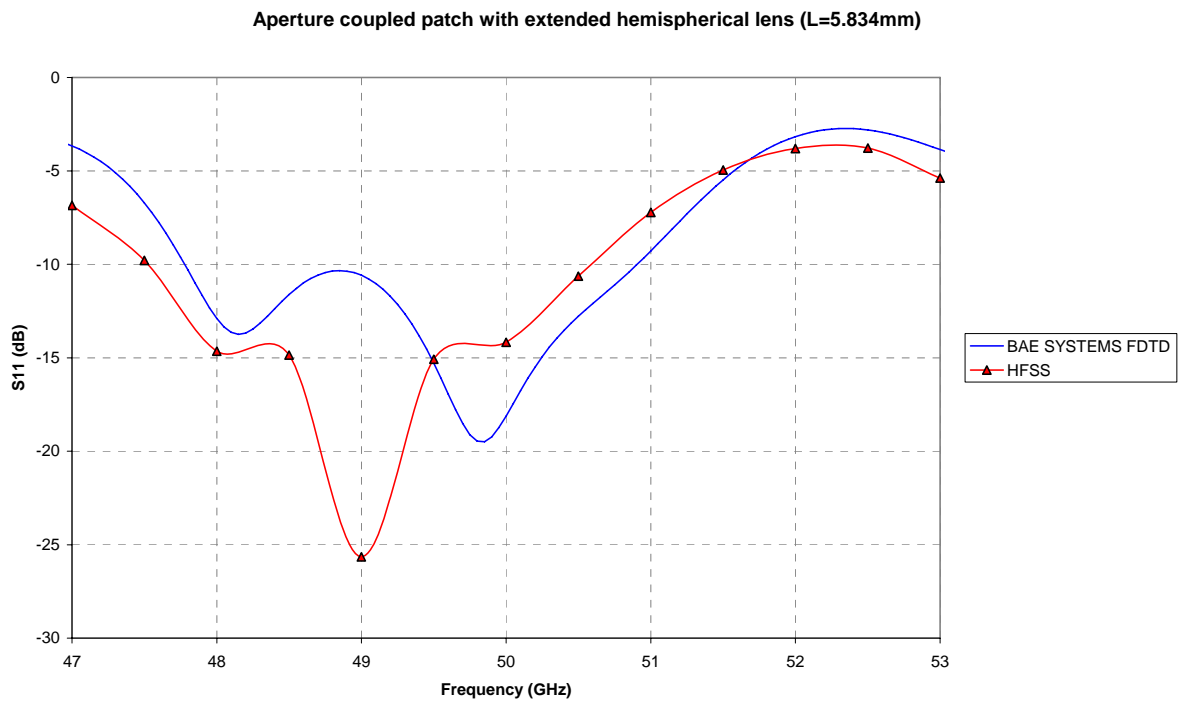
Figure 4.8 – Comparison of BAE SYSTEMS FDTD and HFSS (Radiation Boundary) predictions of return loss

Aperture Coupled Patch with Extended (L=5.834mm) Hemispherical Lens (Quartz) & Infinite ground plane
E-plane
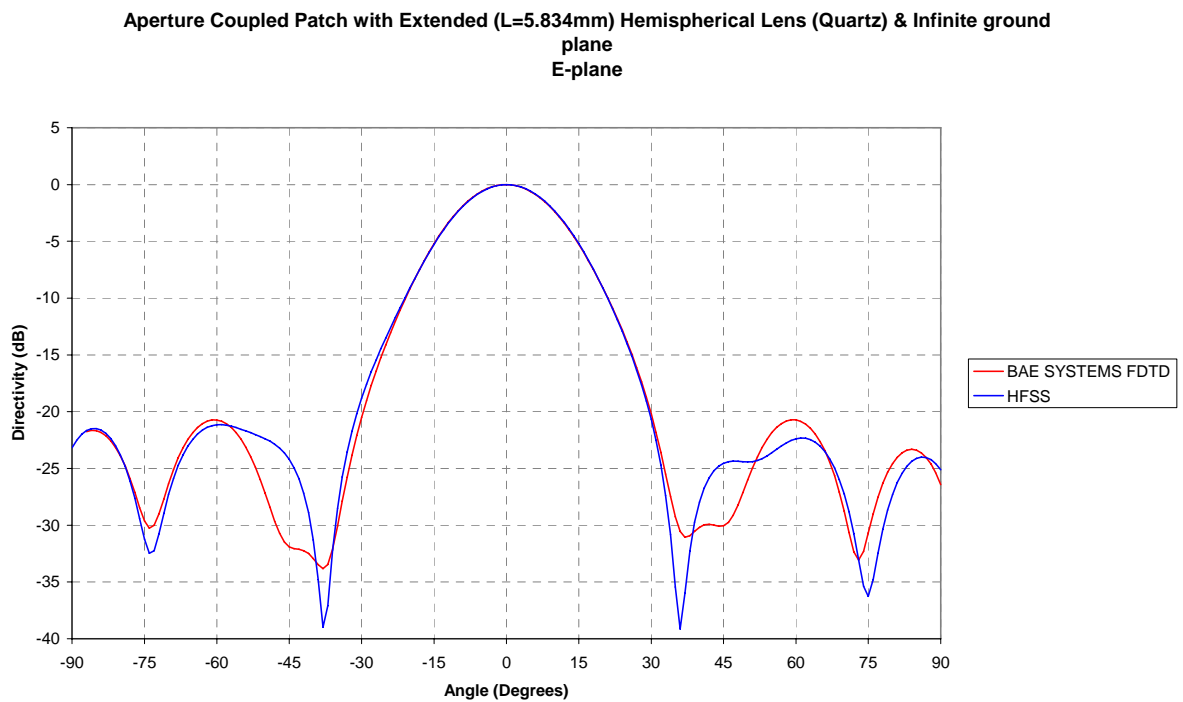
Figure 4.9 – Comparison of BAE SYSTEMS FDTD and HFSS (Radiation Boundary) predictions of E-plane radiation pattern

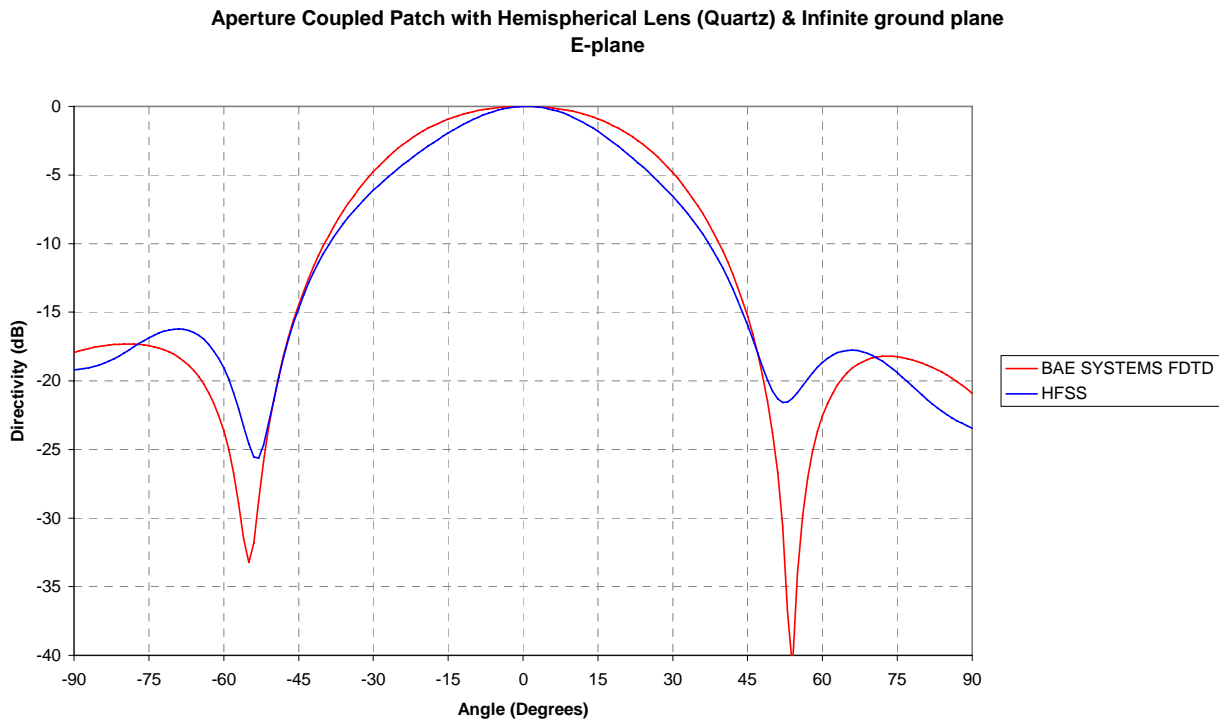**Aperture Coupled Patch with Extended (L=5.834mm) Hemispherical Lens (Quartz) & Infinite ground plane**
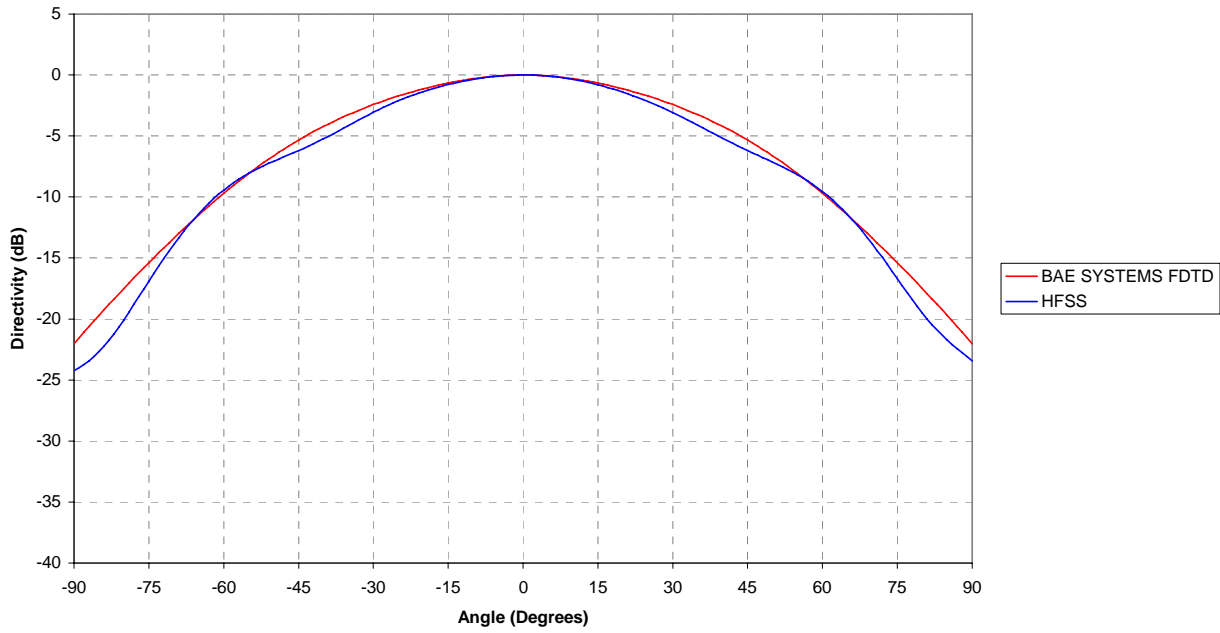**H-plane**
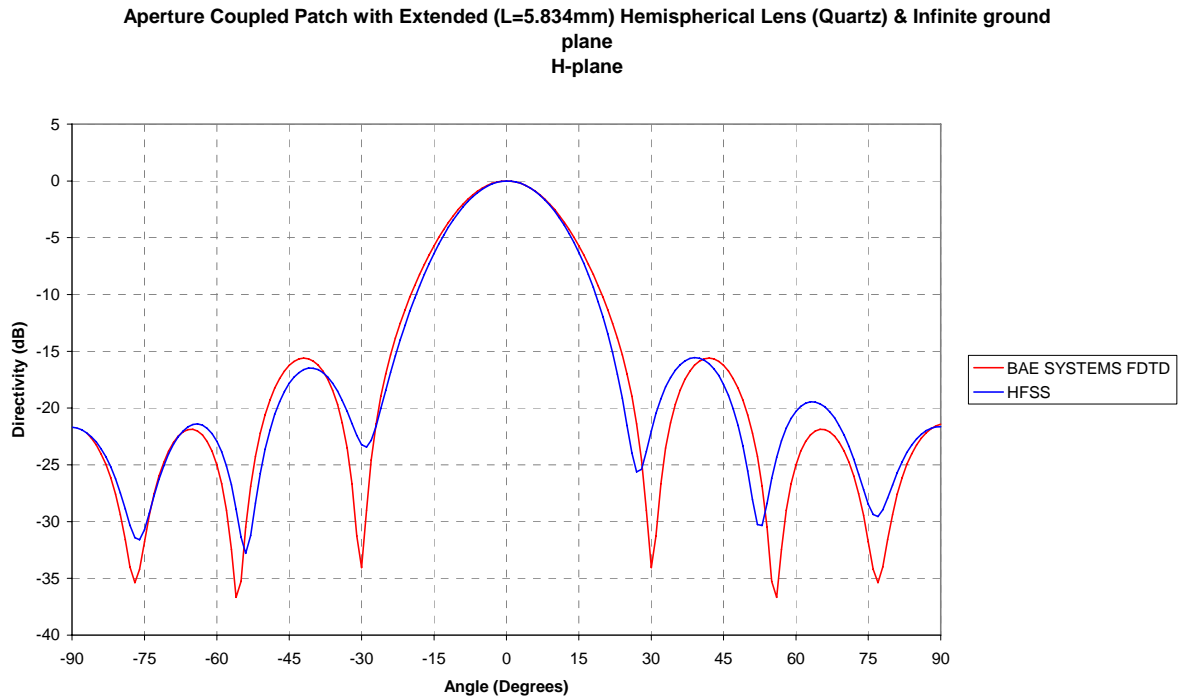
Figure 4.10 – Comparison of BAE SYSTEMS FDTD and HFSS (Radiation Boundary) predictions of H-plane Radiation Pattern

IETR and IST contributions
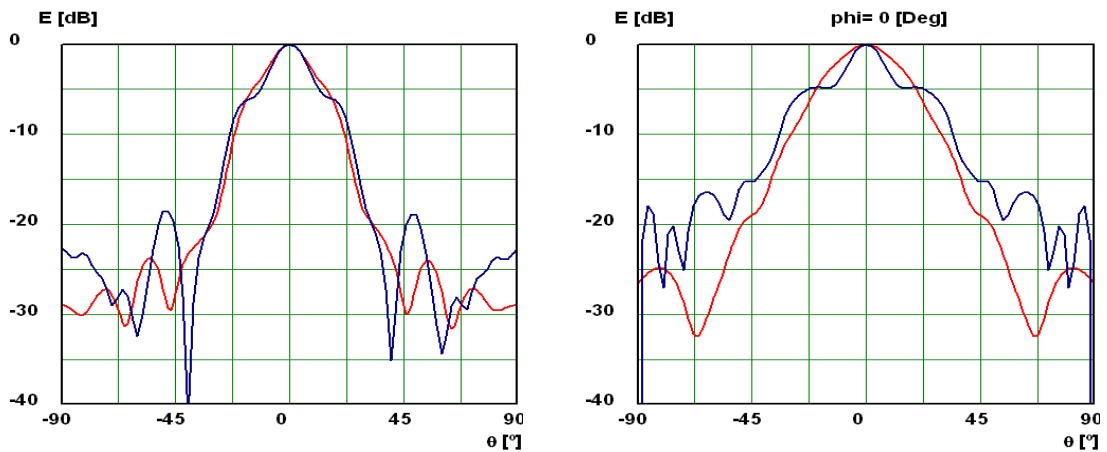
Figure 4.11 – Far-field radiation patterns computed by IST for L=6.474mm.
(a) E-plane; (b) H-plane (Blue line: FDTD ; Red line: ILASH) – f=49.5 GHz
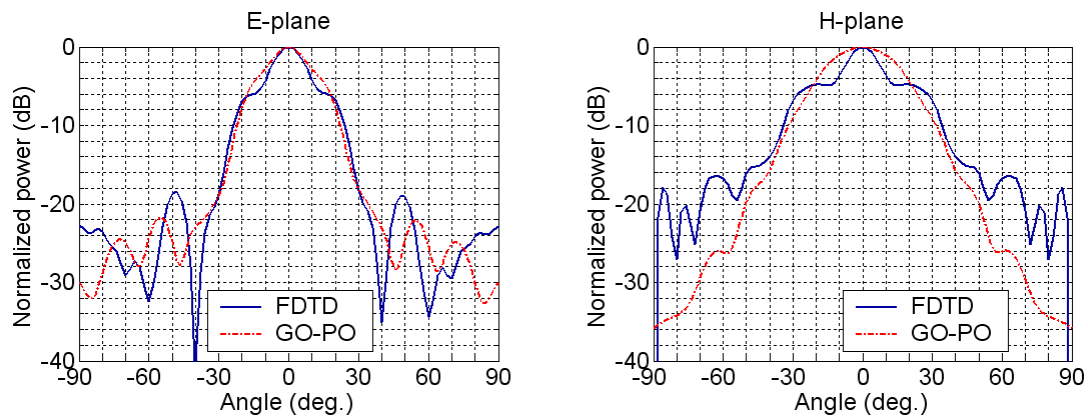
Figure 4.12 – Far-field radiation patterns computed by IETR for L=6.474mm.
(a) E-plane; (b) H-plane – f=49.5 GHz

The results obtained by IETR and IST are very similar.

4.3 L=11.459 mm

BAE SYSTEMS contribution

It was not possible to model this configuration using HFSS, since the total memory requirement exceeded that available on the computer. Due to limitations in the operating system (Windows XP) and HFSS, the maximum addressable memory is 4GB. The previous case (L=5.834mm) used 3.2GB memory and the L=11.459mm case would obviously need significantly more. Attempts were made to reduce the amount of memory required, by moving the boundaries closer to the geometry (to the extent that the boundaries touched the geometry – see Figure 4.9 below). However, this was not sufficient to allow the problem to be solved.

We are currently migrating to version 10 which may offer improved meshing and memory handling features, but it is not certain that this would be sufficient to allow the simulation to proceed.

The information contained in this document should be used only for the scope of the contract for which this document is prepared.
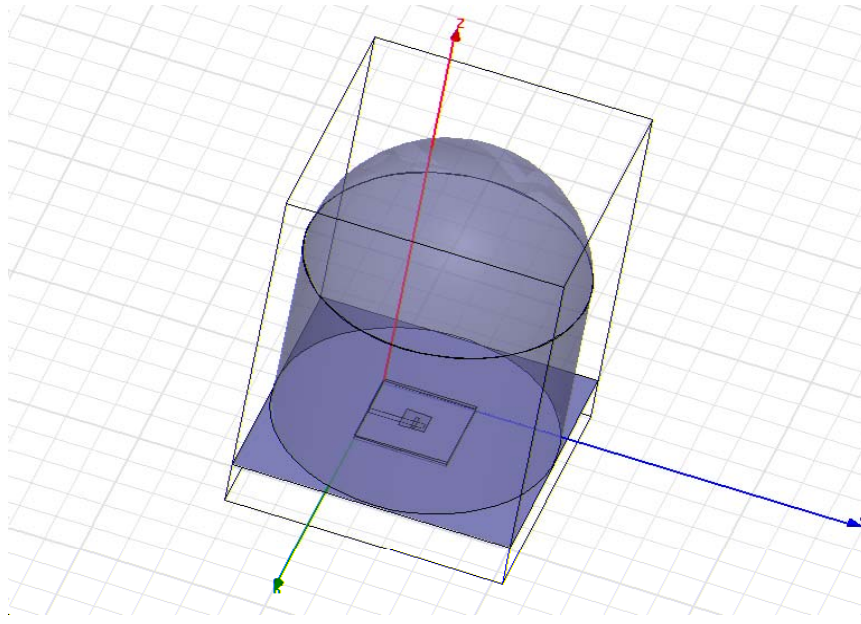
Figure 4.13 – HFSS model of the extended hemi-spherical lens (L=11.459mm)

The memory requirements for modelling this geometry with the BAE SYSTEMS FDTD code are also very significant. It is planned to attempt to simulate this using the PC cluster when a sufficiently long modelling time becomes available. However, this has not been possible within the timescales of the current ACE programme. Results may become available in early 2006.

IETR and IST contributions
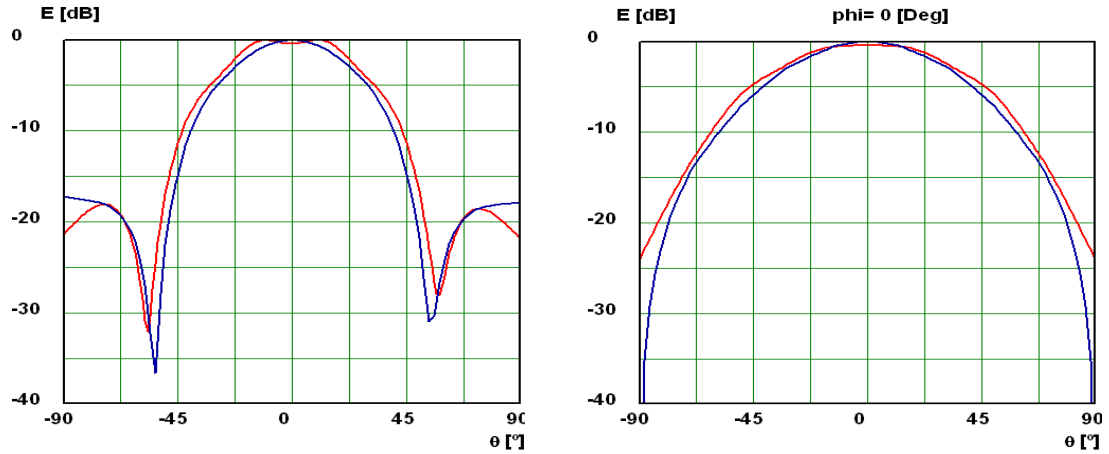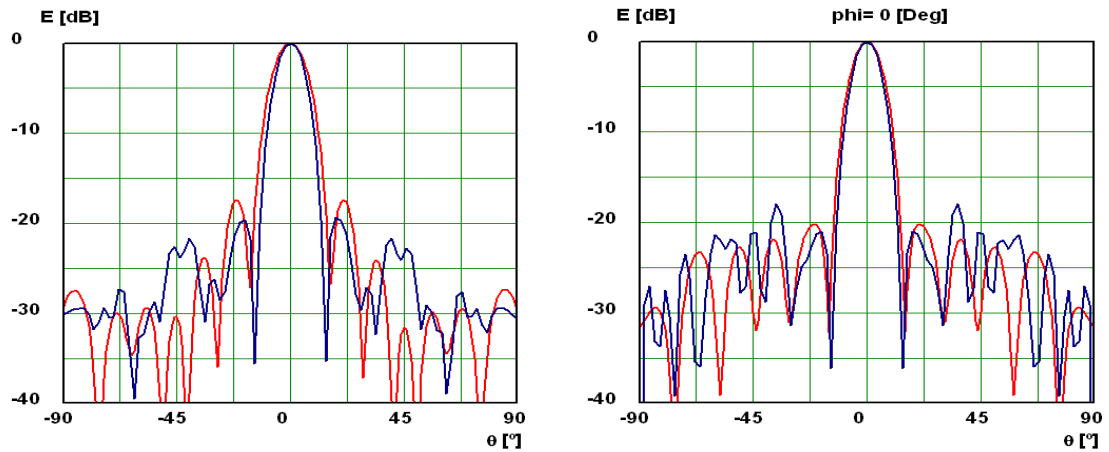

Figure 4.14 – Far-field radiation patterns computed by IST for L=12.189mm.
(a) E-plane; (b) H-plane (Blue line: FDTD ; Red line: ILASH) – f=49.5 GHz

The information contained in this document should be used only for the scope of the contract for which this document is prepared.

ACE – Antenna Centre of Excellence   Contract FP6-IST 508009

Document Title   *Date*
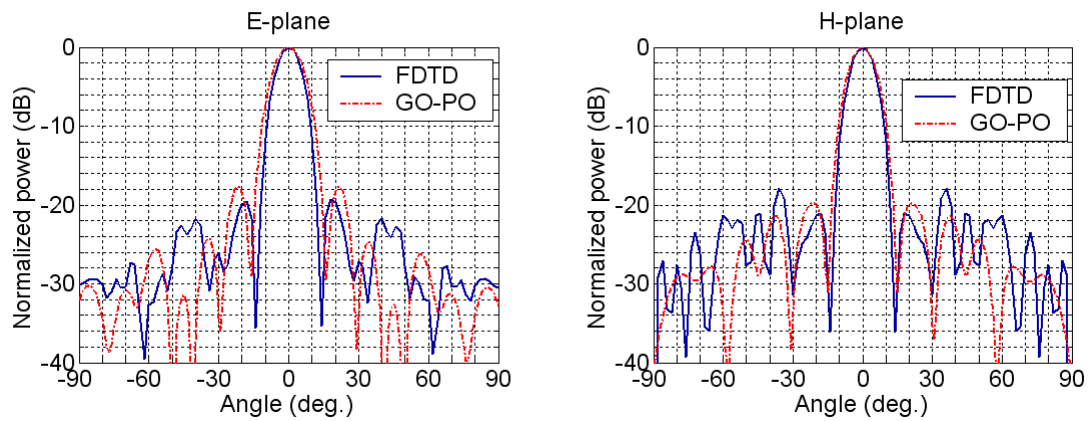
Figure 4.15 – Far-field radiation patterns computed by IETR for L=12.189mm.
(a) E-plane; (b) H-plane – f=49.5 GHz

The results obtained by IETR and IST are very similar.

5. ANALYSIS OF BENCHMARK GEOMETRIES, WITH FDTD AND GO-PO IETR TOOL

The computations are done <u>with a ground plane</u> placed at the base of the lens (coherent with FDTD simulations). Original extension lengths and corrected extension lengths (+0.64mm) are computed with GO-PO and compared to FDTD.
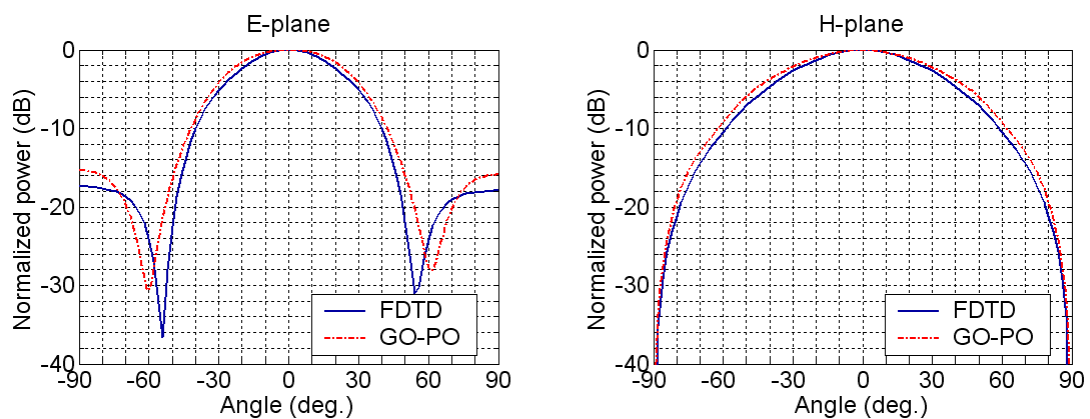
Figure 4.16 – L=0mm FDTD & L=0mm GO-PO
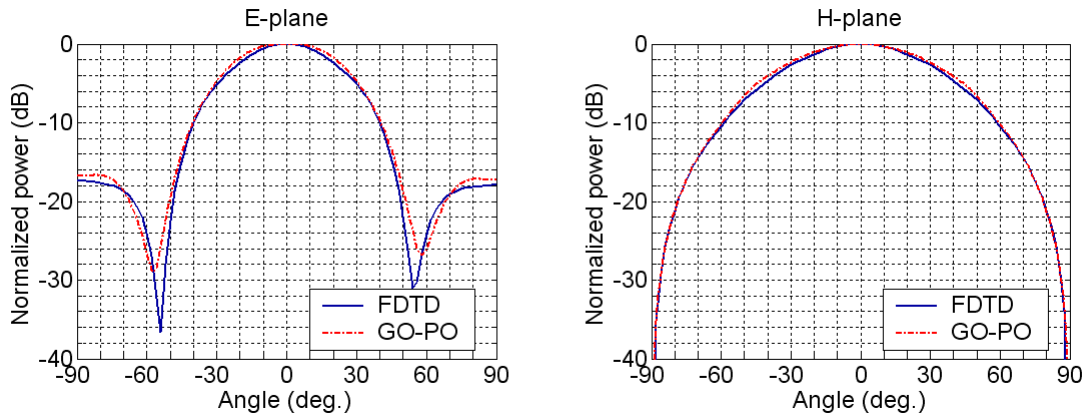
Figure 4.17 – L=0mm FDTD & L=0.64mm GO-PO
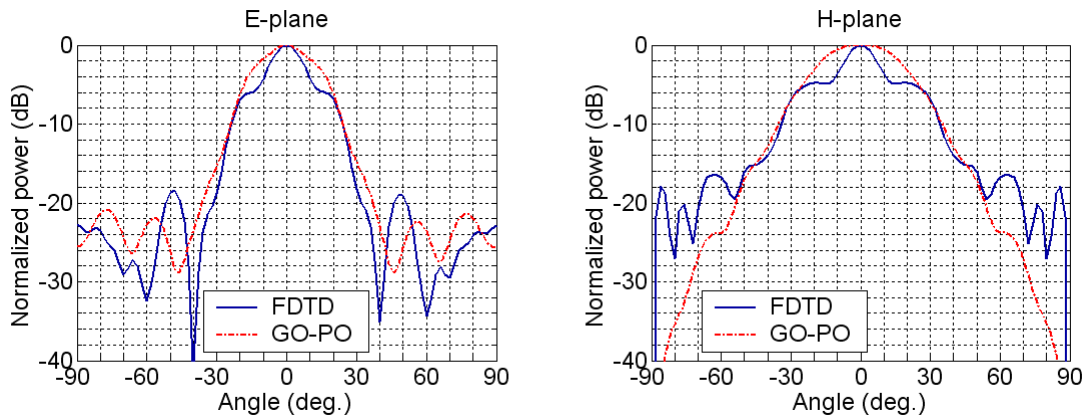
Figure 4.18 – L=5.834mm FDTD & L=5.834mm GO-PO
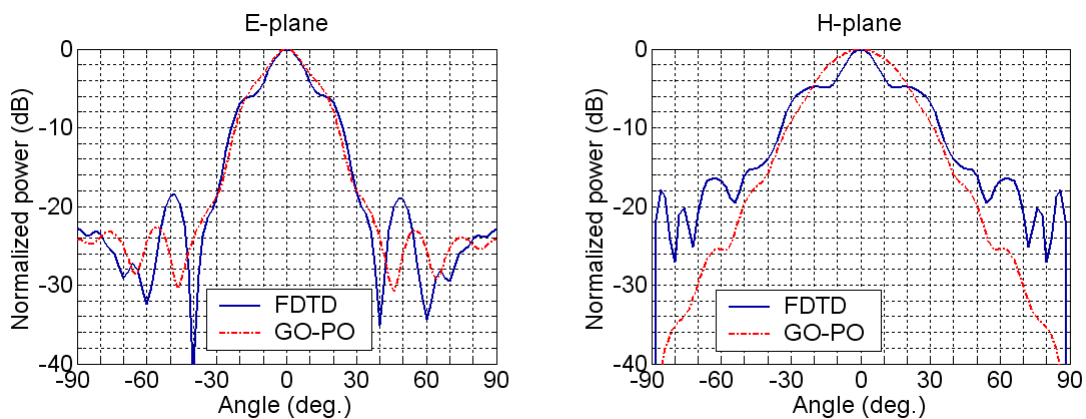
Figure 4.19 – L=5.834mm FDTD & L=6.474mm GO-PO

In the case of GO-PO simulations, the ground plane (at z=0) brings minor changes in the far-field patterns compared to the geometries without ground plane. GO-PO results differ from FDTD, especially when L=5.834mm.

In order to find the reason(s) of the differences in the far-field patterns, FDTD simulations are done, without taking into account the multiple reflections inside the lens (the method is explained in Ref. [2]).
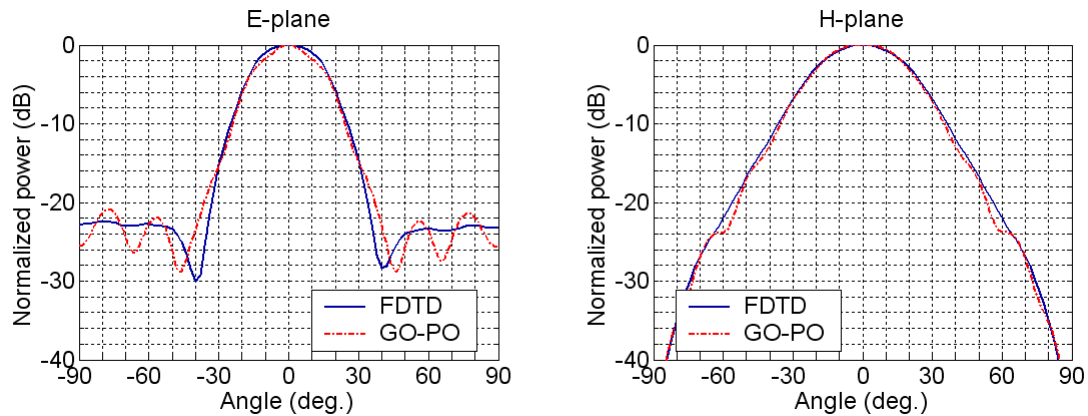
Figure 4.20 – L=5.834mm FDTD <u>with only first refraction</u> & L=5.834mm GO-PO
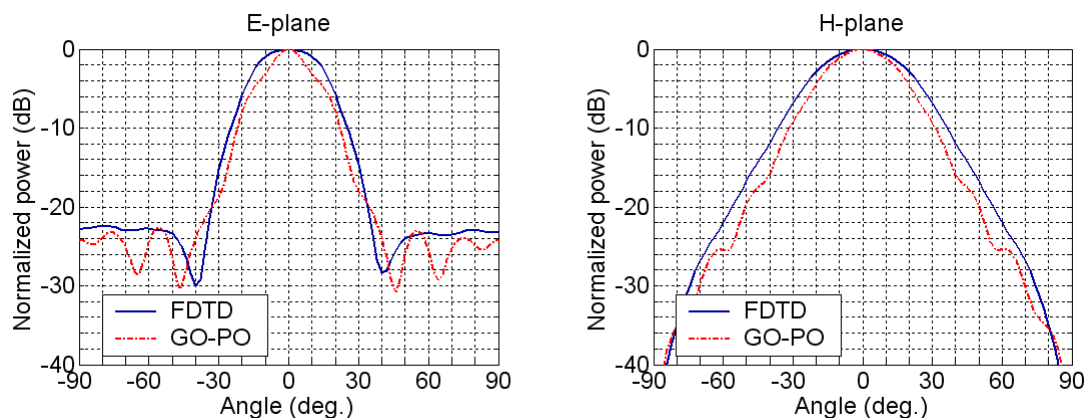
Figure 4.21 – L=5.834mm FDTD <u>with only first refraction</u> & L=6.474mm GO-PO

Amplitude patterns are similar for the two approaches (FDTD and GO-PO), in the case of reflection-less simulations (fig. 11). It means that **internal reflections inside the lens are mainly responsible for the differences between the FDTD and GO-PO** computations. Note that the ground plane used for IETR computation lowers the rear-side radiation but probably increase the influence of these reflections, compared to geometries without ground plane.

That implies also that the phase centre position may not be the reason of the differences between FDTD and GO-PO results (Figure 4.21).
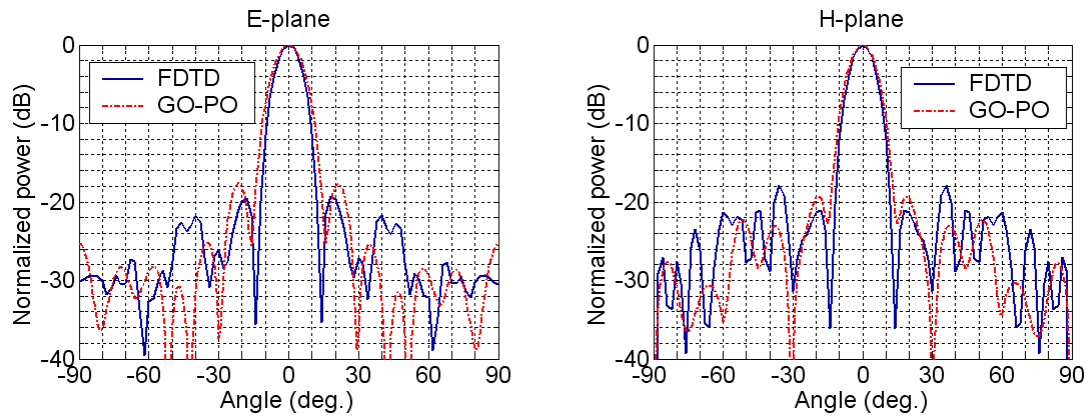
Figure 4.22 – L=11.549mm FDTD & L=11.549mm GO-PO
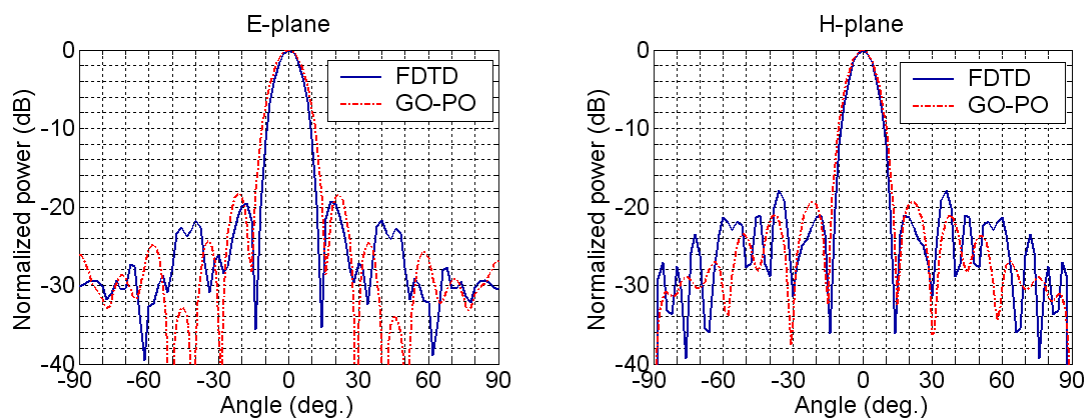
Figure 4.22 – L=11.549mm FDTD & L=12.189mm GO-PO

6. DOUBLE-SHELL INTEGRATED LENS ANTENNAS

In Europe, double-shell shaped integrated lens antennas [3,4,8] are mainly studied by two laboratories (IT/IST and IETR). In contrast to single-shell lenses, these structures allow to improve significantly the antenna characteristics (broader bandwidth, size reduction, etc.).

Based on recent results obtained by IT/IST [4], both laboratories have compared the accuracy of their design tools. The antenna test case is represented in Figure 4.23.
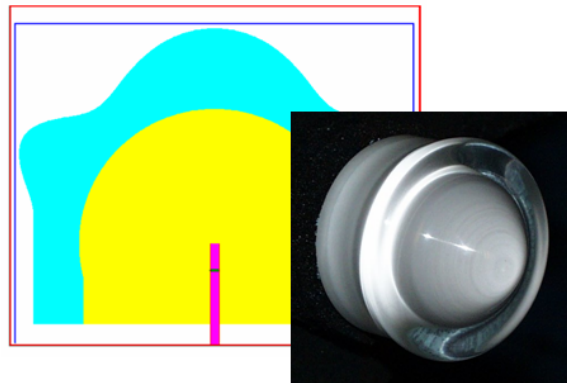
Figure 4.23 – The double-shell lens antenna used as a tets case

Comparison between theoretical and experimental results are given in Figure 4.24 at 62.5GHz. A satisfactory agreement is obtained between measurements and simulations.
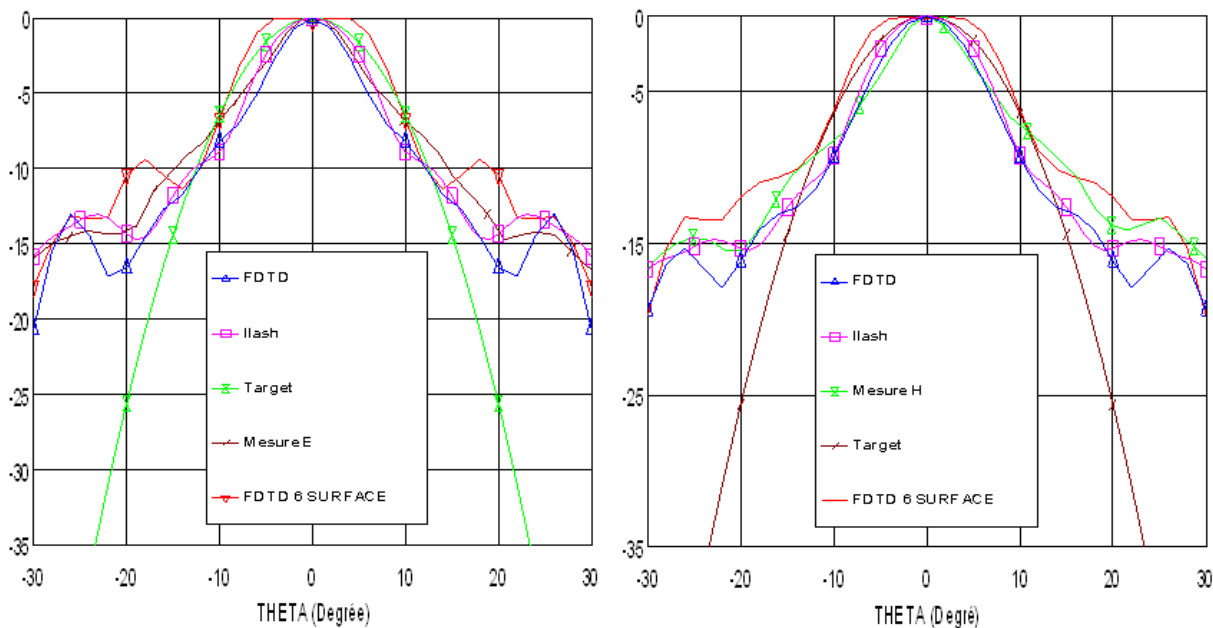
Figure 4.24 – The double-shell lens antenna used as a tets case

7. CONCLUSIONS AND FUTURE WORK

This report summarizes the main results obtained by BAE SYSTEMS, IT/IST and IETR about the modelling of millimeter-wave integrated lens antennas using commercial and home-made numerical tools.

The accuracy of asymptotic simulation tools has been demonstrated by comparison with numerical results obtained with global modeling softwares. For that purpose, two categories of lenses have been studied:
-   Single-shell extended hemispherical dielectric lenses,

- Double-shell shapes dielectric lenses.

Quasi-optical antennas, and in particular integrated lens antennas, are key technologies for many millimeter- and sub-millimeter-wave current and future applications. This activity should be promoted within the framework of ACE-2, given the unique expertise of IT/IST and IETR in this area. Several joint projects could be defined in strong cooperation with industrial partners (Alcatel Alenia Space, BAS SYSTEMS, etc.) and academic institutions (e.g. VTT laboratory, UPM).

REFERENCES

[1]   D. F. Filipovic, S. S. Gearhart, G. M. Rebeiz, "Double-slot antennas on extended hemispherical and elliptical silicon dielectric lenses", IEEE Trans. Microwave Theory Tech., vol. 41, n°-10, pp. 1738-1749, Oct. 1993

[2]   G. Godi, R. Sauleau, D. Thouroude, "Performance of electrically small substrate lens antennas for millimetre-wave communications", IEEE Trans. Antennas Propagat., vol. 53, n°4, pp. 1278-1286, April 2005

[3]   M. Silveirinha, C. A. Fernandes, "Shaped double-shell dielectric Lenses for wireless millimeter wave communications", Proc. 2000 IEEE AP-S International Symp., Salt Lake City, Utah, pp. 1674-1677, July 2000

[4]   J. R. Costa, M. Silveirinha, C. A. Fernandes, "Design and analysis of double-shell axial-symmetric integrated lens antennas for space applications", 28th ESA Antenna Workshop on Space Antenna Systems and Technologies, Vol. 2, pp. 865-872, May 2005

[5]   R. Sauleau, Ch. Guiffaut, Ph. Coquet, K. Mahdjoubi, J.-P. Daniel, "FDTD modeling on high performance Vector/Parallel computers. Application to the analysis of millimeter wave printed antennas and focusing devices", 8th Int. Conf. on Advances in Communications and Control - Telecommunication / Signal processing, COMCON8, Greece, pp. 329-347, 25-29 June, 2001

[6]   Ch. Guiffaut, K. Mahdjoubi, "A parallel FDTD algorithm using the MPI library", IEEE Antennas and Propagation Mag., Vol. 43, n°2, pp. 94-103, April 2001

[7]   H. Hoteit, R. Sauleau, B. Philippe, Ph. Coquet, J.-P. Daniel, "Vector and parallel implementations for the FDTD analysis of millimeter wave planar antennas", Int. Journ. of High Speed Computing, vol. 10, n°2, pp. 209-234, Dec. 1999

[8]   G. Godi, R. Sauleau, D. Thouroude, "A computer-aided design tool for the optimization of arbitrarily-shaped homogeneous single- and double-shell dielectric lenses", Int. Joint Conf. of 4th ESA Workshop on Millimeter-Wave Technology and Applications, 8th Topical Symp. on Millimeter Waves, 7th Millimeter-Wave Int. Symp., Espoo, Finlande, 15-17 Fév. 2006

2.2 Metamaterial-based antennas

2.2.1 Introduction and background

Metamaterials are dielectric or metallic periodic structures that can be described, in suitable frequency ranges, as homogeneous media with properties not exhibited by ordinary, natural materials (see, e.g., [1], [2] and references therein). With reference to bulk media (*volume metamaterials*), these properties include negative values of the permittivity and/or of the permeability, or positive but extremely small or large values of the same parameters. After the seminal theoretical work of Veselago at the end of the sixties [3], the study of metamaterials has received much attention in recent years thanks to the realization of artificial magnetic conductors by means of resonant metal inclusions in a host dielectric media by Smith *et al.* [4] (and subsequently by other groups) and of non-resonant transmission-line-like planar structures by Eleftheriades *et al.* [5] and Itoh *et al.* [6]

The area of metamaterials has widened to include also planar structures (*surface metamaterials*) which can be described in certain frequency ranges as homogeneous surfaces with some peculiar property, e.g., that of exhibiting a specific surface impedance or transition impedance. Artificial magnetic conductors, artificially-hard and soft surfaces, and electronically-controllable surface impedances are examples of the kinds of surfaces considered so far in the literature [7]. These structures, in addition to having theoretical interest in themselves and to offer challenges for their actual implementation, are particularly interesting for the realization of planar radiators with enhanced impedance and radiation features.

In this context, the design of millimeter and sub-millimeter wave antennas may potentially benefit from the use of metamaterial structures, either volume or surface. The problems to be addressed in this frequency range are related to the reduction of material losses in general, and in particular to the reduction of surface-wave excitation and to the directivity enhancement with reference to planar realizations (e.g., metal-patch antennas).

[1] R. W. Ziolkowski and N. Engheta (Eds.), "Special Issue on Metamaterials," *IEEE Trans. Antennas Propagat.*, vol. 51, Oct. 2003.

[2] T. Itoh and A. A. Oliner (Eds.), "Special Issue on Metamaterials," *IEEE Trans. Microwave Theory Tech.*, vol. 53, Apr. 2005.

[3] V. G. Veselago, "The electrodynamics of substances with simultaneously negative values of ε and μ," *Sov. Phys. Usp.*, vol. 10, no. 4, pp. 509--514, Jan.-Feb. 2001. (Original Russian version in *Usp. Fiz. Nauk.*, vol. 92, pp. 517-526, 1967).

[4] D. R. Smith, W. J. Padilla, D. C. Vier, S. C. Nemat-Nasser, and S. Schultz, "Composite medium with simultaneously negative permeability and permittivity," *Phys. Rev. Lett.*, vol. 84, pp. 4184-4187, May 2000.

[5] G. V. Eleftheriades, A. K. Iyer, and P. C. Kremer, "Planar negative refractive index media using periodically L-C loaded transmission lines," *IEEE Trans. Microwave Theory Tech.*, vol. 50, pp. 2702-2712, Dec. 2002.

[6] C. Caloz and T. Itoh, "Application of the transmission line theory of left-handed (LH) materials to the realization of a microstrip "LH line"," *2002 IEEE Antennas and Propagation Society International Symposium Digest*, vol. 2, pp. 412-415, 16-21 June 2002.

[7] P.-S. Kildal, A. A. Kishk, and S. Maci (Eds.), "Special Issue on Artificial Magnetic Conductors, Soft/Hard Surfaces, and other Complex Surfaces," *IEEE Trans. Antennas Propagat.*, vol. 53, Jan. 2005.

2.2.2 Objectives

The research activity carried out in the area of metamaterials by our group has focused on different themes, all oriented to the design of *planar antennas* with enhanced performances. The studies have not been restricted to the millimeter-wave range, since the objective was to gain physical insight into the radiation mechanisms and to develop basic simulation tools.

With reference to volume metamaterials, low-permittivity substrates have been considered, which allow, under suitable conditions, to greatly enhance the broadside directivity of a simple source. The goal was to characterize the nature of radiation from such structures, to simulate both homogeneous and periodic realizations based on a wire medium, and finally to consider more advanced homogenized models which take into account anisotropy and spatial dispersion. This research was made in collaboration with Prof. David R. Jackson of the University of Houston and with Dr. Filippo Capolino of the University of Siena. In the framework of this collaboration, Dr. Capolino, who is a workpackage coordinator of the *Metamorphose* European Network of Excellence, invited our research group to become '*Friends of Metamorphose*', and invited two of us (P. Burghignoli and G. Lovat) to deliver lessons on this research topic during the "II Week of the Distributed European Doctoral School on Metamaterials".

A second topic concerning volume metamaterials has been the employment of epsilon-negative (ENG) media in non-radiative dielectric waveguide (NRD) configurations. As is well known, NRD technology is particularly suitable for operation in the higher microwave and millimeter-wave ranges, thanks to its reduced material and radiation losses. The goal was in this case to explore the possibility of having unimodal propagation of the desired low-loss LSM_{01} mode by means of an ENG strip.

With reference to surface metamaterials, one goal was to start a collaborative work with the University of Birmingham on metal periodic surfaces aimed at producing multi-band operation for a simple patch antenna. The initial project has involved frequencies in the GHz range, and full-wave simulations with a commercial code based on the finite-element method ($HFSS^{TM}$ by Ansoft Corp.) had been planned.

Finally, the development of a full-wave code based on the method of moments in the space domain for the rigorous analysis of metal periodic screens has been planned by our group, with the aim of characterizing dispersion properties of surface and leaky waves supported by grounded dielectric slabs covered with such screens. This research was made in collaboration with Prof. Arthur A. Oliner of the Polytechnic University of New York, with Prof. David R. Jackson of the University of Houston, and with Dr. Carlo Di Nallo of Motorola Corp.

2.2.3 Technical part

2.2.3.1   *Volume metamaterials*

2.2.3.1.1   *Low-permittivity grounded slabs*

A low-permittivity grounded metamaterial slab as in Fig. 1(a) has been considered, with a plasma-like dispersive permittivity

$$\varepsilon_r = 1 - \frac{f_p^2}{f^2} \qquad\qquad (1)$$

(where f_p is the plasma frequency) excited by an electric line source. The power density radiated at

(a) (b)
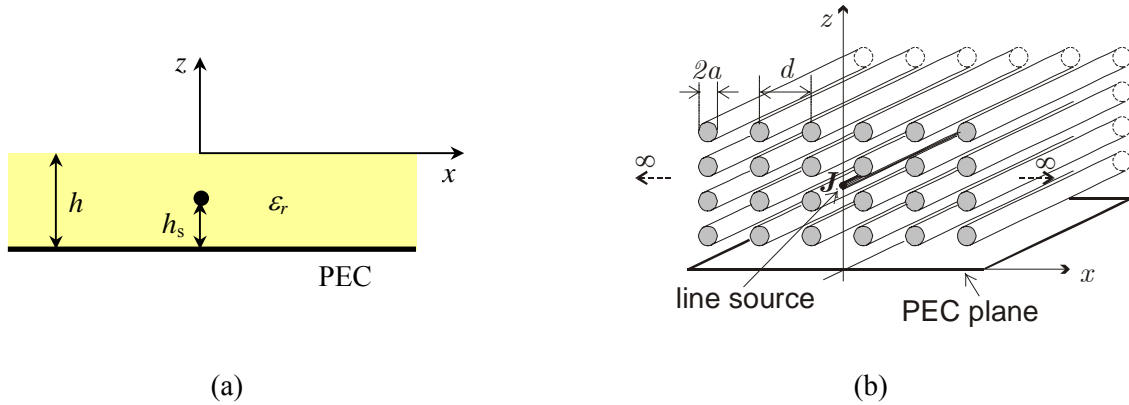
Fig. 1 – (a) Grounded metamaterial slab with a plasma-like relative permittivity. (b) Grounded wire-medium slab, which can be homogenized as in (a) at sufficiently low frequencies.

broadside is maximized when the slab thickness is equal to half a wavelength inside the slab. Under this condition, an asymptotic analysis of the relevant TE dispersion equation has allowed us to establish the presence of a dominant leaky mode with small and equal values of the phase and attenuation constants, given by

$$\hat{\beta} = \hat{\alpha} \cong \sqrt{\frac{c^3}{8\pi f_p^3 h^3}} \tag{2}$$

Knowledge of the attenuation constant allows for designing the minimum size of a truncated slab which does not produce significant edge-diffraction effects.

The pattern bandwidth BW of the antenna has been evaluated in a simple approximate closed form, valid in the limit of small attenuation constant of the operating leaky mode, as

$$BW \cong \frac{c^3}{4\pi f_p^3 h^3} \tag{3}$$

The broadside directivity of the antenna has been evaluated, under the same approximations, as

$$D = \frac{1}{\hat{\alpha}\sqrt{-2\hat{\alpha}^2 + \sqrt{4\hat{\alpha}^4 + 1}}} \sim \frac{1}{\hat{\alpha}} \tag{4}$$

Numerical simulations have been performed on a grounded wire-medium slab, which is one possible realization of a plasma-like metamaterial medium, by means of a full-wave moment-method approach. The comparison between results obtained with the homogeneous model and those obtained with the actual metamaterial confirm the leaky-mode explanation of the high-directivity radiation at broadside.

Excitation with a point source has also been considered. In this case the excited field is not purely TE, thus the intrinsic anisotropic nature of the wire medium has to be taken into account, together with its spatial dispersion. The radiation patterns radiated in the principal planes by an electric dipole parallel to the wires' axis have been shown to be approximately equal for optimized structures, thus showing the possibility to obtain narrow pencil beams with almost omnidirectional shape.

2.2.3.1.2   Epsilon-negative NRD guides

A second research topic has been the use of metamaterials in NRD guides. In this case conditions have been sought to suppress the propagation of the undesired, highly-lossy LSE_{01} mode, which is even, i.e., has an open-circuit bisection at the symmetry plane of the structure at $x = 0$ (see Fig. 2(a)), thus obtaining unimodal propagation of the operating LSM_{01} mode, which is odd, i.e., has a short-circuit bisection at the same plane.

(a)   (b)
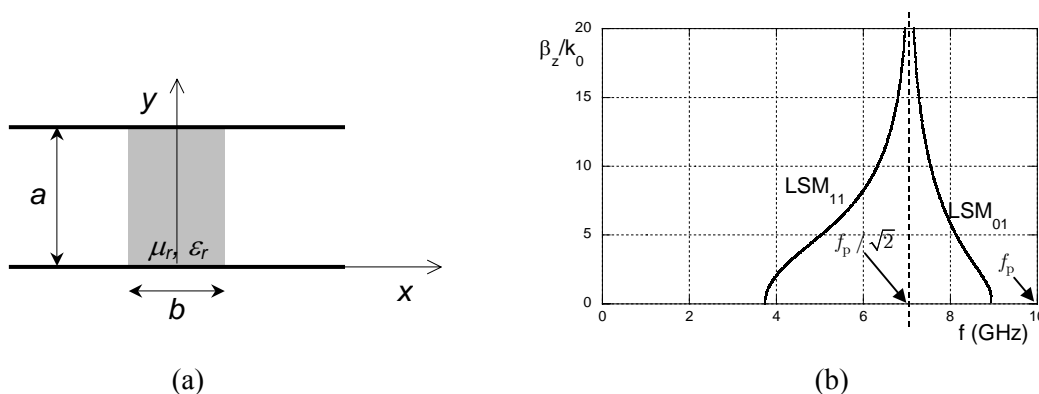
Fig. 2 – (a) Cross section of a NRD guide. (b) Dispersion diagram for LSM modes supported by an NRD waveguide with a plasma-like non-magnetic ENG medium. *Parameters*: $a = 11.4 \text{ mm}$, $b = 1.2 \text{ mm}$, $f_p = 10 \text{ GHz}$.

The idea has been to use an ENG slab, which does not support TE waves, so that the resulting NRD guide does not support any LSE mode. However, the negative value of the permittivity alters the ordinary sequence of modal cutoffs, letting the LSM_{11} even mode propagate together with the LSM_{01} mode. An analysis of the dispersion equation for even modes has revealed that a necessary and sufficient condition to suppress them is that $|\varepsilon_r| < 1$; for a plasma-like medium with relative permittivity as in Eq. (1), this occurs in the range $f_p / \sqrt{2} < f < f_p$. In this range, a sufficiently small slab width allows to achieve the desired unimodal condition for the operating mode (see an example in Fig. 2(b)).

2.2.3.2   Surface metamaterials

2.2.3.2.1   Researcher exchange with the University of Birmingham

As agreed in the WP 2.1-2 meeting held in Nice in November 2004, a researcher exchange has been performed between the University of Birmingham and "La Sapienza" University of Rome. The student Xiaojing Wang, who is a doctoral student of Prof. Peter Hall of BU, has spent one month, between June and July 2005, working at the Department of Electronic Engineering of "La Sapienza". The exchange was part of a joint project entitled *Metamaterials for millimeter-wave antennas*.

The topic chosen for starting the research was the design of EBG planar surfaces aimed at realizing multiband operation of a patch antenna embedded in a dielectric multilayer. The considered structure is shown in Fig. 3.
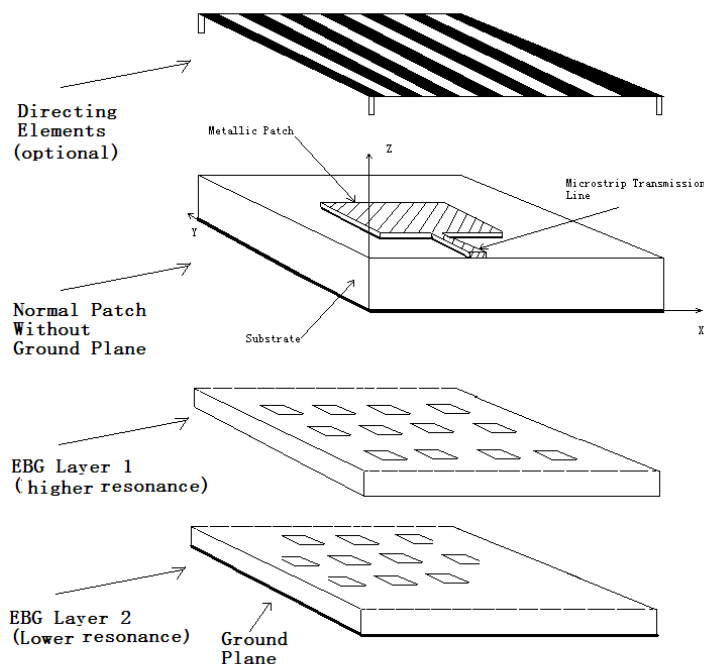
Fig. 3 – Microstrip-fed patch embedded in a dielectric multilayer comprised of periodic metal screens above and below the patch layer.

The periodic (EBG) metal screens made of square patches and placed below the patch layer are intended to behave as perfect electric conductors at different frequencies. In particular, the highest EBG has a resonant frequency f_1, and should be transparent at the lower frequency f_2 at which the lowest one resonates; both EBG should be transparent at a third and lowest frequency f_3. This would allow to synthesize different cavities below the metal patch, and thus to produce a multiband radiation. A microstrip feeding as the one shown in Fig. 3 has been considered initially, however, in order to have a better pattern symmetry, a probe feeding has been adopted for the simulations.

Full-wave simulations of finite-size antennas have been performed in HFSS to gain some confidence on the behaviour of the structure and to examine the sensitivity of the resonance frequencies to the structural parameters (e.g., the EBG spatial periods, the thicknesses of the dielectric layers, and so on) (see Fig. 4). Furthermore, simulations of the EBG screens illuminated by incident plane waves have been proposed in order to examine the phase of the reflection coefficient and thus characterize the kind of achievable boundary conditions.

The presence of an additional periodic structure placed above the radiating patch has been discussed with "La Sapienza" staff, in order to enhance the directivity of broadside radiation at a fixed frequency by exciting weakly-attenuated leaky waves. In view of the dispersive nature of such waves, this seemed to be in contrast with the desired multiband operation of the antenna, thus its use has been discarded, at least initially.

(a)
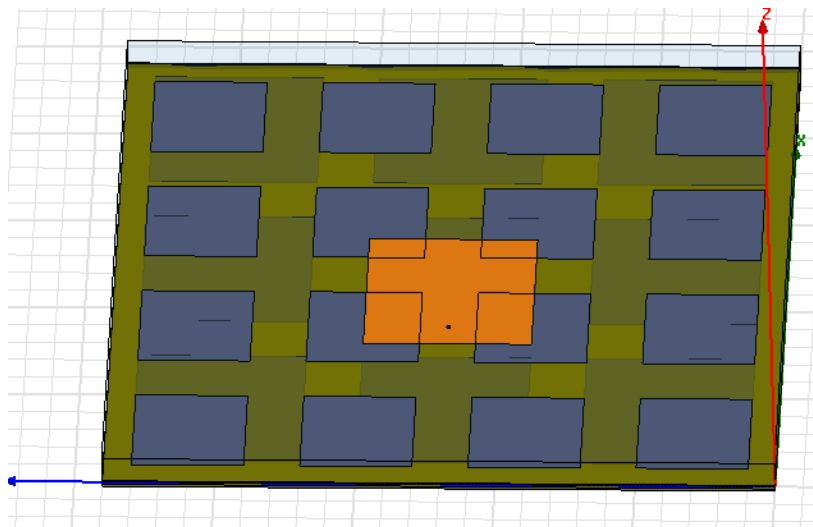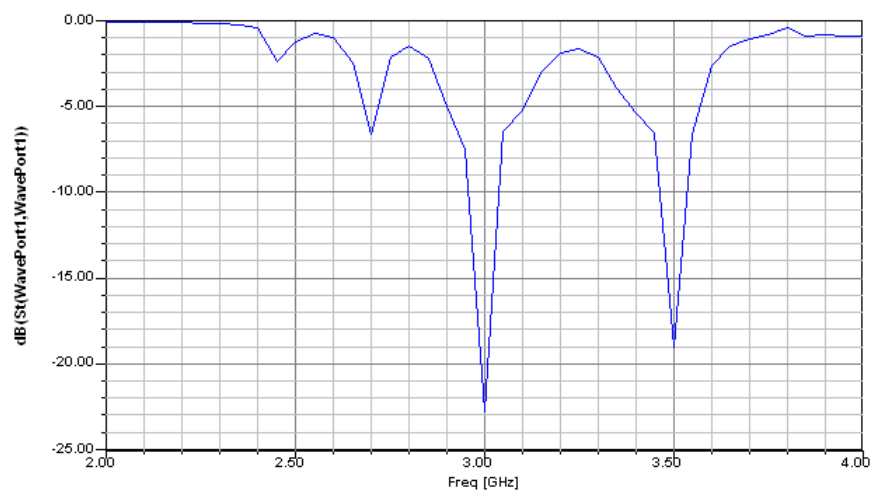
(b)

Fig. 4 – (a) Probe-fed microstrip patch antenna embedded in a two-layer EBG structure; (b) return-loss performance.

2.2.3.2.2   *Full-wave modal analysis of periodic metal screens*

On the basis of a consolidated experience in the full-wave analysis of one-dimensional periodic structures, gained during the last years by "La Sapienza" staff (in particular, by P. Baccarelli and S. Paulotto), a moment-method code based on the mixed-potential formulation of the relevant EFIE with accelerated periodic Green's function has been adapted to treat the case of printed 2D periodic structures. This research is also part of the software integration activity carried out in the framework of WP 1.1-3 in collaboration with prof. G. Vandenbosch and Dr. Volski of the Catholic University of Leuven.

Completely arbitrary geometries in the unit cell can be considered with the developed code, with reference to metal screens placed on top of a grounded dielectric slab (see Fig. 4).
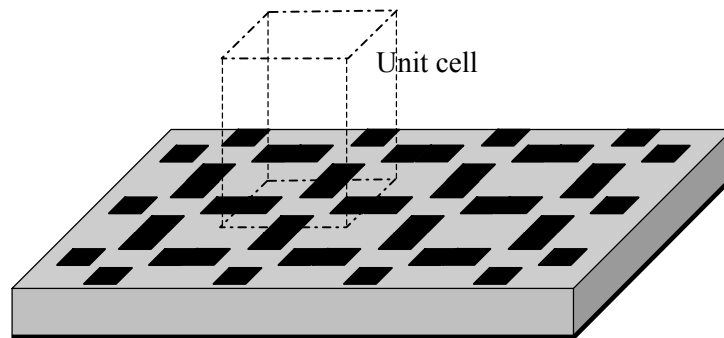
Fig. 4 – Printed 2D-periodic metal screen with arbitrary geometry inside the unit cell, placed above a grounded dielectric slab.

Simulations of dispersion properties of both surface and leaky modes propagating at arbitrary angles along such structures have been performed, validating the code with the (few) existing results of this kind published in the open literature.

2.2.4 Conclusion and future work

The analysis of planar antennas comprised of either volume or surface metamaterials of different kinds has allowed to gain a valuable physical insight into the relevant mechanisms of radiation.

A comprehensive study of homogeneous and time-dispersive low-permittivity grounded slabs has been performed, which is being extended to more complex anisotropic and space-dispersive homogeneous models, and to more demanding simulations of actual periodic structures (e.g., wire-medium slabs). A study of unimodal radiation in NRD guides made of ENG slabs has been started. Also in this case deeper analyses will regard the features of leaky modes supported by such structures and the refinement of the adopted metamaterial constitutive models.

As concerns surface metamaterials, the study of printed periodic screens has been started, both with commercial FEM-based simulators and by developing original full-wave moment-method codes. The possibility to synthesize different boundary conditions is being studied, together with a rigorous analysis of the dispersion features of surface and leaky waves propagating along periodically-loaded grounded dielectric slabs.

2.2.5 Appendix

We report here the paper "Dual-band Resonances of a Patch Antenna on UC-EBG substrate" published in the Asia Pacific Microwave Conference (APMC 2005) Proceedings (December 2005) as an outcome of the Researcher Exchange described in Sec. 2.2.3.2.1.

The information contained in this document should be used only for the scope of the contract for which this document is prepared.

2.3   Measurements of Low Profile Array Antenna at 150 GHz

Juha Ala-Laurinaho   December 20, 2005

Helsinki University of Technology

Radio Laboratory

Antenna Centre of Excellence – ACE

Activity 2.1 MM and Sub MM Wave Antennas, Integrated Antennas

WP2.1-1 and WP2.1-2

2.3.1   Introduction

One of the proposed researcher exchange projects in the work-packages WP2.1-1 and WP2.1-2 is the development of a low profile antenna array operating at 150 GHz. In this report, antenna measurement techniques in the view of the tests of a low profile array antenna at 150 GHz are described. Especially, the antenna measurement capabilities at the Radio Laboratory of Helsinki University of Technology are the basis for this report. The scope is in the basic antenna tests, namely in the antenna radiation pattern measurements.

Basically, there are three different methods for measuring the radiation pattern of an antenna: far-field method, near-field method, and compact antenna test range (CATR). In the following sections these measurement methods are briefly described and their feasibility for the measurement of the low profile array antenna at 150 GHz is discussed. The antenna under test (AUT) is not defined exactly, but is assumed here, that the largest antenna dimension does not exceed 100 mm. As the wavelength in the free space is about 2 mm, the gain of the AUT is relatively high. If the aperture efficiency is one the gain of the AUT is

$$G = \frac{4\pi A}{\lambda^2} = 31416 = 45 \text{ dB} \tag{1}$$

For a square aperture and even illumination, the half power beamwidth of 100 mm x 100 mm antenna is about

$$\theta_{3dB} = 0.89\frac{\lambda}{D} = 0.0089 \text{ rad} = 0.5° \tag{2}$$

2.3.2 Far-field measurements

In far-field measurements the separation between the antenna under test (AUT) and the test antenna is large enough so that the phase front in the aperture of the AUT can be assumed as planar, see Figure 1. The AUT is rotated to achieve the radiation pattern. E.g. elevation over azimuth type antenna rotator can be used for full 3D pattern coverage. Often, only one azimuth rotator is used and E- and H-planes of the antenna radiation pattern are measured by rotating the antenna 90 degrees around the boresight axis.
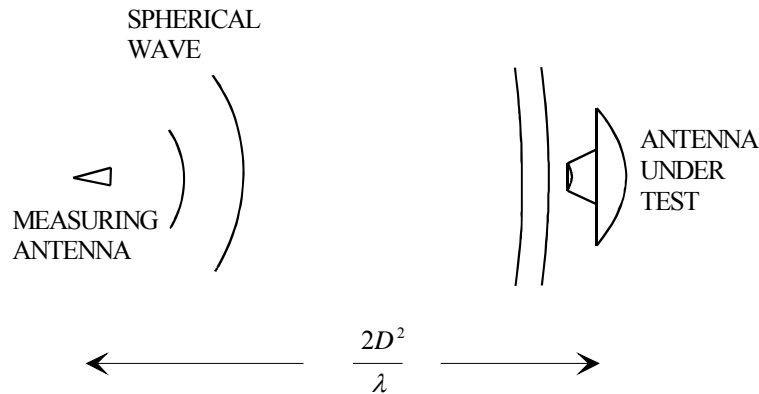
Figure 1. Far-field measurement and far-field criterion.

The common criterion for the far-field distance is that the phase deviation is less than $\lambda/16$ or 22.5°. This leads to the far-field distance of $2D^2/\lambda$. For example for antenna array with the largest dimension of 100 mm, the far-field distance at the frequency of 150 GHz is

$$R = \frac{2 \cdot 100\text{mm} \cdot 100\text{mm}}{2.0\text{mm}} = 10 \text{ m} \qquad (3)$$

Relatively large anechoic chamber is required, if indoor measurements are desirable. Significantly larger separation is required if low side lobe levels are of interest [1]. The amplitude and the phase taper due to insufficient separation affects the accuracy of the antenna measurement. The too small distance causes widening of the measured main beam, filling of the nulls, and raising of the sidelobe levels [2,3].

The atmospheric attenuation at 150 GHz is about 2 dB/km, (T = 293 K, P = 1013 mbar, Relative humidity = 43 % (7 g/m^3)) [4]. At short ranges, the dynamic range is not affected and uncertainties caused by variations of the atmospheric attenuation are not very significant at this frequency.

2.3.3. Near-field measurements

In near-field measurements the radiating near-field of the antenna is sampled and the radiation pattern in the far-field is calculated from the measured complex (amplitude and phase) field samples. The radiation pattern of the probe antenna is taken into account, when the near-field to far-field transformation is made [5]. The sampling geometry can be planar, cylindrical, or spherical. Near-field range measurements can be done indoors in a relatively small space. The temperature and humidity can be controlled and thus the distortions due to the atmosphere become are small.

In the planar geometry, the probe antenna is typically moved instead of the antenna under test. The probe movement forms a plane. Typically, the probe antenna is moved with two linear scanners. There are also other sampling geometries, e.g. plane polar and bi-polar, which require different equipment for moving the probe antenna [5,6]. In the cylindrical scanning the AUT is rotated in one plane and the probe is moved with a linear scanner. In the spherical scanning the AUT is rotated with respect to two axes. Rotation axes have to coincide, which may be difficult to achieve.

The planar geometry is the most attractive geometry for the measurement of the planar array. However, the measurement plane is always truncated, which has to be taken into account in the measurement of the radiation pattern in large angles. The valid angle or the maximum angle, where the far-field pattern is accurate, is (see Figure 2)

The information contained in this document should be used only for the scope of the contract for which this document is prepared.

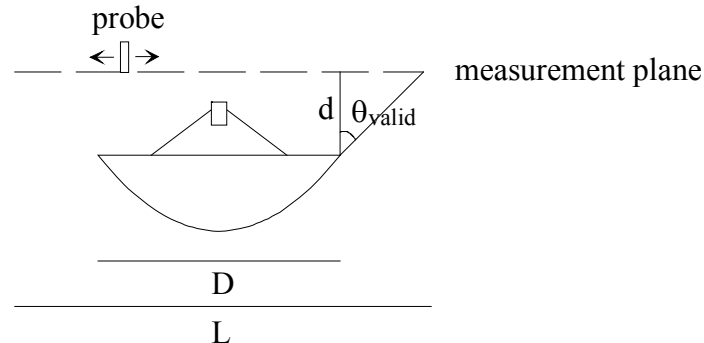$$\theta_{valid} = \arctan\left(\frac{L - D}{2d}\right)$$

(4)

Figure 2. Valid angle in planar near-field scanning.

For the planar array, the measurement distance can be relatively short (at minimum a few wavelengths). Thus, radiation pattern at quite large angles can be achieved without increasing the size of the measurement plane excessively.

The planar near-field scanning is advantageous with respect to antenna diagnostics. For example, problems in the phase or amplitude control of the antenna elements or malfunction of an antenna element can be seen directly from the measured near-field data.

The sampling of the near-field has to be dense enough satisfying the Nyquist sampling criterion. In the planar near-field scanning, the sampling interval has to be smaller than one half of the wavelength [5]. If the far-field radiation pattern of only small angular range in the main beam region is required, sparser sampling is adequate.

If the measurement area is 150 mm x 150 mm and the sampling interval is one half of the wavelength, 22 500 samples are required. If the sampling rate is ten samples per second the full data capturing takes about 40 minutes.

The main problems of the planar near-field scanning at high frequencies are the phase errors due to the bending cables and the planarity errors of the planar scanner. However, at 150 GHz with antenna dimensions of about 100 mm these are not seen very severe problems. The probe may cause interference for the AUT operation and multiple reflections may occur.

2.3.4. Compact antenna test ranges

In the compact antenna test range, a planar wave front is produced with a collimating element which can be a reflector, lens, or a hologram. The reflector based CATR is mostly used, but a hologram based CATR is also proven to be a feasible at millimeter wavelengths. CATRs enable the antenna measurements indoors in plane wave conditions, i.e., the radiation pattern can be directly measured by rotating the AUT. The main beam region can be measured without rotating the AUT by scanning the CATR feed transversally.

Reflector Based CATR

Figure 3 shows a CATR based on an off-set reflector. The feed horn radiates a spherical wavefront, which reflects from the parabolic reflector forming a plane wave. The diameter of the quiet-zone is typically limited to one third of the reflector diameter due to the edge diffraction caused by the reflector edges. The illumination in the edges of the reflector has to be low enough to prevent the disturbance of the diffracted fields. The edge diffraction can be diminished by treatment of the reflector edges, e.g. the edge can be rolled or serrated, or the edges can be covered with resistive film. With two or more reflectors the quiet-zone size can be substantially increased. Also, the cross-polarisation of the range can be reduced compared to the one reflector range [7]. The diameter of the quiet-zone can be about 70 % of the main reflector diameter [7].
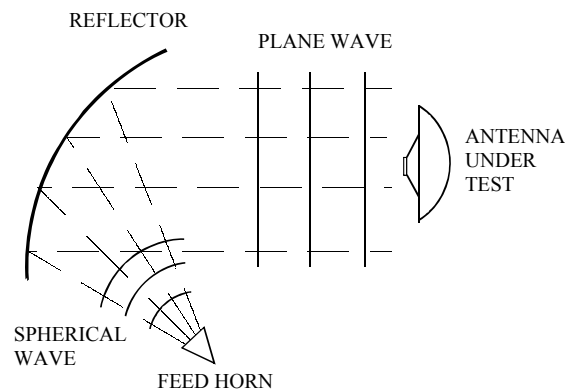

Figure 3. Compact antenna test range based on an offset reflector.

The major problem in the reflector type CATRs at high frequencies is the surface accuracy requirement. Usually the RMS surface error should be less than 0.01λ [2,8], e.g., 20 μm at 150 GHz. This surface error corresponds to a phase error of 7.2 degrees. Manufacturing of the reflectors for the measurement of 100 mm-sized antenna with good accuracy is feasible, but the costs are substantial.

Hologram Based CATRs

Figure 4 shows a compact antenna test range based on a radio frequency hologram. The planar hologram structure modulates the spherical wave radiated by a feed horn in such a way that a plane wave is formed. Hologram pattern is etched on metal layer on top of thin dielectric film.

The hologram is a transmission type of collimating element, thus the surface accuracy requirement of the hologram is considerably less stringent than that of a reflector [9]. The hologram is tensioned into a frame, which ensures sufficient planarity for the hologram. According to the simulations, the accuracy requirement for the hologram pattern is about $0.01-0.02\lambda$, which is of the same order as the surface accuracy for the reflector. However, the manufacturing of the two-dimensional hologram is easier than the manufacturing of the three-dimensional reflector surface, thus the manufacturing costs are reduced substantially. Manufacturing can be done by conventional printed circuit board technologies, i.e., exposure through mask or by laser and wet etching.
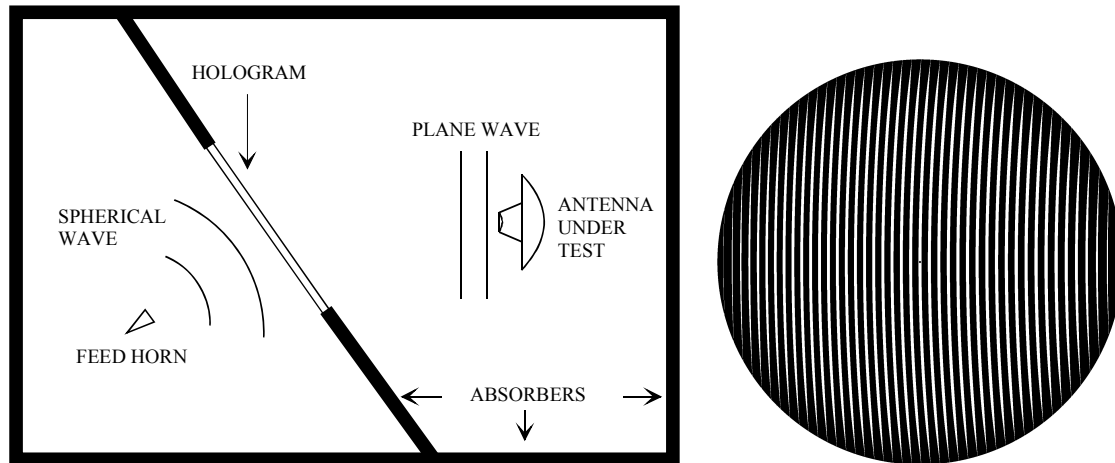
Figure 4. Hologram based CATR and an example of an amplitude hologram.

2.3.5. Antenna measurements at Radio Laboratory of Helsinki University of Technology

At the Radio Laboratory of Helsinki University of Technology, far-field measurements, planar near-field measurements, and hologram compact antenna test range measurements are carried out. The far-field distance in an anechoic chamber of the Radio Laboratory is limited to 5 metres, which limits the AUT maximum dimension to about few centimeters at 150 GHz.

The Radio Laboratory has a large planar near-field scanner with scanning dimensions of about 1.4 m x 1.2 m. The planarity of the scanner has been measured with a 3D tracking laser interferometer, and the peak-to-peak variation in the whole scanning area is about 0.3 mm. However, in smaller regions the planarity is much better. Furthermore, the measured deviations from the plane are tabulated and they can be taken into account and phase corrections can be applied to the near-field data accordingly.

The Radio Laboratory has also an accurate 3D scanner with scanning ranges of 300 mm x 300 mm x 100 mm. This scanner has very good accuracy compared to the large scanner. This scanner could be used for near-field scanning of planar array with maximum dimension of 100 mm.

The Radio Laboratory develops compact antenna test range based on a hologram and has significant experience on the high gain antenna measurements at millimeter and submillimeter wave frequencies [10–13]. For testing the radiation pattern of a 100 mm-sized antenna array, about 300 mm diameter hologram is required. It provides a quiet-zone size larger than 150 mm. The manufacturing of a 300 mm hologram is very rapid and economical. Use of hologram CATR allows antenna measurements as in a far-field range.

The Radio Laboratory uses AB Millimetre MVNA 8-350 Vector Network Analyzer for antenna measurements at millimeter wavelengths. MVNA enables complex field measurements, thus, it allows also near-field scanning measurements. In the far-field technique and in the compact antenna test ranges the phase information is not required for radiation pattern measurements. However, the phase information can be used for determination of the phase centre of the antenna.

2.3.6. Conclusions

The far-field measurements, near-field measurements and compact antenna test ranges are briefly described and their feasibility for radiation pattern measurement of a planar low profile antenna at 150 GHz was discussed. All the methods are in principle possible. The far-field distance may become inconveniently large if the antenna dimensions are of the order of 100 mm. The planar near-field scanning is attractive as it allows antenna diagnostics directly from the near-field data. One problem can be the probe antenna, which may cause interference to the operation of the array. Also, multiple reflections may occur. Thus, small probe antenna should be used. The hologram CATR is feasible and economic way to realize an antenna test range. The hologram CATR allows antenna measurements as in the far-field technique.

2.3.7. References

[1]   R. C. Hansen: Measurement distance effects on low sidelobe patterns, *IEEE Transactions on Antennas and Propagation*, Vol. 32, No. 6, 1984, pp. 591–594.

[2]   *IEEE Standard Test Procedure for Antennas*, IEEE Std 149-1979, published by IEEE, Inc., 1979, 143 p., distributed by Wiley-Interscience.

[3]   G. E. Evans, *Antenna Measurement Techniques*, Artech House, Boston, 1990, 229 p.

[4]   P. R. Foster, D. Martin, C. Parini, A. Räisänen, J. Ala-Laurinaho, T. Hirvonen, A. Lehto, T. Sehm, J. Tuovinen, F. Jensen, K. Pontoppidan: Mmwave antenna testing techniques - Phase 2, *MAAS Report 304*, Issue No 2, ESTEC Contract No 11641/95/NL/PB(SC), December 1996, 224 p.

[5]   A. D. Yaghjian: An overview of near-field antenna measurements, *IEEE Transactions on Antennas and Propagation*, Vol. 34, No. 1, 1986, pp. 30–45.

[6]   Y. Rahmat-Samii, L. I. Williams, R. G. Yaccarino: The UCLA bi-polar planar-near-field antenna-measurement an diagnostics range, *IEEE Antennas and Propagation Magazine*, Vol. 37, No. 6, 1995, pp. 16–34.

[7]   A. D. Olver: Compact antenna test ranges, *Proceedings of the Seventh International conference on Antennas and Propagation (ICAP)*, York, UK, 1991, pp. 99–108.

[8]   J. Tuovinen: Methods for testing reflector antennas at THz Frequencies, *IEEE Antennas and Propagation Magazine*, Vol. 35, No. 6, 1993, pp. 7–13.

[9]   T. Hirvonen, J. Ala-Laurinaho, A. V. Räisänen: Performance analysis of a submillimeter wave hologram CATR, *Proceedings of the 27th European Microwave Conference*, Jerusalem, Israel, September 8–12, 1997, pp. 681–686.

[10]   J. Häkli, T. Koskinen, A. Lönnqvist, J. Säily, J. Mallat, J. Ala-Laurinaho, V. Viikari, A. V. Räisänen, J. Tuovinen: Testing of a 1.5 m reflector antenna at 322 GHz in a CATR based on a hologram, *IEEE Transactions on Antennas and Propagation,* Vol. 53, Issue 10, October 2005, pp. 3142–3150.

[11]　A. Lönnqvist, T. Koskinen, J. Häkli, J. Säily, J. Ala-Laurinaho, J. Mallat, V. Viikari, J. Tuovinen, A. V. Räisänen: Hologram-based compact range for submillimeter wave antenna testing, *IEEE Transactions on Antennas and Propagation,* Vol. 53, Issue 10, October 2005, pp. 3151–3159.

[12]　T. Koskinen, J. Ala-Laurinaho, J. Säily, A. Lönnqvist, J. Häkli, J. Mallat, J. Tuovinen, A.V. Räisänen: Experimental study on a hologram based compact antenna test range at 650 GHz, *IEEE Transactions on Microwave Theory and Techniques*, Vol. 53, No. 9, September 2005, pp. 2999-3006.

[13]　J. Ala-Laurinaho, T. Hirvonen, P. Piironen, A. Lehto, J. Tuovinen, A. V. Räisänen, U. Frisk, Measurement of the Odin telescope at 119 GHz with a hologram type CATR, *IEEE Transactions on Antennas and Propagation,* Vol. 49, No. 9, 2001, pp. 1264–1270.